



<https://theses.gla.ac.uk/>

Theses Digitisation:

<https://www.gla.ac.uk/myglasgow/research/enlighten/theses/digitisation/>

This is a digitised version of the original print thesis.

Copyright and moral rights for this work are retained by the author

A copy can be downloaded for personal non-commercial research or study, without prior permission or charge

This work cannot be reproduced or quoted extensively from without first obtaining permission in writing from the author

The content must not be changed in any way or sold commercially in any format or medium without the formal permission of the author

When referring to this work, full bibliographic details including the author, title, awarding institution and date of the thesis must be given

Enlighten: Theses

<https://theses.gla.ac.uk/>
research-enlighten@glasgow.ac.uk

Characterisation of selected magnetic elements

Mhairi Crawford, M.Sci.

Department of Physics and Astronomy,
University of Glasgow

Presented as a thesis for the degree of Ph.D.
in the University of Glasgow, University Avenue,
Glasgow G12 8QQ.

July 2004

ProQuest Number: 10753959

All rights reserved

INFORMATION TO ALL USERS

The quality of this reproduction is dependent upon the quality of the copy submitted.

In the unlikely event that the author did not send a complete manuscript and there are missing pages, these will be noted. Also, if material had to be removed, a note will indicate the deletion.



ProQuest 10753959

Published by ProQuest LLC (2018). Copyright of the Dissertation is held by the Author.

All rights reserved.

This work is protected against unauthorized copying under Title 17, United States Code
Microform Edition © ProQuest LLC.

ProQuest LLC.
789 East Eisenhower Parkway
P.O. Box 1346
Ann Arbor, MI 48106 – 1346

GLASGOW
UNIVERSITY
LIBRARY:

Ecce Eduardus Ursus scalis nunc

tump-tump-tump

occipite gradus pulsante post Christophorum Robinum descendens. Est quod sciat unus et solus modus gradibus descendendi, nonnunquam autem sentit, etiam alterum modum exstare, dummodo pulsationibus desinere et de eo modo meditari possit. Deinde censet alios modos non esse.

A.A. Milne,
translated by A. Lenard



Text from Winnie ille Pu Latin translation (c) Alexander Lenard 1960
Original English text by A A Milne, copyright under the Berne Convention.
Used with permission of Egmont Books Limited, London.

Line illustration by E.H. Shepard copyright under the Berne Convention,
reproduced by permission of Curtis Brown Ltd., London.

Acknowledgements

There are many people I wish to thank for their help and support over the course of my PhD. It is not possible to mention everyone but to those who have helped in any way, I am very appreciative of your help.

Some people however, deserve a special mention. Firstly, I wish to thank John Chapman and Andrew Long, my supervisors, for their help, patience, support and guidance. Steven McVitie for many useful discussions regarding my research and help on the CM20 when things weren't going according to plan. Sam McFazdean for keeping the equipment running and being about to help fix everything as and when required. Also within the Solid State group: Brian Miller for his help with sample preparation; Colin and Billy for looking after the evaporators; Lucy for helping organising trips and printing draft copies; my office companions, past and present (Jamie, Mo, Ewan, Dave E, Pedro and Craig), for putting up with me and offering help, advice, support and ever so occasionally a welcome distraction from work; Jamie Scott for being absolutely wonderful at knowing everything to do with any machine in the group, and thanks for proof-reading some of the thesis through as well; the occupants of room 309 (Christine, Clair, Damien, James and Tom) also deserve a mention for their help and support and willingness to provide a distraction from work when required, especially around coffee time; Agne for being at the same place at the same time and Pat for providing IT support. Many of the people mentioned have also become friends over the last 3 and a bit years and I would also like to thank them for their friendship through the ups and downs of the PhD.

Other people who have offered invaluable technical support are the beam writer clean room technicians, my samples would never have reached completion without their help. Chris Marrows from Leeds has also been great, helping with the sputtering of specimens and the GMR measurements obtained in

Leeds.

On a more personal level, my friends have been a tower of support throughout the whole process, cheering me up when I'm down or stressed and reminding me on a regular basis that I need to stop work every so often and go out to relax. Most notably: Jacqui Allan, Jo Burnside, Clair Collins, Cathy James, Islay Johnston, Sandra Martin, Sarah Miller, Catherine Norrie, Seonaid Taylor and Katherine Wilson. Also, Dave Pritchard for his conversations about quantum gerbils and other serious research matters alongside friendship and the knowledgeable support of someone who's already been through it all.

Most importantly, I wish to thank my family for being there for me, their support, help and tolerance. I wouldn't have managed it without your help and I promise I'll never do anything like this again. Mum, you deserve a very special mention for all your effort proof reading various chapters and trying to understand the principles behind the research ... just think ... you can forget all about GMR now. I'd also like to thank you for putting up with possibly the worst tempered grouch in Glasgow - you've no idea how much I appreciate it. Thanks also to Dad for not asking how it's going too often and providing an objective viewpoint, Neil for letting me know what they're really thinking, Gran for feeding me on a regular basis and Auntie Anne and John for providing Gerbil sitting services when I was away at conferences and the like.

Contents

Summary	v
Declaration	x
1 Introduction, Magnetics and Transport Theory	1
1.1 Introduction	1
1.2 Basic Ferromagnetism	1
1.3 Energy Considerations	2
1.3.1 Exchange Energy	3
1.3.2 Magnetocrystalline Energy	4
1.3.3 Magnetostatic and Zeeman Energies	5
1.3.4 Domains and Domain Wall Energy	6
1.3.5 Total Energy	8
1.4 Reversal Processes	10
1.4.1 Hysteresis	10
1.4.2 Rotation and Coherent Reversal	10
1.4.3 Domain Nucleation and Irreversible Processes	12
1.5 Magneto Transport	13
1.5.1 Magnetic Multilayer Material	13
1.5.2 Magneto-transport in semiconductor heterostructures . .	19
2 Fabrication Techniques	24

2.1	Introduction	24
2.2	Lithography	25
	2.2.1 E-beam lithography	25
	2.2.2 Photolithography	32
2.3	Etching	33
	2.3.1 Wet etch	34
	2.3.2 Dry etch	35
2.4	Metallisation	35
	2.4.1 Evaporation	36
	2.4.2 Sputtering	38
2.5	Lift-off	39
2.6	Wafer cleaning	40
2.7	Example	41
3	Transmission Electron Microscopy of Artificial	
	Antiferromagnetic Thin Film Spin Valves	42
3.1	Introduction	42
3.2	Transmission Electron Microscopy	45
	3.2.1 The Electron Gun	45
	3.2.2 The column	46
3.3	Observation of Domains by TEM	53
	3.3.1 Beam and sample interaction	53
	3.3.2 Lorentz microscopy	56
3.4	Spin Valve Structure	59
3.5	Physical Microstructure	60
3.6	Magnetic Reversal	65
	3.6.1 Introduction	65
	3.6.2 As Grown State	65
	3.6.3 Magnetising Experiments	67

3.7	Magnetoresistance Measurements	81
3.8	Discussion and Conclusions	82
3.8.1	Cross Section Study	84
3.8.2	Conclusions	90
4	Transmission Electron Microscopy of Patterned Spin Valves	92
4.1	Introduction	92
4.2	Specimen Fabrication	94
4.3	Magnetic Studies of Specimen 5	95
4.3.1	DPC images of the as grown state	96
4.3.2	Reversal of $4 \times 2 \mu\text{m}^2$ rectangular element parallel to growth field	101
4.3.3	Reversal of $4 \times 2 \mu\text{m}^2$ rectangular element at 45° to growth field	103
4.3.4	Reversal of $4 \times 2 \mu\text{m}^2$ rectangular element perpendicular to growth field	109
4.3.5	Reversal of $4 \times 2 \mu\text{m}^2$ elliptical element parallel to growth field	112
4.3.6	Reversal of $4 \times 2 \mu\text{m}^2$ elliptical element at 45° to growth field	113
4.3.7	Reversal of $4 \times 2 \mu\text{m}^2$ elliptical element perpendicular to growth field	115
4.3.8	Discussion	115
4.4	Magnetic Studies of Specimen 1	118
4.4.1	DPC images of the as grown state	119
4.4.2	Reversal of $4 \times 2 \mu\text{m}^2$ elements	124
4.4.3	Discussion	130
4.5	Simulations	130
4.5.1	Simulations on a Balanced AAF structure	131

4.5.2	Simulations on an Unbalanced AAF structure	137
4.6	Conclusion	140
5	Transport in Hybrid Magnetic/Semiconductor Devices	143
5.1	Introduction	143
5.1.1	Hall effect in inhomogeneous magnetic fields	145
5.2	Cryostat Design/Operation	147
5.3	Fabrication of samples	150
5.3.1	Wafer Fabrication	150
5.3.2	Hall Bar Fabrication	151
5.4	Experiments	160
5.4.1	Large Hall Bar	160
5.4.2	1500 × 500 × 50 nm Co element with one end over a Hall cross	172
5.4.3	1500 × 500 × 50 nm Co element in the centre of the Hall bar	184
5.4.4	1000 × 500 × 50 nm Co element in the centre of the Hall bar	186
5.4.5	1500 × 500 × 20 nm Py element with one end over a Hall cross	193
5.5	Conclusions	196
6	Conclusions and Future Work	198
6.1	Introduction	198
6.2	Conclusions	199
6.2.1	Artificial antiferromagnetically biased spin valves	199
6.2.2	Hybrid ferromagnet/semiconductor heterostructures	201
6.3	Future Work	202
6.3.1	Artificial antiferromagnetically biased spin valves	202
6.3.2	Hybrid ferromagnet/semiconductor heterostructures	203

A Appendix A	205
A.1 Introduction	205
A.2 Fabrication process	205
A.2.1 Wafer Cleaning	205
A.2.2 Alignment Marks	206
A.2.3 Ohmics	208
A.2.4 Isolation	210
A.2.5 Small Gates	212
A.2.6 Thick gate leads	215
A.2.7 Magnetic structures	216
References	i

Summary

The work presented in this thesis is a study of the reversal properties of selected magnetic materials. The reversal mechanisms of magnetic multilayer artificial anti-ferromagnetically biased spin valves (AAF SV), both in the form of continuous thin films and discrete elements have been investigated. SVs consist of two ferromagnetic layers separated by a non magnetic spacer layer. The magnetisation of one layer is pinned through exchange coupling to an adjacent anti-ferromagnetic layer. The magnetisation of the other ferromagnetic layer (the free layer) can be reversed by applying a small external field. If the free layer aligned is parallel to the pinned layer, a low resistance state is measured. For an anti-parallel alignment, the resistance is considerably larger. This is a phenomenon known as Giant Magnetoresistance (GMR) and is highly desirable for applications such as read heads in disc drives. For AAF biased systems, the pinned layer consists of two ferromagnetic layers and a non magnetic spacer such that the two ferromagnetic layers couple anti-ferromagnetically. This modifies the coupling within the entire multilayer stack giving a potential advantage for applications.

A second area of investigation comprised hybrid ferromagnetic / semiconductor systems. Magnetic elements were formed on Hall bars enabling a non-invasive study of the interactions between the stray field from the elements and electrons in the two dimensional electron gas (2DEG) of the semiconductor. From this, the magnetisation state of the elements can be investigated giving further insight into the reversal properties of the material.

The first Chapter introduces the basic concepts of ferromagnetism and reviews the energy contributions which govern the behaviour of magnetic materials. Following this is a discussion of domains, domain walls and some of the reversal mechanisms relevant to the work presented in later Chapters.

Two types of magneto-resistive effects important to the two experimental techniques of this thesis are introduced: giant magnetoresistance with an emphasis on spin valve systems and quantum transport mechanisms for semiconductor heterostructures.

Techniques necessary for the fabrication of all specimens investigated are discussed in Chapter 2. A discussion of electron beam lithography and photolithography, pattern design, transfer and resists with reference to the systems available precedes a description of some of the associated techniques.

An investigation of the free layer magnetic reversal processes for a range of AAF biased spin valves is presented in Chapter 3. Prior to this is a discussion of the instrumentation and techniques employed. An overview of the transmission electron microscope (TEM) including the gun, column and limitations on the resolution is given. The principal mode of operation, Lorentz microscopy, is then discussed with emphasis on Fresnel and differential phase contrast (DPC) modes which were used to investigate the free layer reversal of the spin valves in situ. Reversal mechanisms of the spin valves are then presented for a range of specimens. The general structures of all specimen are nominally identical with only the second Co layer of the AAF varying between specimens. Marked differences in the reversal processes are apparent as the thickness of the second Co layer is increased from a fraction of the thickness to near double the thickness of the first Co layer. Some insight into the mechanisms causing the change in the reversal processes is given.

Chapter 4 continues the investigation of AAF biased spin valves with the study of a range of spin valve elements. The elements have one of two layer structures, a range of orientations with respect to the growth and applied field directions, and a range of dimensions down to $400 \times 200 \text{ nm}^2$. DPC images of the free layer reversal for selected elements are presented. It was found that a range of reversal mechanisms was possible and was dependent on element shape and orientation. Domain processes were observed in all reversals. The reversals

presented exhibited wide hysteresis loops without sharp jumps between $\pm M_s$,

Accompanying the experimental results, simulations of the AAF SV system using a commercially available package are shown for some of the smaller elements. These indicate that the elements possess two stable magnetisation states with a rapid switch between each state. The fields at which reversal of these smaller elements occurred were considerably greater than for larger elements, as was the offset in the hysteresis loop. Experimentally, the fields at which reversal occurred for the smallest elements were recorded and were compared with the simulations.

The final experimental chapter discusses the fabrication and measurement of hybrid ferromagnet/semiconductor samples. This system enables a non-invasive characterisation of the reversal of a magnetic element by studying the interaction between the stray field from the element and electrons in the 2DEG. The study revealed that small Hall bars can be defined on a much larger Hall bar, enabling bulk characterisation alongside smaller scale investigations. Both the large and small Hall bars exhibit similar magnetotransport properties at high fields with the smaller Hall bar showing additional mesoscopic effects at lower fields.

With magnetic elements present, it has been shown that the magnetisation state of elements of dimensions $\sim 1 \mu\text{m}$ can be detected using the Hall bar. For such an element placed symmetrically between two Hall contacts, both the longitudinal and transverse resistance measurements shows structure attributed to the magnetic element. A simple model is used to successfully describe the relationship between them.

Calculations of the magnitude of the Hall signal from experimental and simulated systems are presented indicating a discrepancy between the two values in many samples. This is tentatively ascribed to partial lift-off of the element giving a curled structure, but this model is yet to be confirmed. However, for an element placed symmetrically between the two Hall contacts, both the

shape of the hysteresis loop and the magnitudes of the resistance structures were in good agreement with theoretical estimates.

General conclusions and a discussion of further work are presented in Chapter 6

Declaration

This thesis is a record of experimental work which I carried out by myself during the period 2000-2004 in the Department of Physics and Astronomy at the University of Glasgow. The work described herein is my own, with the exception of the AAF biased SV deposition which was carried out by Dr Marrows at the University of Leeds.

Chapter 1

Introduction, Magnetism and Transport Theory

1.1 Introduction

This chapter describes the basic concept of ferromagnetism, the various energy considerations which help determine the magnetic state, properties and characteristics of a ferromagnetic material. Reversal processes appropriate to the materials studied are discussed. Further to this, two types of magnetotransport are introduced: giant magnetoresistance with an emphasis on spin-valves which display this phenomenon, and quantum transport theory relating to semiconductor/ferromagnetic metal hybrid structures. Jiles [1], Craik [2] and Hubert [3] have been frequently referred to in sections 1.2 and 1.3.

1.2 Basic Ferromagnetism

A ferromagnet is a material which possesses non-zero magnetisation in the absence of an applied field. In ferromagnetic materials, there is a dipole moment associated with each atom. The non-zero magnetic moment arises due to these dipole moments aligning parallel to their nearest neighbours. Above

a critical temperature, the Curie temperature (T_C) of the material, this alignment breaks down due to thermal agitation and the dipoles become randomly oriented. The material then behaves as a paramagnet.

In the case of an elemental ferromagnet, the dipole moment arises primarily from the spin angular momentum of unpaired electrons in the 3d or 4f shells of the atoms. At sufficiently low temperature in ferromagnets, the moments behave in a cooperative manner. Weiss (1906) proposed that an internal molecular field can be used to account for the spontaneous alignment of the dipole moments. This internal field, \mathbf{H}_m , is proportional to the magnetisation \mathbf{M} of the sample. Heisenberg (1928) suggested this molecular field had its origin in a quantum mechanical effect, the exchange interaction between each molecule and its nearest neighbours. Specifically he suggested the interaction could be written in the form

$$E_H = -2J_{ij}\mathbf{S}_i \cdot \mathbf{S}_j \quad (1.1)$$

where J_{ij} is the exchange parameter, \mathbf{S}_i is the spin angular momentum of a molecule i , coupled with nearest neighbours of spin \mathbf{S}_j . For J_{ij} positive, this results in an energy minimum when the dipoles have a parallel alignment and is the interaction responsible for a spontaneous moment arising in zero applied field.

From this, it can be deduced that for a ferromagnetically aligned state, J_{ij} must be greater than zero and for antiferromagnetic alignment, J_{ij} must be less than zero.

1.3 Energy Considerations

The magnetic state of a ferromagnetic sample can be understood by taking into consideration various energies associated with the material properties and physical dimensions of the sample coupled with the knowledge that the material will, in general, relax into an energy minimum. Described below are

the exchange energy, the magnetocrystalline energy, the magnetostatic energy and, the Zeeman energy, all of which combine to give the total energy E_{tot} of the sample.

1.3.1 Exchange Energy

As described earlier, the exchange interaction, equation 1.1, is responsible for the spontaneous alignment of dipole moments within the material. For isotropic exchange, a simplified expression for the exchange energy can be used. In this case, $J_{ij} = J$ and for identical atoms $S_i = S$ with small ϕ_{ij} , where ϕ_{ij} is the relative angle between the spins, a small angle approximation can be applied. The simplified atomic expression is then

$$E_H = -2J_{ij}S_iS_j \cos \phi_{ij} \simeq JS^2\phi_{ij}^2 \quad (1.2)$$

where the constant term has been dropped.

A more general expression for the simple cubic lattice unit cell, is

$$E_H = nJS^2a^2 [(\nabla\alpha)^2 + (\nabla\beta)^2 + (\nabla\gamma)^2], \quad (1.3)$$

where α, β, γ are the directional cosines of the magnetisation vector, a is the lattice parameter, S the magnitude of the spin component of the magnetic moment and n a multiplication factor dependent on the crystal structure.

There are $\frac{1}{a^3}$ atoms per unit volume for a cubic lattice, thus equation 1.3 can be rewritten to give a more complete description for a finite volume of magnetic material:

$$E_{ex} = A \int_V [(\nabla\alpha)^2 + (\nabla\beta)^2 + (\nabla\gamma)^2] dV. \quad (1.4)$$

A is the exchange constant and for a cubic system,

$$A = \frac{nJS^2}{a}. \quad (1.5)$$

For bcc materials, $n = 2$ and for fcc $n = 4$. The spontaneous alignment gives a magnetisation vector $\mathbf{M} = M_S \mathbf{m}_i(\alpha(r), \beta(r), \gamma(r))$. M_S is the saturation magnetisation and \mathbf{m}_i is a unit vector in the direction of \mathbf{M} .

1.3.2 Magnetocrystalline Energy

The magnetocrystalline or anisotropy energy arises from the tendency of the internal magnetic moment, \mathbf{M} , to lie along a preferred axis. A preferred axis is known as an easy axis. For a hexagonal or uniaxial system, the anisotropy energy can be written as

$$E_K = K_1 \sin^2 \theta + K_2 \sin^4 \theta. \quad (1.6)$$

Or, using direction cosines

$$E_K = K_1(1 - \gamma^2) + K_2(1 - \gamma^2)^2. \quad (1.7)$$

For a cubic system using the expression involving direction cosines

$$E_K = K_1(\alpha^2\beta^2 + \beta^2\gamma^2 + \alpha^2\gamma^2) + K_2\alpha^2\beta^2\gamma^2. \quad (1.8)$$

For all three expressions, K_1 and K_2 are the anisotropy constants of the material and θ is the angle between the magnetisation vector \mathbf{M} of the material and the easy axis. α, β, γ are the directional cosines of the magnetisation vector \mathbf{M} and relate the magnetisation vector to the cubic axes. For uniform magnetisation, the magnitude of the magnetisation vector, $|\mathbf{M}| = M_S$, the saturation magnetisation. The anisotropy energy can also be calculated per unit volume by integrating over the volume of magnetic material.

For transition metals with uniaxial or hexagonal anisotropy, K_1 is significantly greater than K_2 and expression 1.6 is frequently reduced to

$$E_K \simeq K \sin^2 \theta. \quad (1.9)$$

There is an energy minimum when $\theta = 0^\circ$, when \mathbf{M} is parallel to the easy axis. As the orientation of \mathbf{M} rotates away from the easy axis, the anisotropy energy will increase until it reaches a maximum at $\theta = 90^\circ$. This is known as the hard plane. For cubic systems, higher order terms are required.

The relations described above are applicable to single crystals. For polycrystalline material, the anisotropy direction will vary locally between crystallites. These variations lead to a very small anisotropy value and no easy overall axis but local easy axes. An appreciable anisotropy and hence an easy axis can be induced by growing the ferromagnetic material in an externally applied field, by annealing the material after deposition with an external field present, or by depositing the ferromagnetic material at an oblique angle. After the introduction of an easy axis, small variations in the anisotropy due to the crystallites still remain. These local fluctuations in the direction of the magnetisation vector result in magnetisation ripple. This is further discussed in Chapter 3.

1.3.3 Magnetostatic and Zeeman Energies

The magnetostatic energy arises due to the presence of surface and volume charges, Fig 1.1. These charges give rise to an external stray field and hence an internal field. This results in an energy

$$E_m = -\frac{1}{2}\mu_0 \int_V \mathbf{H}_d \cdot \mathbf{M} dV \quad (1.10)$$

where \mathbf{H}_d is the internal demagnetising field, \mathbf{M} is the magnetisation and the energy is calculated over the magnet volume. An expression for \mathbf{H}_d is

$$\mathbf{H}_d = \frac{1}{4\pi} \int_V \frac{-\nabla \cdot \mathbf{M}}{r^2} dV + \frac{1}{4\pi} \int_S \frac{\mathbf{M} \cdot \mathbf{n}}{r^2} dS. \quad (1.11)$$

where \mathbf{M} is the internal magnetisation and \mathbf{n} a unit vector normal to the surface.

If an external field is applied, an additional term is required to account for the interaction between the magnetisation and the applied field,

$$E_z = -\mu_0 \int_V \mathbf{M} \cdot \mathbf{H}_{app} dV. \quad (1.12)$$

This is known as the Zeeman energy.

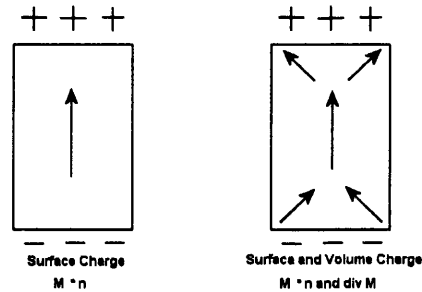


Figure 1.1: Diagrams showing simple domain states exhibiting magneto-static energy arising from surface and surface and volume charges

1.3.4 Domains and Domain Wall Energy

A ferromagnetic system will relax over time into a state which minimises the overall energy E_{tot} . This energy minimum can be less than the energy required to keep all the moments aligned in a parallel state, i.e. less than the energy required to achieve the single domain saturation magnetisation condition. In 1930, Becker [4] proposed that this phenomenon was due to the existence of magnetic domains which was confirmed by Bitter [5] in 1931. These domains are regions within the magnetic material where all moments have parallel alignment, i.e. the magnetisation is saturated. However, two adjacent domains would not have the same direction of magnetisation. These different directions of magnetisation lower the overall net magnetisation of the material, Fig 1.2. The boundary between two regions of differing magnetisation is known as a domain wall. Within the domain wall, the magnetisation vector rotates smoothly between the two directions of magnetisation.

Various types of domain wall exist. These depend on how the magnetisation vector rotates. A Bloch wall, Fig 1.3a, is where the magnetisation rotates out of the sample plane. A Néel wall, Fig 1.3b, is where the magnetisation rotates within the sample plane. A third type, the cross-tie wall, Fig 1.3c, is a combination of both Bloch and Néel walls. The type of wall found in a

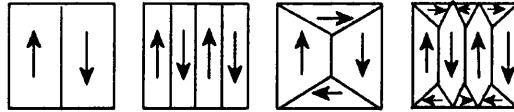


Figure 1.2: Domains lowering the overall net magnetisation

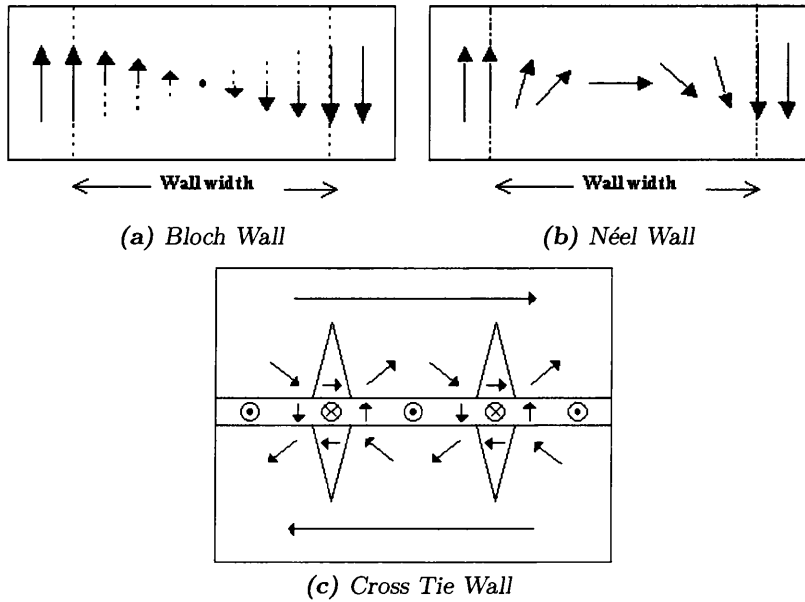


Figure 1.3: Domain wall types

particular sample depends on the sample thickness, as shown in Fig 1.4.

The formation of domains and domain walls reduces the magnetostatic energy of a system but increases the exchange and anisotropy energies. This change in exchange and anisotropy energies can be described by a domain wall energy. Taking into account these energy considerations and the magnetostatic energy gives an optimal domain wall thickness dependent on the specimen type. In a thin film, it would be expected that considerably more energy would be required to pull the magnetisation vector out of plane than with a thicker film. Hence, Néel walls are more common in thin films and Bloch walls in

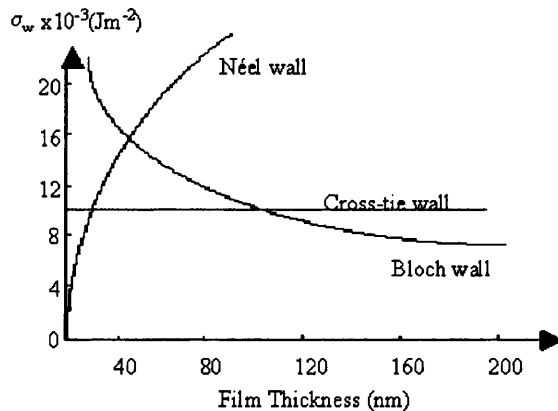


Figure 1.4: Dependence of wall type on sample thickness. Material used is permalloy. σ_w represents the energy density [6], section 3.6.4

thicker films. For the film shown in Fig 1.4, it can be observed that for film thicknesses of less than 10 nm, Néel walls are preferred. Between 10 nm and 70 nm, cross tie walls are dominant and above a film thickness of 70 nm, Bloch walls require the least energy, as may be expected. For a Bloch wall in a bulk material, assuming that the exchange and anisotropy energies do not vary through the wall, the domain wall energy per unit area for a 180° wall [2], section 1.12.2,

$$E_w = 4\sqrt{AK}. \quad (1.13)$$

where A is the exchange constant and K is the anisotropy constant. The energy per unit area of a Néel wall cannot be written in such a compact form.

1.3.5 Total Energy

The total energy of a magnetic system is given by summing all the energies discussed above.

$$E_{tot} = E_{ex} + E_K + E_m + E_z \quad (1.14)$$

To calculate a possible magnetic state of a system, the total energy must be minimised as a magnetic specimen will, over time, relax into an energy min-

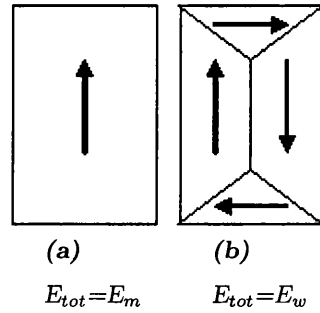


Figure 1.5: Two examples indicating how a different domain structure can arise from differing energy contributions

imum. This requires the balancing of the constituent energies which comprise the total energy to achieve a minimum. At times, it is simpler to consider a domain wall energy, (as the wall energy is a combination of the exchange and anisotropy energies), than to calculate each of the energies separately. For example, in Fig 1.5a, a single domain structure, E_{TOT} consists primarily of a magnetostatic energy which is relatively simple to calculate. The second example Fig 1.5b, however, contains a flux closed structure. In this case, E_{TOT} is principally the sum of the anisotropy and exchange energies with a reduction in the magnetostatic energy. It is therefore simpler to consider the wall energy rather than the individual anisotropy and exchange energies.

The magnetic state a system will relax into also depends on the size. For example, the energy of the single domain sample shown in Fig 1.5a decreases as r^3 as the size decreases. The energy of the flux closed sample, however, decreases with r . Therefore, for small enough magnetic samples, a single domain state would be more energetically favourable whereas for a larger magnetic sample, flux closure or another domain configuration may be preferred.

Many local energy minima exist as well as the absolute energy minimum of a magnetic specimen. The minimum reached depends on the history of the material and any fields applied. For example, the application and removal of an external field could result in the magnetic state of a specimen relaxing to

an energy other than the absolute energy minimum, i.e. the input of energy may change the magnetic state and enable the material to relax into a lower energy state.

1.4 Reversal Processes

1.4.1 Hysteresis

For magnetic material in the as grown state that has never been exposed to an applied field, the material is likely to consist of domains arranged such that the net magnetisation is zero. Applying an external field to the sample leads to a net magnetisation being induced within the sample along the direction of applied field. This increases until a maximum moment is reached, the saturation magnetisation M_S , when all moments are aligned with the applied field, H_{app} . Decreasing the applied field leads to a reduction in the net sample magnetisation. At zero field, the sample magnetisation may not have reduced to zero. Any remaining net moment is known as the remanent magnetisation, M_R . A field applied in the opposite direction will reduce the remanent magnetisation to zero. The applied field strength at which this occurs is known as the coercive field H_c . Further increase of the applied field in the negative direction will cause the sample to reach saturation magnetisation in the opposite direction. The loop traced as the applied field is swept from positive to negative values then back to positive is known as the hysteresis loop, Fig 1.6.

1.4.2 Rotation and Coherent Reversal

In an ideal situation, the magnetisation direction of a sample would reverse by a reproducible, reversible process. One example is by pure, coherent rotation of the magnetisation direction. A description of the process is outlined below.

For a uniaxial particle aligned such that the applied field is perpendicular

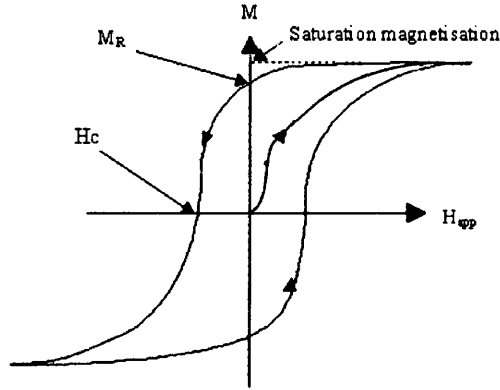


Figure 1.6: A typical hysteresis loop

to the easy axis and with magnetisation direction at an angle θ to the easy axis. If all moments of this particle are aligned so that the magnitude of the particle magnetisation is the saturation magnetisation M_S , Fig 1.7, the system equilibrium energy density

$$K \sin^2 \theta - \mu_0 H M_S \sin \theta \quad (1.15)$$

is at its minimum when the derivative of the expression is 0, i.e. $\frac{dE}{d\theta} = 0$. This gives:

$$2K \sin \theta \cos \theta - \mu_0 H M_S \cos \theta = 0 \text{ so that } \sin \theta = \frac{\mu_0 H M_S}{2K}. \quad (1.16)$$

Therefore the magnetisation induced in the applied field direction, H_{app} , as specified in Fig 1.7 is

$$M = M_S \sin \theta = \frac{\mu_0 H M_S^2}{2K} \text{ and } \chi = \frac{M}{H} = \frac{\mu_0 M_S^2}{2K} \quad (1.17)$$

where K is the anisotropy constant, H the applied field, μ_0 the permittivity in free space and χ the magnetic susceptibility.

From this it can be observed that the magnetisation increases linearly with H until a maximum value H_K .

$$H_K = \frac{2K}{\mu_0 M_S} \quad (1.18)$$

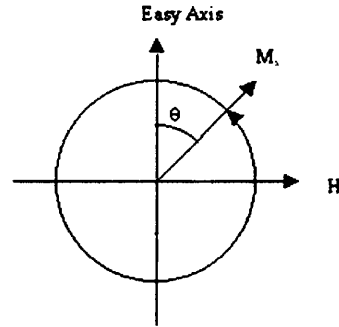


Figure 1.7: Directions of magnetisation, \mathbf{M} , and applied field, \mathbf{H}_{app} , with respect to the easy axis for rotation

If the applied field is parallel to the easy axis, the magnetisation direction jumps discontinuously from antiparallel to parallel to the applied field at $H = H_C = H_K$.

1.4.3 Domain Nucleation and Irreversible Processes

For a single domain system with the magnetisation direction parallel to the easy axis and an external field applied in an anti-parallel direction, it may be more energetically favourable for reversal to occur through domain processes rather than coherent rotation. Domains frequently nucleate from edges and corners.

Systems which already support domains before the application of an external field will undergo similar processes possibly without nucleation of further domains. An example is shown in Fig 1.8a. Those domains that are favourably aligned with the applied field will increase in size, Fig 1.8b. Those close to the applied field direction will rotate to align with the field. Domains which are not favourably aligned will either reduce in size until eliminated or jump irreversibly to align with the field direction, Fig 1.8c. If the applied field is large enough, the magnetisation will align with the applied field direction completely, Fig 1.8d.

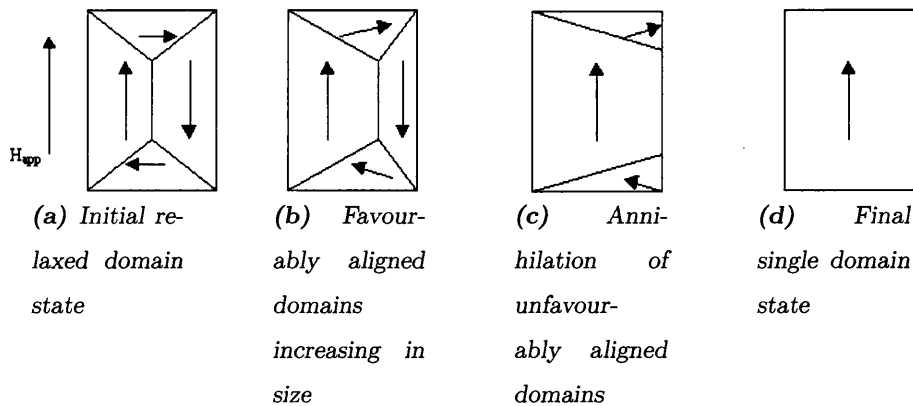


Figure 1.8: Domain processes

Domain growth/reduction and rotation are mostly reversible processes however the annihilation of a domain or magnetisation jumps are irreversible.

1.5 Magneto Transport

Of the many different phenomena which have been studied, only the two types of magneto-transport relevant to this thesis will be discussed. The first is magnetoresistance of magnetic multilayers which is important for one class of materials investigated in this thesis. The second is transport in semiconductor heterostructures. In this case, the material is introduced first leading into a discussion of the more relevant quantum and semi-classical transport properties. The transport properties are used to investigate the magnetic material.

1.5.1 Magnetic Multilayer Material

Magnetoresistance

Magnetoresistance is a phenomenon that describes the change in electrical resistance of a magnetic material either due to the material's magnetic structure or an applied external field.

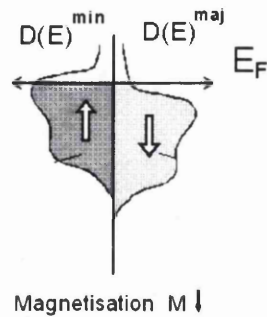


Figure 1.9: Density of states for majority and minority electrons.

Many types of magnetoresistance (MR) exist, some of the more common are Anisotropic (AMR), Colossal (CMR), Giant (GMR) and Tunnelling (TMR) magnetoresistance. Here we only consider GMR arising from spin valve multi-layer stacks.

Giant Magnetoresistance, GMR, was first observed by Baibich [7] in Fe/Cr multilayer structures grown by Molecular Beam Epitaxy (MBE). The resistivity of the system was found to decrease by a factor of 2 at 4 K under an applied field of 20 kOe. Parkin [8] later found that a larger GMR ratio existed in sputtered systems. A GMR of greater than 100 % has been demonstrated [9, 10]. The origin of GMR was described by Baibich et al as spin dependent scattering of conduction electrons at the interfaces.

In ferromagnetic transition metals, conduction electrons tend to arise from the s,p or d shells or a mix of the three. The electrons can be divided into two families which can be distinguished according to the projection of the electron spin along the local magnetisation direction. These electron families are known as spin up or spin down electrons, conventionally parallel and antiparallel to the local magnetisation direction. The two families can have very different scattering rates. This spin dependent scattering arises from the difference of empty states at the Fermi level into which electrons can be scattered, Fig 1.9.

The differences in scattering rates gives a difference in the mean free paths. For example, in $Ni_{80}Fe_{20}$ spin up electrons have a mean free path of around 5 times that of spin down electrons [?].

For a multilayer system with layers having parallel magnetisation alignment, Fig 1.10, electrons with a spin parallel to that of the local magnetisation direction will be weakly scattered from boundaries and weakly scattered within the magnetic material due to the density of states at the Fermi level. However, electrons with a spin antiparallel to the local magnetic induction, Fig 1.10, will be weakly scattered at boundaries but will also be strongly scattered within the magnetic layers. This is due to the different density of states for the spin down electrons at the Fermi level giving many more free states for electrons antiparallel to the local magnetisation direction to scatter into.

For an antiparallel alignment of magnetic layers, both spins will be scattered at boundaries, and alternately strongly and weakly scattered from the two magnetic layers depending on whether the spin is anti-parallel or parallel to the local magnetisation direction.

A convenient analogue to this is to consider the different spin states having a different electrical resistance. In the parallel alignment, the spin up electrons are only weakly scattered and as such, carry a large part of the current giving a low resistance state. In the antiparallel alignment, both spin up and spin down electrons are alternately weakly and strongly scattered giving a higher resistance state for both electron species. This is also shown in Fig 1.10.

From this two current model [11], it can be seen that for a parallel magnetisation alignment (low resistivity state),

$$\rho_P = \frac{\rho_{\uparrow}\rho_{\downarrow}}{\rho_{\uparrow} + \rho_{\downarrow}} \quad (1.19)$$

where ρ_{\uparrow} is the resistivity of the spin \uparrow electrons and ρ_{\downarrow} is the resistivity of spin \downarrow electrons. Also, for an antiparallel magnetic alignment (high resistivity

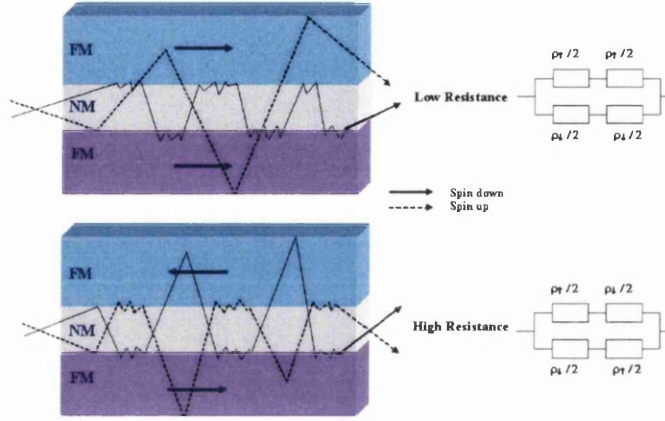


Figure 1.10: Scattering within a multilayer stack.

state),

$$\rho_{AP} = \frac{\rho_{\uparrow} + \rho_{\downarrow}}{4}. \quad (1.20)$$

This gives a GMR ratio of

$$\frac{\Delta\rho}{\rho_P} = \frac{(\rho_{\uparrow} - \rho_{\downarrow})^2}{4\rho_{\uparrow}\rho_{\downarrow}} = \frac{1 - \alpha^2}{4\alpha} \quad \text{where } \alpha = \frac{\rho_{\downarrow}}{\rho_{\uparrow}} \quad (1.21)$$

As the thickness of the spacer layer is varied, the GMR amplitude will vary. The coupling between adjacent layers can also change leading to either ferromagnetic or anti-ferromagnetic coupling in zero applied field. The coupling can oscillate from parallel to antiparallel with the separation of the two magnetic layers. This is known as Ruderman-Kittel-Kasuya-Yosida (RKKY) coupling; details are given in [12, 13, 14].

There are two interesting geometries for studying GMR in multilayer materials. One is when the sense current is in the plane of the material (CIP), the second where the current is perpendicular to the plane of the material (CPP). CPP tends to lead to a larger change in resistance as the current passes through the interfaces. However the overall resistance is very low. Standard practice is to use a four probe CIP set-up to measure GMR.

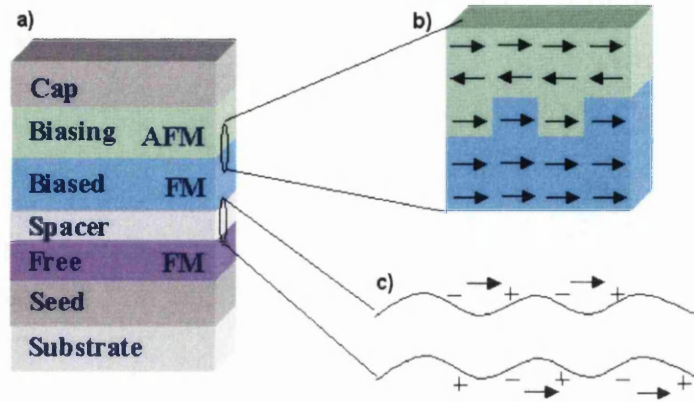


Figure 1.11: A typical spin valve layer structure. AFM is an antiferromagnetic layer and FM a ferromagnetic layer.

Spin Valves

Many GMR applications require a system which exhibits MR at small applied fields. One such multilayer system is the spin valve, Fig 1.11a.

This layer structure is known as a top spin valve and contains two ferromagnetic layers known as the free and the biased or pinned layers. These are coupled by a non-magnetic spacer layer. The pinned layer has its direction of magnetisation fixed through exchange coupling to a pinning layer grown adjacent to it. The magnetisation direction of the pinned layer is only reversed by reasonably large fields. The spacer layer thickness is chosen so that the pinned and free layers are weakly coupled with a parallel alignment in zero field. Due to the weak coupling, the free layer can be reversed by a low field, for example <10 Oe, so that the free and pinned layers then have an anti-parallel alignment. This leads to a change in resistance [15]. The different coupling mechanisms and magnetoresistance are briefly described below.

Exchange Coupling

Within the anti-ferromagnetic layer, the number of moments pointing in one direction is equal to the number of moments pointing in the other direction. At the interface between the anti-ferromagnetic layer and the ferromagnetic layer, there may be an unequal number of moments pointing in each direction due to grain orientation, shape, size and surface roughness. The ferromagnetic layer is ordered below the Curie temperature. If this is chosen to be higher than the Néel temperature of the anti-ferromagnetic material then applying an external field to the system while keeping the temperature between the Curie and Néel temperatures will cause the ferromagnetic layer to align with the external field while the anti-ferromagnetic layer is in a paramagnetic state. As the temperature is lowered through the Néel temperature of the anti-ferromagnetic layer, localised anti-ferromagnetic moments couple parallel to the aligned ferromagnetic moments. The exchange interaction between moments then keeps the direction of the moments fixed after the applied field is removed. The anti-ferromagnetic/ferromagnetic coupling is known as exchange biased coupling, Fig 1.11b. Further information on exchange biasing can be found in [16, 17, 18, 19].

Interlayer Coupling

Two different types of interlayer coupling exist, Orange Peel (Néel) and RKKY. RKKY coupling [12, 13, 14], as introduced earlier, is the interaction responsible for the change between ferromagnetic and anti-ferromagnetic alignment of two magnetic layers due to spacer thickness. Orange peel coupling [20, 21] comes from the magnetostatic interaction arising from surface roughness in the individual layers. The surface roughness is correlated between different layers due to the interface profile propagating between layers during deposition. The magnetostatic interaction keeps the magnetic moments on each side of

the ferromagnetic/non-magnetic/ferromagnetic tri-layer aligned parallel, giving ferromagnetic coupling, Fig 1.11c.

Magnetoresistance of Spin Valves

The resistivity of the parallel and antiparallel alignment states are as described previously in equations 1.19 and 1.20. These lead to the same MR discussed earlier, equation 1.21. For the spin valve layer structures investigated, an MR of under 10 % is more common than higher GMR values.

The above properties indicate that spin valves are useful as materials for sensors. The low reversal field of the free layer leads to a high sensitivity for say, read heads in hard disk drives and the two resistive states depending on free layer orientation gives a relatively simple way of determining the “bit” magnetisation direction in a recorded track. Details of the specific spin valves investigated will be given in Chapter 3.

1.5.2 Magneto-transport in semiconductor heterostructures

Quantum Transport measurements can be used to investigate the interactions between a magnetic element and the two dimensional electron gas (2DEG) in a semiconductor heterostructure. Further details of this can be found in Chapter 5. Here, an introduction to the semiconductor substrate and transport properties is given. For this section, extensive reference to Davies [22] and Sze [23] have been made.

Semiconductor heterostructures used in most transport measurements are semiconductors composed of more than one material. Active regions of heterostructures are typically at or close to interfaces. However surface roughness at the interfaces causes electron scattering which reduces the mobility. This can be overcome by growing the heterostructures using Molecular Beam Epi-

taxy [23], section 8.6. To achieve as near perfect interfaces as possible, the crystals must have the same crystal structure and lattice constant. This condition is satisfied for a number of common III-V compounds. (III, V relates to elements in the third and fifth columns of the periodic table). The materials used are GaAs and $\text{Al}_x\text{Ga}_{1-x}\text{As}$, where x is the fraction of Al ions replacing Ga ions in the structure, as these satisfy the above conditions.

The purpose of creating these heterostructures is to modify the properties of the material to suit the users' needs. In this case, a good mobility is the desired outcome. To achieve the desired transport properties, extra electrons or holes must be introduced for increased conductance. The process employed to achieve this is doping.

Doping the region directly where the electrons (holes) are required is the most obvious option. However, charged donors (acceptors) are left behind when the electrons/holes are released. These scatter the carriers through their Coulomb interaction and reduce the mobility. To avoid this, a process called modulation doping is employed. In this technique, the carriers are introduced into the structure at a distance from the region in which they are required and migrate to the desired area. Initially, the material is neutral and the band structure is flat. See Fig 1.12a. On the release of the electrons from the doped region, some cross into the GaAs. Due to the surface barrier between GaAs and AlGaAs, a quantum well is created in which the carriers are trapped. This is due to the energy band gap (ΔE_c) on one side and the electrostatic potential on the other. The quantum well prevents electrons crossing the energy barrier back to the n-AlGaAs and separates the electrons from their donors leading to an excess of electrons in the required region, Fig 1.12b. The trapped electrons all have similar energies and are confined in the z direction due to the well. However, the electrons are free to move in the xy plane. This is called a 2 Dimensional Electron Gas or 2DEG. This method of doping has two advantages: the scattering from donors in the transport area is reduced

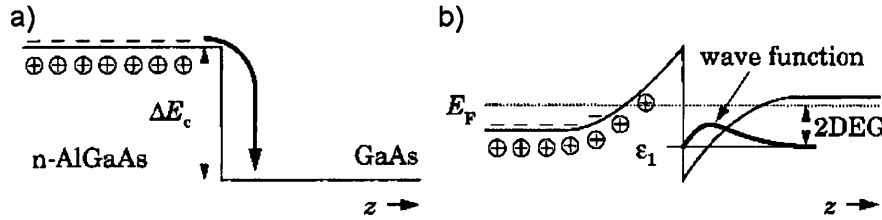


Figure 1.12: Band structure of GaAs/AlGaAs heterostructure showing 2DEG formation. [23]

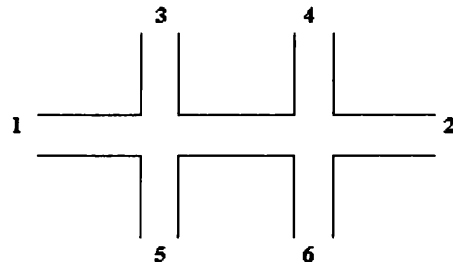


Figure 1.13: schematic of hall bar

and the electrons have been confined to two dimensions. To reduce scattering further, an undoped AlGaAs spacer layer between the n-AlGaAs and GaAs can be used.

To enable a study of the transport characteristics of the 2DEG, a pattern must be defined in the 2DEG to further confine the electrons and create regions where electrical contact can be made to supply a current through the material. One such system is the Hall bar, Fig 1.13. A current is applied along the long axis of the device and voltage measurements are taken either longitudinally or transversely, between contacts 3/4 (5/6) and 3/5 (4/6) respectively.

Under the application of a perpendicular, uniform magnetic field, electrons will have a circular orbit, the cyclotron orbit, with a cyclotron frequency and

radius:

$$\omega_c = \left| \frac{eB}{m} \right| \quad (1.22)$$

$$R_c = \frac{v}{\omega_c} = \frac{\sqrt{2mE}}{|eB|}, E = E_F \quad (1.23)$$

where ω_c is the cyclotron frequency, B the magnitude of the applied field, e and m the charge and mass of an electron respectively. R_c is the cyclotron radius and v , the magnitude of the electron velocity.

Due to the electron cyclotron motion, the continuous density of states for free electrons is replaced by a series of delta functions known as Landau levels. There are $n_B = \frac{eB}{h}$ states permitted in each Landau level. In a magnetic field, electron spins are non degenerate and therefore a factor of 2 is not required here. As B increases from zero, the separation between Landau levels changes, as does the number of available states. The experiments undertaken are with carrier concentration (charge per unit area) n_{2D} constant, therefore the number of occupied Landau levels ν , known as the filling factor, changes with B .

$$\nu = \frac{n_{2D}}{n_B} = \frac{hn_{2D}}{eB} \quad (1.24)$$

This calculation counts the two electron spins as separate levels. ν is generally not an integer, N is the number of full levels. Increasing B causes more levels to become available and leads to fewer electrons filling the highest occupied level. At $\nu = N$, the top level becomes empty. i.e. when $B = \frac{hn_{2D}}{eN}$ there are N full levels.

Plotting the density of states at the Fermi level with respect to B shows that it drops to zero at $\nu = N$ and is at its maximum at $\nu = N + \frac{1}{2}$. This can be shown experimentally by measuring R_{xx} , the longitudinal resistance. At low magnetic fields and at low temperature ($< 4\text{K}$), the resistivity is constant but as B increases, it develops strong oscillations. This is called the Shubnikov-de-Haas effect, Fig 1.14. Measuring the transverse resistance at low fields, $R_{xy} = BR_H = \frac{B}{en_{2D}}$. At high fields, plateaux in the trace can be found when

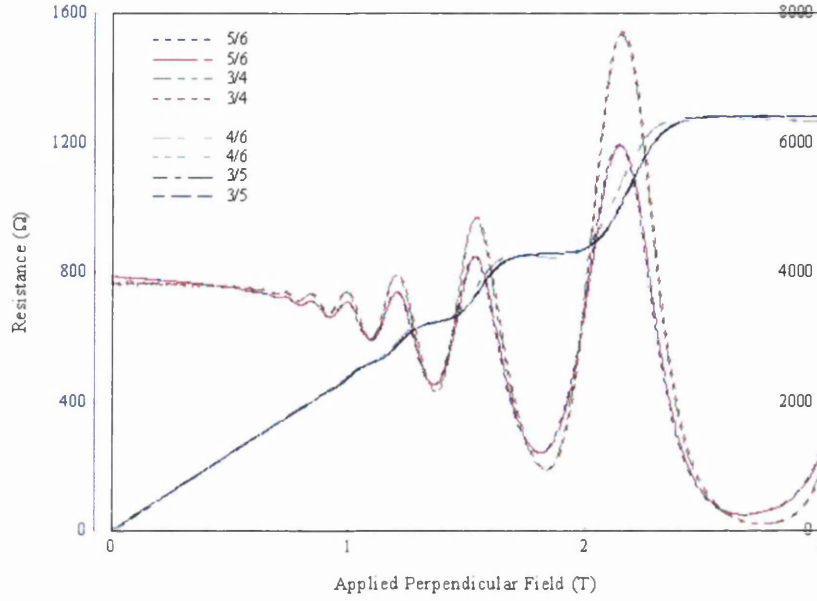


Figure 1.14: Typical Shubnikov-de-Haas and Quantum Hall traces

$R_{xy}^{-1} = \left(\frac{ne^2}{h}\right)$ with n being at an integer. The plateaux exist at integral filling factors and are known as the Quantum Hall effect, Fig 1.14. Plateaux in the the Quantum Hall effect correspond to minima in the oscillations of the Shubnikov-de-Haas effect.

Using the high field longitudinal or transverse measurements to obtain n_{2D} , the carrier concentration leads to the electron mobility μ through:

$$\mu = \frac{1}{n_{2D}eR_{xx}(B=0)} \quad (1.25)$$

The samples investigated here are GaAs/AlGaAs heterostructures. The mobility and carrier concentrations are found using the SdH and QH effects. The majority of subsequent measurements are taken at low fields where quantisation into LL is not important.

Chapter 2

Fabrication Techniques

2.1 Introduction

It was necessary to design and fabricate suitable specimens to enable the investigation of spin valve multilayers and hybrid semiconductor/ferromagnetic metal structures introduced in Chapter 1. Investigation of the spin valve samples (introduced in section 1.5.1) was carried out using transmission electron microscopy. This required the fabrication of self-supporting electron transparent windows. These windows served as a substrate onto which the spin valve stack could be deposited, and enabled the specimen to be mounted onto a suitable sample rod for the microscope.

The study of the ferromagnetic metal/semiconductor samples required Hall bars (introduced in section 1.5.2) to be designed and fabricated. These Hall bars confined the current flow in the 2DEG enabling measurements to be made of the interaction between a magnetic element deposited near the centre of the Hall bar and the 2DEG. Due to the complexity of the design, it was necessary to fabricate these samples in a series of steps, each of which is known as a fabrication layer and consists of a complete fabrication cycle. Each cycle comprises a range of techniques which are introduced below.

The techniques required for each fabrication layer are lithography, combined with etching or metallisation, and lift-off. The general principles of these techniques will be discussed in this chapter, with specifics pertinent to the individual samples being discussed in the relevant chapters.

2.2 Lithography

Lithography is the transfer of a pattern from a physical or electronic mask to a substrate. A variety of specialised techniques have been developed to enable micro and nano scale lithography, including electron beam lithography (EBL), photo or optical lithography, x-ray lithography and ion beam lithography. Electron beam lithography and photolithography were used in this project and are discussed below. Electron beam lithography was the principal tool used for pattern transfer and as such, is discussed in the greatest detail.

2.2.1 E-beam lithography

There are two standard EBL techniques. Projection EBL uses a broad electron beam and a physical mask, which is electron transparent only in the regions to be patterned, close to or in contact with the substrate. The second method does not use a physical mask. A focused, computer controlled, electron beam defines the pattern by scanning over the regions to be exposed. The mask pattern is held in the control computer. This latter technique was used for the fabrication carried out within this project.

The EBL machine is similar to a Scanning Electron Microscope (SEM) and is one of the tools available as part of the Nanoelectronics Research Centre of the Electronics and Electrical Engineering department at the University of Glasgow. The machine used in this research was a commercially available Electron Beam Pattern Generator 5 (EBPG5) beamwriter [24], a schematic diagram of which can be seen in Fig 2.1. Electrons from the LaB_6 source

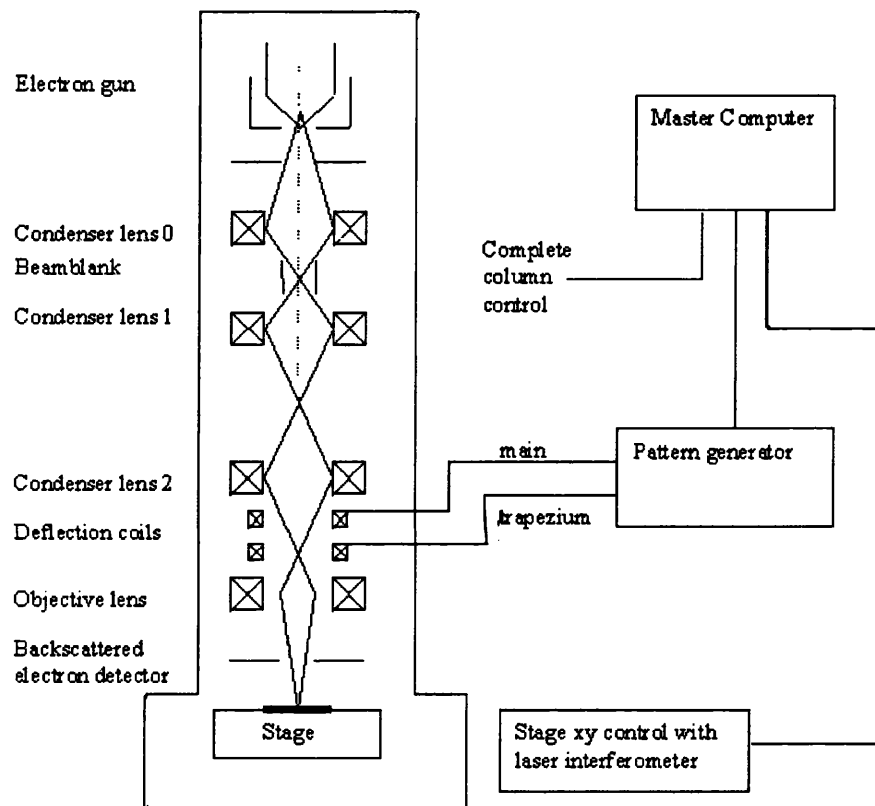


Figure 2.1: Schematic of the EBPG5

are focused onto the specimen (see section 3.2 for further details about the focusing process). A range of spot sizes is available with the smallest spot size for 50 keV electrons being 15 nm. For 100 keV electrons, the minimum spot size is reduced to 12 nm. The EBPG5 can write features of 20 nm over 126 mm² with a beam placement accuracy of 5 nm. It is kept in a class 10 cleanroom (i.e. one in which there are fewer than 10 particles of diameter greater than 0.5 μm per cubic foot) with temperature control of ± 0.25 °C for stability. Different machines have different characteristics, for example, a modified JEOL 100CXII TEM which is also available within the Nanoelectronics Research Centre has a minimum spot size of ~ 3 nm. This higher resolution enables the patterning of smaller features but is less automated and hence more complex to use. It was not required for this project as the EBPG5 has a resolution better than that required for this research.

Pattern Design

As mentioned previously, no physical mask was used and the pattern was transferred onto the substrate by a scanned electron beam under computer control. A computer-aided-design (CAD) program was used to design the pattern to be transferred to the substrate. The software used in this research was the WAM package [25] which enables all the design aspects to be viewed simultaneously. For example, the designs for different fabrication layers could be studied together to check inter-layer alignment. The design for each separate layer was stored as an individual sub-structure of the complete pattern which enabled each layer to be written separately.

The completed WAM file was transferred to a control computer which stored the mask design. A second piece of software, CATS [26] was used to specify which sub-structure was to be written. The areas of the sample to be exposed by the e-beam were thus specified and fractured. Fracturing is the process whereby the pattern is broken up into pixels, with each pixel being

Program	Output file type	Description
WAM	.GDS	Initial pattern design
↓		
readfile	-GDS.clib	Converts file format
↓		
CATS	.cft	Fractionates pattern for beamwriter
↓		
writefile	.IWFL	Creates pattern file
↓		
BELLE	.com	Creates job file

Table 2.1: The file processes involved from design to pattern transfer

exposed individually by the beam during writing of the pattern. The CATS software produced an output pattern file containing the fractured design in a format compatible with the EBL control.

To complement this pattern file, a third program, BELLE [27] was used to specify the beam diameter, step size, beam dose and the number of pattern repeats leading to the construction of a job file. The pattern and the job files provided the beamwriter with the information required to expose the desired areas at the specified dose, point by point, in a raster pattern, Fig 2.2. The file processes from design to pattern transfer are shown in Table 2.1.

As mentioned in section 2.1 and earlier in this section, some samples require more than one fabrication layer. In these multilayer systems, it was necessary to achieve accurate alignment of the current layer with respect to those previously fabricated. This process is known as registration. The job file enabled the registration process to occur by positioning the pattern to be transferred at a known distance, specified by the user, from a set of markers. These markers were laid down in the first fabrication layer enabling them to

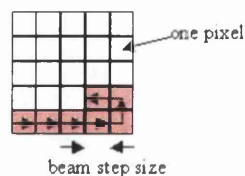


Figure 2.2: A schematic of the e-beam scan process during writing

be referred to in the fabrication of subsequent layers thus allowing accurate alignment of many layers.

Resist and Pattern Transfer

The pattern was transferred onto the substrate via an electron sensitive layer known as resist. Electron resists are polymers dissolved in a liquid solvent, usually chlorobenzene or o-xylene. The liquid was deposited onto the surface of a substrate. To achieve a uniform layer, the sample was first attached to a vacuum chuck, then spun with the resist at a known rate for a set period of time. The solution in which the resist was dissolved was evaporated through baking. The choice of resist depends on the subsequent processing requirements after patterning. For example, a single layer of resist is sufficient for etching. For metallisation, however, a bi-layer of resist is preferable. This will be discussed later in this section and also in section 2.4. All samples in this research had Polymethyl methacrylate (PMMA) resist deposited, were spun for 60 s at 5000 rpm and then baked at 180 °C for half an hour for the first layer and an hour for the second layer.

During the transfer of the pattern to the substrate, electrons interact with the resist leading to a number of events. The first is a change in the chemical bonds of the resist due to the electron - resist interaction. In the case of a positive resist, such as the PMMA used for this research, the electron - resist interaction serves to break bonds in exposed areas of the long polymer

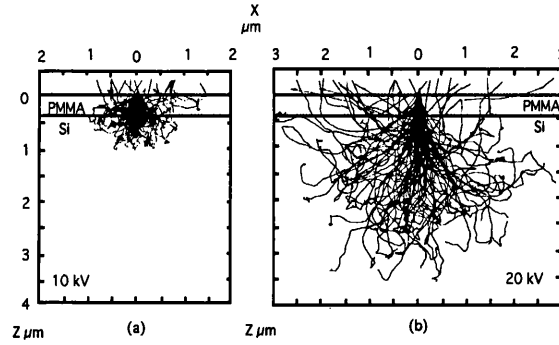


Figure 2.3: Electron beam paths for 10 and 20 kV acceleration

molecules thus increasing its solubility. For a negative resist the electron-resist interaction has the effect of solidifying the polymer in exposed areas thus reducing solubility.

As the electron beam interacts with the resist, small and large angle scattering events occur. Forward scattering involves small angle scattering events and leads to an increase in the initial beam diameter. The increase in effective beam diameter (in nm) is $d_f = 0.9 \frac{R_t}{V_b}^{1.5}$ where R_t (nm) is the resist thickness and V_b (keV) is the electron beam accelerating voltage [28].

Back scattering is the term used to describe large angle scattering events. During the electron-solid interaction, the electrons continually lose energy as they slow down and produce a cascade of low voltage secondary electrons. Simulations can be used to predict electron paths as seen in Fig 2.3. As the accelerating voltage is increased, the number of scattering events increases and a larger area of resist is exposed to a weak dose of electrons.

For non-bulk substrates such as the electron transparent windows, back scattering is greatly reduced. Forward scattering still has the effect of broadening the effective beam diameter but the beam footprint does not increase significantly. The lack of back scattering gives an altered exposure pattern in the resist which can affect further patterning of the sample.

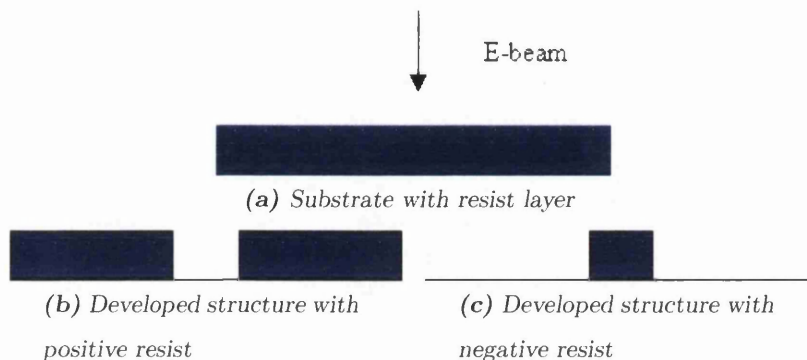


Figure 2.4: After patterning and developing of positive and negative resist

Once the mask pattern has been transferred to the substrate, the sample was developed by removing the resist that is not required. In the case of a positive resist, the patterned areas have the resist removed. In the case of negative resist all areas other than those patterned are removed, Fig 2.4.

The developing process consists of immersing the substrate in a solution of methyl isobutyl ketone to isopropanol (MIBK:IPA) and gently agitating for 60 s at 21 °C. The developing process was halted by rinsing in IPA and the substrate was then dried using a fast flow of nitrogen gas. MIBK has the function of developing the PMMA and IPA the function of diluting the solution. For large features a MIBK:IPA 1:1 is conventionally used, for smaller features 1:2.5 is more common.

As stated earlier, the choice of resist used depends on subsequent fabrication processes. Feature size must also be taken into account with smaller features requiring a thinner resist layer. For metallisation, a bi-layer of resist was used to help prevent a phenomenon known as edge-flagging (see section 2.4). The bi-layer consists of a base layer with a polymer of lower molecular weight and a top layer with a polymer of higher molecular weight. Due to backscattering, the base layer receives a greater exposure dose than the top layer. This has the effect of producing an undercut profile on completion of the development

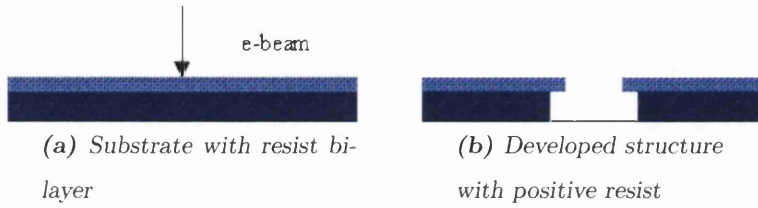


Figure 2.5: The resist profile after patterning for a bilayer

Resist concentration (%)	Resist type	Film thickness (nm)
15.0	(2010)	1200
4.0	(2010)	100
4.0	(2041)	100
2.5	(2010)	40
2.5	(2041)	40

Table 2.2: Resist thicknesses depending on concentration

process, such as that represented schematically in Fig 2.5.

The two electron resists used are both PMMA resists, Elvacite (2041) which has a molecular weight of 345 kDa and Elvacite (2010) which has a molecular weight of 90 kDa. When dissolved in solvent and spun at 5000 rpm for 60 s, these resist layers are of thickness as stated in Table 2.2.

2.2.2 Photolithography

The technique of photolithography exposes the sample by use of a physical mask and ultraviolet radiation. Photolithography enables a high throughput of samples as the process of patterning is much more rapid than that of e-beam lithography and the mask plate can be used many times.

The mask consists of a glass plate coated with chromium in areas which are not to be patterned thus blocking the transmission of the UV radiation in

specified areas. This mask plate is then placed in contact with the resist coated substrate and UV radiation is applied for a set time, usually around 8-10 s thus exposing the resist in the desired areas. The resist can then be developed as described in section 2.2.1 enabling further patterning of the substrate.

In this thesis, photolithography was used in the preparation of TEM windows. The poorer resolution ($\simeq 0.5 \mu\text{m}$), when compared with EBL, was adequate for this process as no small features were required and the pattern definition times for e-beam were prohibitively long.

Resists

Photolithography resists are similar to electron resists but are sensitive to UV radiation rather than electrons. As with electron resists, the liquid is deposited onto the surface of a substrate. To achieve a uniform layer, the sample was first attached to a vacuum chuck, then spun with the resist at a known rate for a set period of time. The solution in which the resist was dissolved was then evaporated through baking. For photo-resists, the spinning rate is 3000 rpm for 60 s with subsequent baking for 30 minutes at 90 °C. The variation in spinning speed and baking temperature between photo and electron resists is due to the different polymers used for the resists.

The developer used in the case of photoresists is microposit concentrate which is diluted in de-ionised water to a concentration of 1:1. The substrate was immersed in the developer for 75 s and a pipette used to move the developer solution across the surface of the substrate. Development is halted by rinsing the substrate in de-ionised water and dried using a fast flow of nitrogen gas.

2.3 Etching

Two different etching techniques, wet etch and dry etch were used to remove material from the substrate. Wet etch was used most frequently in this research

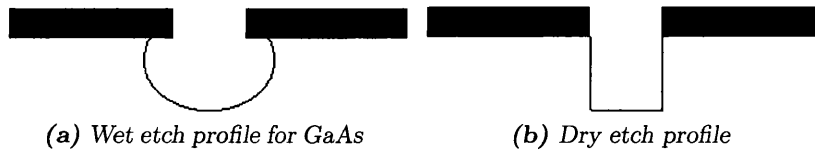


Figure 2.6: Etch profiles for wet and dry etch

with dry etch employed for the fabrication of electron transparent windows.

2.3.1 Wet etch

The process of wet etch removes material from the substrate by immersion of the sample in a corrosive solution. The resist covering areas of the substrate not requiring to be etched is impervious to the etch solution and thus leads to only the desired areas being patterned.

Whilst this technique is useful for removing areas of material, it does not lead to an edge profile with vertical walls due to the nature of the etch. Depending on the material to be etched, the profile will differ. For GaAs, once the etch has removed the surface, the side walls are also attacked giving a profile shown schematically in Fig 2.6. However, for (100) oriented Si, due to the (111) plane being more closely packed than the (100) plane, the etch proceeds anisotropically with a 45° angle leading to a V shaped profile. Anisotropic etches are much less common in GaAs as the surface activity of the (111) Ga and (111) As faces are very different.

The wet etching technique is useful for larger sized features. It is not, however, suitable for small features as the width of the etch increases with the depth of the etch.

2.3.2 Dry etch

Dry etch removes material by directing ions at the substrate, the ions being of a species likely to attack the material to be removed. The resist coating is not totally impervious to the ion bombardment but is removed at a slower rate than the material to be etched. The two main advantages of this technique over wet etch are that (1) the ions are directed such that an etch profile can be produced which has vertical walls and (2) there is greater uniformity over the substrate than with wet etch, Fig 2.6. There is however, one principal disadvantage of damage to the substrate from the ion bombardment. This can result in implantation of ions near the surface and damage at and below the surface of the substrate.

2.4 Metallisation

Two different metallisation techniques were employed to deposit metal onto the surface of the substrates. Evaporation was most commonly used in this research. Sputtering, the second technique, was carried out at the University of Leeds [29].

For both metallisation techniques, the bi-layer of resist was used with the metal to be deposited being less than one third the thickness of the resist layer. This gave an overhanging resist profile as shown in Fig 2.5. This overhanging profile helped prevent a build up of excess metal at the edges of the areas to be metallised. This build up is known as edge flags. Edge flags arise from the evaporated or sputtered metal hitting the sample at an angle rather than perpendicular to the surface and can cause difficulties, especially in magnetic samples. Here, out of plane fields may be stronger near the edges. The flags can also act as nucleation points for domains.

For non solid substrates, such as electron transparent windows, the undercut profile of the resist bi-layer will be less due to the lack of back scattering

described previously. This can lead to problems with edge flagging in elements patterned onto TEM windows.

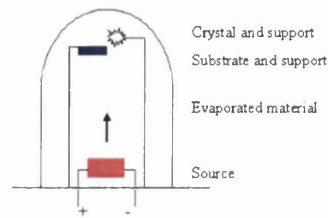
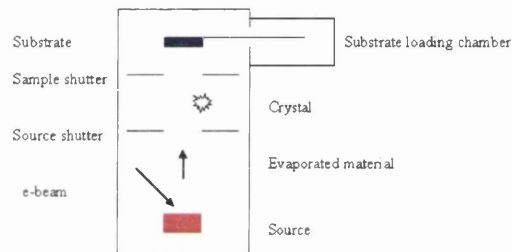
Before metallisation takes place, a wet etch must be carried out in order to de-oxidise the surface of the substrate and enable improved adhesion of the metal to the substrate. This etch which is usually carried out just before the substrate is put into vacuum for metallisation uses a 20:1, $H_2O:HCl$ solution for 20 s.

2.4.1 Evaporation

In the technique of evaporation, the material to be deposited was heated until thermal evaporation occurred. The sample was exposed to the resulting beam of evaporated material until the desired layer thickness was deposited. Evaporation must take place under high vacuum to ensure that the evaporated atoms travel directly from the source to the substrate and also to minimise contamination from other materials.

Two different techniques were employed to heat the material for deposition. The first used a conducting crucible into which the material to be deposited was placed. The crucible and metal for deposition were heated to an appropriate temperature by means of passing a high current through the crucible. Once a steady evaporation/deposition rate had been achieved the sample was exposed and the material deposited. The principal evaporator which uses this technique is housed within the Physics department, Fig 2.7a. It can evaporate only one metal at a time. To add a second layer the system would have to be let up to air and the crucible changed. This introduces a risk of oxidisation between layers due to the system being let up to air. This system is therefore only appropriate for single layers of metal.

In the second technique, material for deposition was heated by use of a focused electron beam. The equipment was a Plassys MEB450, Fig 2.7b situated

(a) *Physics evaporator*(b) *Plassys MEB450***Figure 2.7:** Schematic diagrams of the evaporators

within the Electronic and Electrical Engineering Department of the university. The Plassys MEB450 system uses a number of different crucibles which can be rotated, thus enabling the desired material to be evaporated and multilayers to be evaporated without exposing the sample to air. An electron beam is focused onto the surface of the material to cause heating and subsequent evaporation. Again, once a steady rate of deposition has been achieved, typically ~ 0.4 nm/s, the substrate is exposed. The crucible selection, application of the electron beam for heating the material and layer thicknesses are computer controlled enabling multilayers to be easily deposited.

In both systems a quartz crystal is used to determine the rate of deposition. The crystal undergoes mechanical oscillation and is exposed to the evaporated material. As the thickness of material deposited onto the crystal increases, the mechanical resonant frequency of the crystal decreases. For each material

a calibration is made correlating frequency drop with thickness of deposited layer, giving an accurate indication of layer thicknesses.

2.4.2 Sputtering

Using the technique of sputtering, the material to be deposited is removed from a source by the impact of energetic particles. The removed atoms build up and form layers on any surface upon which they land.

In DC Magnetron sputtering, the source is a negative electrode. The sputtering chamber is filled with argon gas which becomes ionised by the electrode voltage giving a glow discharge plasma. Permanent magnets behind the electrode produce a toroidal field thus confining the plasma over the target. Ar^+ ions are attracted towards the negative electrode and collide with it with a kinetic energy of hundreds of electron volts. These collisions remove material from the source leading to deposition onto the substrate Fig 2.8.

The sputtering machine used is at the University of Leeds. It has six sources and 15 sample slots, thus enabling multilayer systems to be grown and multiple samples to be fabricated without breaking the vacuum. The system is computer controlled and has a deposition rate of ~ 0.3 nm/s. No in situ thickness monitoring is used with this machine and the thickness is determined by sputtering time. A specimen, with a 100s deposition of the sputtered material is investigated by x-ray techniques to determine the deposition rate. The targets are Cu, Co, Py (NiFe), IrMn and Ta. The targets are not kept permanently on during the deposition of the specimens and are ignited as required. A set delay between ignition and exposing the sample is used to achieve a steady deposition rate before sputtering of the specimen. Magnetic samples can be grown in an in-plane bias field, known as the growth field. For this system, the growth field is supplied through a 200 Oe permanent magnet between the shutter and substrate.

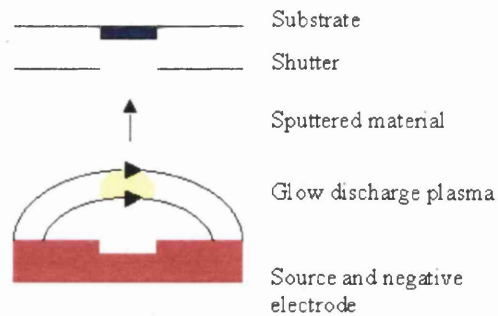


Figure 2.8: Schematic of the sputtering process

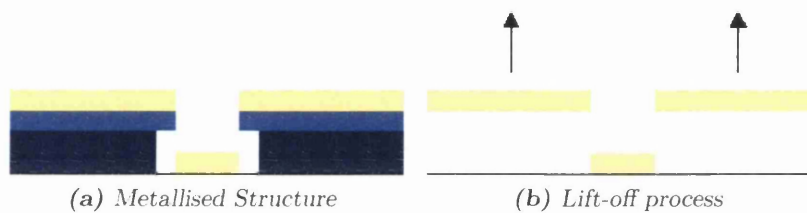


Figure 2.9: Schematic of the lift-off process

2.5 Lift-off

Lift-off is the technique employed to remove excess material after metallisation. For the positive resists used, the metal was in contact with the substrate only in the patterned regions. Elsewhere it lay on top of the resist layers. The excess metal was removed by dissolving the resist layers on which it was deposited, Fig 2.9. The resist was dissolved by placing the metallised substrate into warm acetone. For large features the resist will be removed in a matter of minutes but for smaller features a longer lift-off time is required. Once the excess metal has floated free of the substrate the substrate was removed from the acetone, rinsed in IPA and dried using a nitrogen gun.

2.6 Wafer cleaning

The majority of the techniques described above were carried out within the cleanrooms at the Nanoelectronics Research Centre of the Electronics and Electrical Engineering Department at the University of Glasgow. Sample preparation, wet etching and metallisation took place in a class 100 cleanroom, the specification of which is that the air within contains fewer than 100 particles of diameter greater than $0.5 \mu\text{m}$ per cubic foot. It is essential to carry out fabrication in this controlled environment to ensure high quality specimens. Contamination can alter the properties of the material to be investigated and therefore must be kept to a minimum. To help achieve this, users are required to wear protective clothing consisting of a cleanroom suit, gloves and hat. This reduces dust or fibres from clothing contaminating the air; and dirt, oils and salts being transferred from hands to the substrate. The suit and gloves also confers protection to the user from the chemicals used.

An important technique to further improve the fabrication of high quality reproducible samples is wafer preparation and cleaning which helps remove the surface contamination which can arise between wafer growth and sample preparation and is carried out using highly pure organic solvents. The wafer is cleaned by immersion in acetone in a clean beaker and subjected to an ultrasonic bath at room temperature for 5 minutes. It is then rinsed in isopropanol (IPA), again for 5 minutes in an ultrasonic bath. IPA is chosen as it is stable in air and does not leave prominent drying marks. The wafer is then dried using a fast flow of nitrogen gas. This process is repeated frequently between fabrication steps if contamination occurs.

2.7 Example

An example of a standard e-beam fabrication step involving metallisation and lift off is shown below. For an etching step, the final two stages are altered to include the etch and a 2 minute soak in acetone followed by a rinse in IPA and drying in the flow of nitrogen gas to remove the remaining resist.

<i>process</i>	<i>action</i>	<i>timing</i>
cleaning	acetone and ultrasonic bath	5 minutes
	IPA and ultrasonic bath	5 minutes
	dry in nitrogen	
depositing resist	spin resist at 5000rpm	60 s
	bake at 180 °C	30 minutes
	spin resist at 5000rpm	60 s
	bake at 180 °C	1 hour
writing of pattern	submit job to beamwriter	1 night
develop	MIBK : IPA warmed to 21 °C	60 s
	rinse in IPA	30 s
	dry in nitrogen	
metallise	de-oxidisation etch	20 s
	evaporate metal	10 - 40 minutes
lift-off	acetone and heatbath	20 minutes - 3 hours
	rinse in IPA	30 s
	dry in nitrogen	

Chapter 3

Transmission Electron

Microscopy of Artificial

Antiferromagnetic Thin Film

Spin Valves

3.1 Introduction

Spin Valve systems, introduced in section 1.5.1, are magnetic multilayer systems which exhibit GMR. These systems, which have been investigated for 12 years, are of industrial and commercial importance. This is due to a high level of sensitivity inherent in their structure which has led to applications such as sensors in magneto-recording media [16, 30, 31, 32, 33]. The general layer structure has three forms. The first, known as a top spin valve, is shown in Fig 3.1a. Fig 3.1b and Fig 3.1c represent a bottom spin valve and a double spin valve respectively. The standard layer structure was first proposed by Dieny et. al [34] and has been the subject of much research since. Dieny (1994) [15] provides a general review of some of the earlier work on SVs, Nogues(1999)

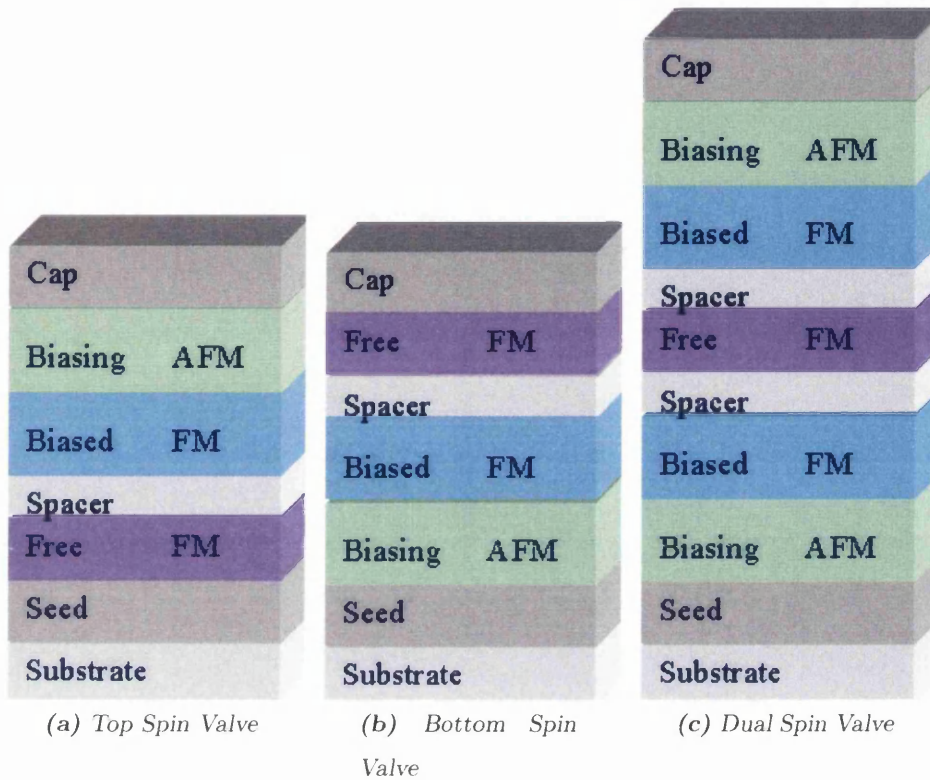


Figure 3.1: Schematic of the different SV formats

and Berkowitz(1999) [17, 18] illustrate some of the more recent research.

The principles behind the interlayer coupling mechanisms were briefly introduced in section 1.5.1. For a conventional exchange biased spin valve (CSV), similar to that shown in Fig 3.1a, limitations in sensitivity and dynamic range exist due to the magnetostatic coupling between the pinned layer and the free layer. This interaction is known as orangepeel or Néel coupling and leads to an offset hysteresis loop when investigating the free layer reversal processes [35]. In some applications, for example sensors, it is more desirable to have the free layer reversal process centred round zero field. This has led to modifications in the CSV layer structure.

As discussed in section 1.5.1, RKKY coupling can lead to ferromagnetic or anti-ferromagnetic coupling [12, 13, 14]. Combining this with a CSV as shown

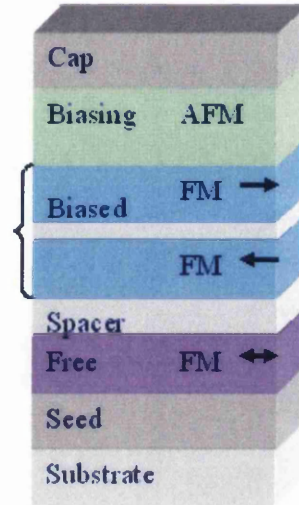


Figure 3.2: Schematic of an AAF biased SV

in Fig 3.2 gives a modified pinned or biasing layer. This modification improves the thermal and magnetic properties of the SV, see section 4.1. Also, when patterned, the ability to “tune” the edge field coupling between the pinned and free layers of magnetic elements by modification of the two Co layer thicknesses within the AAF reduces the effects of the magnetostatic coupling. A further advantage is the large effective exchange pinning field which increases the magnetic stability of the material. This modification results in Synthetic Anti-ferromagnetically (SAF) or Artificial Anti-ferromagnetically (AAF) biased SVs. Such a layer structure was first reported in 1996 [36, 37] and has been studied by a number of groups since [38, 39, 40, 41, 42, 43].

The results reported in this chapter and in chapter 4 were carried out on AAF biased SV structures. Both thin films and elements have been investigated. This chapter covers the research undertaken on thin films; chapter 4 reports the work undertaken on SV elements.

The magnetic samples were investigated using transmission electron microscopy (TEM) which will be introduced in sections 3.2 and 3.3. A discussion

of the sample fabrication process and results obtained follow.

3.2 Transmission Electron Microscopy

Transmission Electron Microscopy has been used as a technique to facilitate in-situ studies of the magnetic reversal process of samples for many years [44, 45, 46, 47, 48]. The principal microscope used for this research was the modified Phillips CM20 electron microscope within the Department of Physics and Astronomy at the University of Glasgow. The discussions on instrumental requirements and imaging methods which follow refer specifically to the CM20 electron microscope when required.

3.2.1 The Electron Gun

The gun system provides the electron source for the microscope. A small negative source emits electrons which are focussed and accelerated to typically ~ 40 keV by an electrode. These electrons are further accelerated by a series of anodes to give electron energies of up to 400 keV, depending on the microscope system, Fig 3.3. The CM20 operates with electrons of an energy up to 200 keV, using the standard equation,

$$\lambda = \frac{h}{(2meV_r)^{1/2}} \text{ where } V_r = V_0 \left(1 + \frac{eV_0}{2m_0c^2} \right), \quad (3.1)$$

where V_0 is the accelerating potential and v_r is an effective potential which accounts for relativistic correction. This gives an electron wavelength of 0.0251 Å at 200 keV, typically the accelerating voltage used on the system.

Two types of electron gun, the thermionic gun and field emission gun (FEG) are in common use. Each type of gun uses a different emitter. The two most common emitters for a thermionic gun are a tungsten (W) filament or a lanthanum hexaboride (LaB₆) filament. The LaB₆ gun has a brightness (defined as the current density per steradian) 10 times that of the tungsten

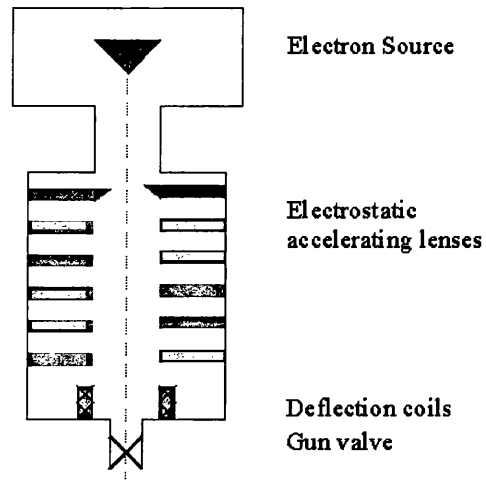


Figure 3.3: The electron gun

filament. A FEG makes use of either a (thermally assisted) cold field emitter or a Schottky emitter and has a brightness around 1000 times that of the tungsten filament.

The gun used on the CM20 is a Schottky FEG. It provides an almost point source, is highly coherent, has significantly higher brightness than either of the thermionic guns and has greater stability than the cold FEG. The cathode is a small tungsten tip coated in zirconia (ZrO_2) to reduce the work function, i.e. increases the ease with which electrons are emitted, which in turn enhances emission.

3.2.2 The column

The electron beam emitted from the gun is manipulated by lenses within the microscope to illuminate the specimen. The resulting image is then projected by lenses below the specimen onto a suitable viewing medium. This section discusses the lenses and their functions within the microscope. Fig 3.4 shows a schematic diagram of the CM20 including the lens and detector positions.

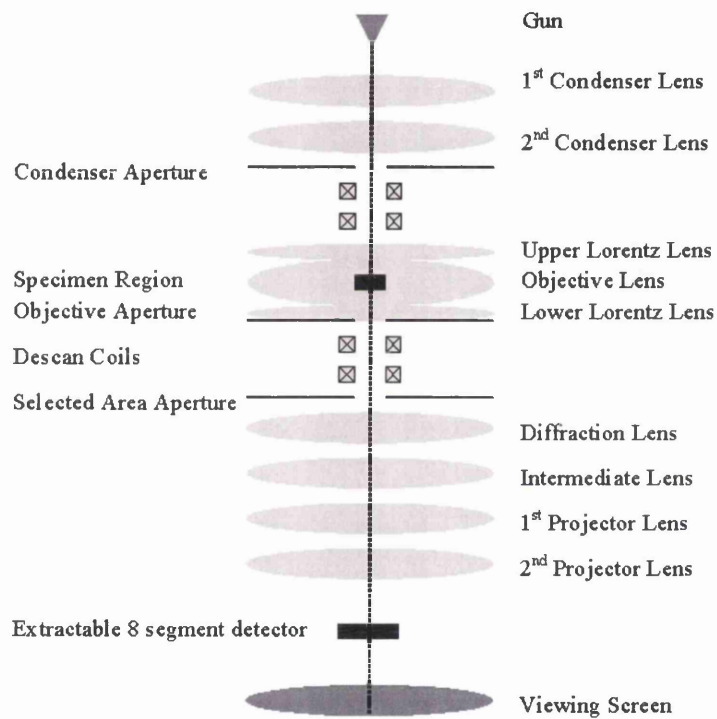


Figure 3.4: Schematic of the modified Phillips CM20

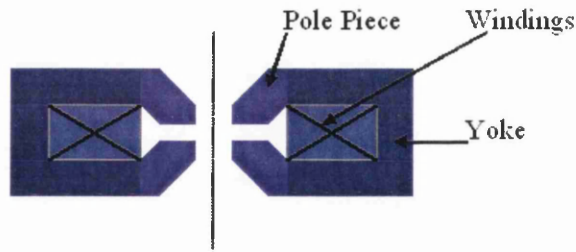


Figure 3.5: The structure of a magnetic lens. The axially symmetric field increases in strength as you move away from the electron axis. This produces a stronger focusing effect on off-axis electrons.

Magnetic lenses and their aberrations

All lenses in the CM20, with the exception of the gun lens, are electromagnetic. Magnetic lenses have smaller optical aberrations than their electrostatic counterparts and can work with greater ease at high voltages. A magnetic lens consists of an iron pole piece and a yoke which contains windings and a cooling system and enables the lens to be dc energised, Fig 3.5. The pole piece produces an axially symmetric focussing field for the electrons and, by altering the current through the windings, the focal length of the lens can be adjusted. The most commonly used magnetic lenses are similar to that sketched in Fig 3.5 and are cylindrically symmetric. The column and lenses are cylindrically symmetric. Due to imperfections in the lens and hence the cylindrical symmetry you can only have 3^{rd} , 5^{th} etc order aberrations due to the deviation changing sign on opposite sides of the lens. Lens aberrations limit the ultimate resolution of the microscope. Three main types of aberrations, all third order, will be described with here, spherical, astigmatism and chromatic. These aberrations can be corrected with the use of quadropole and octopole magnetic lenses.

Spherical aberration

Spherical aberrations arise from the lens field acting inhomogeneously on off-axis

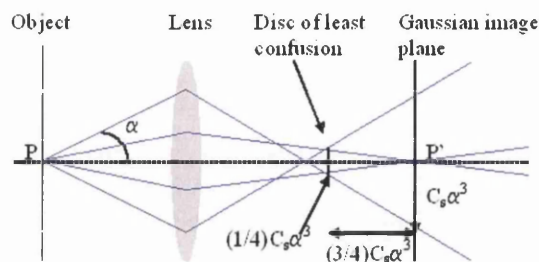


Figure 3.6: Spherical aberration

electrons with the consequence that electrons further from the column axis experience a stronger focussing effect than those closer to the axis. Consequently, rays close to the axis are focussed at the Gaussian image point whereas off axis rays are focussed before the Gaussian image point. Thus, the beam cannot be focussed to a point and instead is focussed to a plane where the beam has a minimum diameter, Fig 3.6. This is known as the disc of least confusion. The radius of this disk is

$$r_s = \frac{1}{4}C_s\alpha^3 \quad (3.2)$$

where C_s is the spherical aberration coefficient of the lens and α is the lens semi angle (see Fig 3.6). The position of the disc is

$$\frac{3}{4}C_s\alpha^3 \quad (3.3)$$

from the Gaussian image point. This form of aberration limits the overall resolution of the microscope.

Astigmatism

Astigmatism occurs when the electrons experience a non uniform magnetic field which produces two line foci normal to each other, P_h' and P_v' separated along the axis. As the focus is moved along the axis the line change to an ellipse, a circular disc, back to an ellipse and then a second line focus at 90° to the original line focus, Fig 3.7. This gives a disc of least confusion with

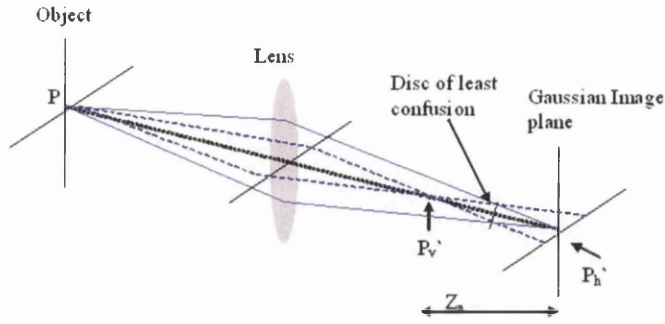


Figure 3.7: Astigmatism

diameter

$$d = Z_a \alpha \quad (3.4)$$

where Z_a is the distance from the disc of least confusion to the Gaussian image plane. This type of aberration can be corrected by small octopoles, known as stigmators whose compensating field cancels out the effects of astigmatism. To correct astigmatism, the CM20 has two sets of stigmators, the first corrects the condenser lens system and the second the objective astigmatism.

Chromatic Aberration

Chromatic aberration arises from three sources, the lens power supplies, the electron beam itself and energy loss due to the electron-specimen interaction. Fluctuations in the lens power supplies can have $\frac{\Delta V_r}{V_r} \simeq 10^{-6}$ for the eht supply and $\frac{\Delta I}{I} \simeq 5 \times 10^{-7}$ for the objective lens with ΔV_r and ΔI being the variation in supply voltage and current. The electron beam can have an energy spread of greater than 0.5 eV ($\frac{\Delta E}{E} \simeq 2 \times 10^{-6}$) and there is an energy loss of approximately 20 eV per 100 nm of specimen thickness for specimens with a mid-range atomic weight such as the transition metals used for the spin valve specimens investigated in this project. The specimen itself can be seen to be the greatest contributor to the chromatic aberration.

The electron focal length depends on its energy. Electrons with a lower

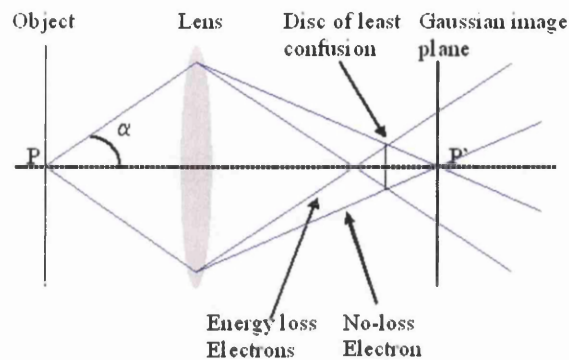


Figure 3.8: Chromatic aberration arising from specimen

energy will experience a greater deflection from the lens field than those with a higher energy, Fig 3.8. This again leads to a disc of least confusion with

$$r_c = C_r \alpha \frac{\Delta E}{E} \quad (3.5)$$

where C_r is the chromatic aberration coefficient, α the semi-angle of the lens, E is the initial beam energy and ΔE the variation in energy.

Condenser lenses and aperture

The condenser system illuminates the specimen with electrons. The configuration employed by the CM20 is the standard configuration which consists of two condenser lenses and an aperture.

The first condenser lens is used to demagnify the beam source and to alter the spot size. The second lens projects the demagnified beam from the first condenser lens on to the specimen and enables the operator to control the illuminated area by focusing/defocusing the illumination on the specimen. The condenser aperture controls the angular variation in the beam. As a smaller spot size is used and the aperture diameter decreased, the coherence of the beam increases.

Objective lens and aperture

In standard microscopes, the specimen is inserted close to the centre of the objective lens. This pre specimen part of the objective lens also contributes to the illumination conditions by focussing the beam onto the specimen. The post specimen part of the objective lens forms an image of the sample which is then, in the simplest case, projected onto a viewing screen by subsequent lenses. Due to its inherent aberrations, the objective lens is the most influential in determining the resolution of the microscope as subsequent lenses deal with a magnified image and as such, their aberrations have a smaller effect. The strength of the lens and hence the magnetic field produced subject the sample to applied fields great enough to erase any domain structure and hence render it unsuitable for imaging magnetic materials. To circumvent this, the CM20 has a set of upper and lower twin lenses added to the column, as shown in Fig 3.4. These lenses enable operation of the microscope with the objective lens turned off leaving the specimen in a field free region. In this mode of operation, the objective lens can be weakly excited to apply a small magnetic field perpendicular to the sample plane. By controlled tilting of the specimen, this objective lens field can be used to alter the magnetic state of the specimen thereby enabling in-situ magnetising experiments.

The objective aperture is situated at the bottom of the pole piece gap of the objective lens. This is used to enhance diffraction contrast images and for Foucault imaging, neither of which will be discussed in any detail as they are not relevant to the work reported in this thesis.

The selected area aperture below the objective system enables diffraction patterns to be obtained from specific areas of the sample.

Diffraction, intermediate and projector lenses

These lenses are situated below the sample in the column and are used to magnify the image obtained from the second part of the objective lens and project the image onto an appropriate viewing medium. The first intermediate lens is also known as the diffraction lens. The strength of this lens determines whether an image or a diffraction pattern is observed. The other intermediate lenses compensate for any image rotation and the projector lens projects the image onto the viewing screen or other viewing media.

Further information on transmission electron microscopy can be found in Williams and Carter [49].

3.3 Observation of Domains by TEM

3.3.1 Beam and sample interaction

One of the challenges of observing magnetic domains is that the specimen is usually immersed in the high magnetic field of the objective lens when using a standard TEM. This field is large enough to erase the domain structure from the sample. As discussed previously, the modified CM20 has twin Lorentz lenses which enable a field free region around the specimen and allow magnetic imaging (section 3.2.2).

The methods of imaging magnetic structures employed here involve a branch of microscopy known as Lorentz microscopy. Lorentz microscopy can be used to describe all imaging modes where contrast is observed as a result of electron deflection from the beam passing through a magnetic specimen.

Assuming the incident electron beam lies along the z axis, any deflection will be along the x axis which relates to the magnetic induction of the material. Classically, the Lorentz deflection angle $\beta_{\mathbf{L}}$ is given by

$$\beta_{\mathbf{L}} = \frac{e\lambda t}{h}(\mathbf{B} \times \mathbf{n}) \quad (3.6)$$

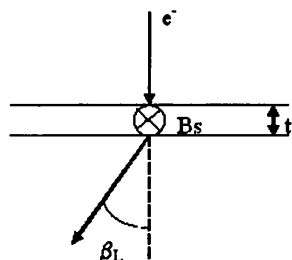


Figure 3.9: The Lorentz deflection

where e is the electron charge, λ the wavelength, t the sample thickness, h is Planck's constant, \mathbf{B} is the magnetic induction inside the investigated area and \mathbf{n} is a unit vector along the direction of travel of the beam. β_L is rarely larger than $100 \mu rad$. Confusion between the magnetic deflection angle, β_L , and the Bragg crystallographic scattering angle is unlikely as the Bragg scattering angle tends to be around $1 - 10 mrad$.

For a specimen of constant thickness and no stray fields,

$$\beta = \frac{eB_s\lambda t}{h} \quad B_s = \mu_0 M_s \quad (3.7)$$

where B_s is the magnetic induction of the specimen and is perpendicular to the beam (Fig 3.9).

To enable quantitative analysis of a system, a quantum mechanical description is required. For this, the magnetic film is considered as a phase modulator of the incident electron wave. The gradient of the phase shift

$$\nabla\phi = \frac{2\pi et}{h}(\mathbf{B} \times \mathbf{n}) + \frac{\pi\nabla(Vt)}{\lambda E_0}. \quad (3.8)$$

The symbols represent the same parameters as introduced in the classical description with the addition of V , the inner potential and E_0 the electron energy. This quantum mechanical description takes into account both the electrostatic interaction and the interaction arising from the magnetic induction of the specimen. For specimens of constant thickness, for example thin films, the electro-

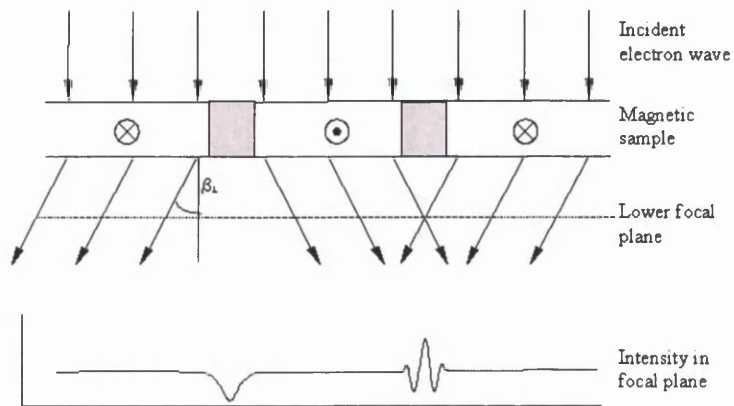


Figure 3.10: Schematic of Fresnel microscopy

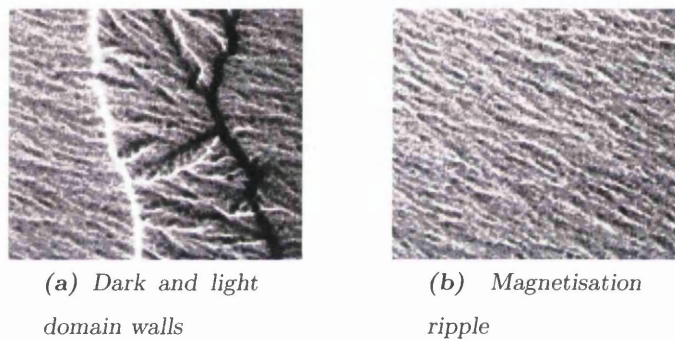


Figure 3.11: Fresnel images of domain walls and ripple

static term is small compared to the term arising from the magnetic induction. Hence, Lorentz microscopy is a branch of phase contrast electron microscopy. For magnetic elements there is an abrupt change in thickness at the edge of the element and therefore a much more substantial electrostatic contribution. However, the specimen still remains a pure phase object [44, 45].

3.3.2 Lorentz microscopy

Fresnel

Fresnel microscopy is one of the most commonly used imaging modes for studying magnetic materials. In this mode, the imaging lens is defocussed so that the object plane no longer coincides with the specimen plane, Fig 3.10. Contrast arises wherever there is a varying component of magnetic induction (i.e. domain walls and ripple). Domain walls are observed as bright and dark bands on the image which represent convergent and divergent domain wall images, Fig 3.11a. Magnetisation ripple is where the moment varies around the mean magnetisation direction. This results in a wave like pattern or ripple in the Fresnel image perpendicular to the mean magnetisation direction, Fig 3.11b. The interference fringes observed in the Fresnel image of the convergent wall arise due to the wave nature of electrons. The simple ray treatment in the schematic is therefore incomplete. It is, however, useful for a simple description of the technique.

Fresnel microscopy is frequently used due to its operational simplicity. It gives fairly high levels of contrast and there is no preferred directionality. However, no information is directly available about the direction of magnetisation within a domain and in the absence of magnetisation ripple, it is difficult to observe the angle through which the magnetisation rotates during reversal.

Differential Phase Contrast Imaging

Differential phase contrast (DPC) is a scanning transmission electron microscopy (STEM) technique whereas Fresnel imaging uses the microscope in a conventional transmission electron microscopy (CTEM) mode. The difference between the two is that for CTEM, a comparatively large beam illuminates the region of interest enabling information to be collected over the entire area simultaneously. For STEM, a small, often coherent probe scans in a regular

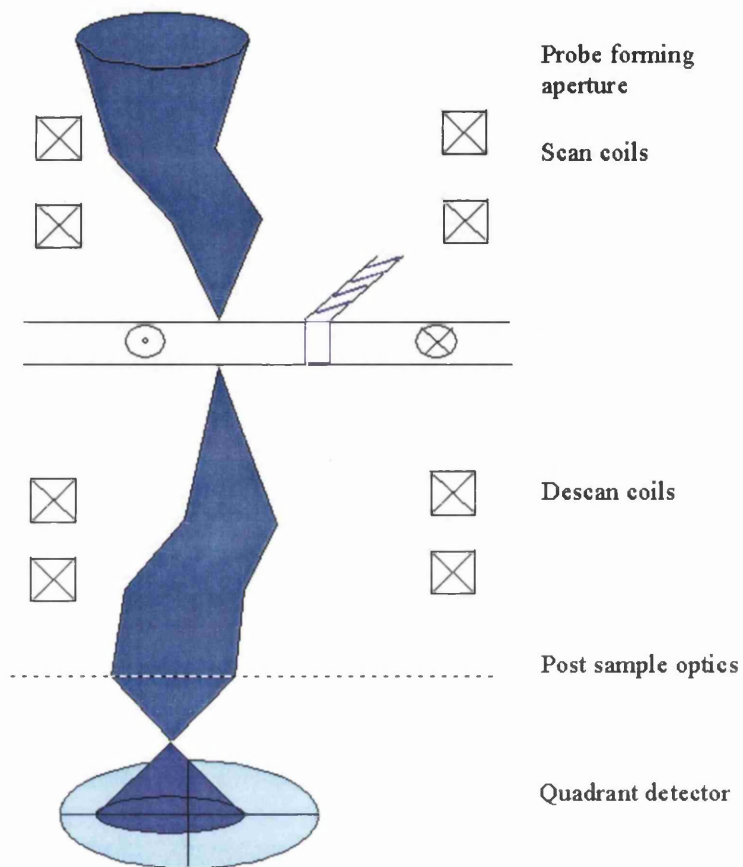


Figure 3.12: Schematic of DPC microscopy

raster pattern over the area required. Each pixel of the raster pattern is then displayed electronically to obtain an image of the whole region of interest.

The probe undergoes a Lorentz deflection due to the magnetic induction in the local area over which the probe is centred, Fig 3.12. This is imaged using a segmented detector placed above the viewing screen (see Fig 3.4 for the position of the detector and Fig 3.13a for a schematic of the detector). Taking the difference between signals from opposite segments gives a direct measure of the two components of $\beta_{\mathbf{L}}$. These can then be combined with the signals from all other pixels included in the scan area to form an overall description of

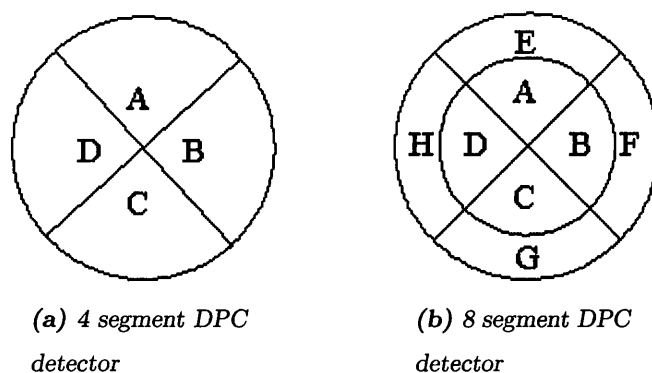


Figure 3.13: DPC detector configurations

the component of magnetic induction perpendicular to the electron beam. It is also possible to sum the signals from all quadrants of the detector to obtain a standard bright field image.

DPC is useful as it enables images to be analysed quantitatively [48] and information to be obtained about the direction of magnetic induction within a domain. However there is a significant increase in instrumental complexity and operational difficulty and, due to this being a scanning technique, the image recording times are longer.

A further disadvantage of Lorentz microscopy in general is that the phase information of a real specimen contains magnetic and non-magnetic contributions. This can make observation of magnetic contrast very difficult, especially on smaller samples with little contrast, hence giving possible difficulties in the observation of magnetic contrast when using DPC imaging.

The standard DPC technique introduced above can be improved to give enhanced magnetic contrast and is known as modified differential phase contrast (MDPC) imaging [50, 51, 52]. This technique uses an 8 segment detector, Fig 3.13b. The system is set up so that the beam diameter at the detector plane is just larger than the diameter of the inner quadrants of the detector. This means that when imaging a magnetic sample and taking difference signals

of the outer quadrants the magnetic deflection is much more significant and enhances the signal due to magnetic contrast.

3.4 Spin Valve Structure

The following describes the composition and function of the layer structure of the AAF biased thin film spin valves introduced in section 3.1. The layers were configured as follows:

Substrate/Ta/NiFe/Co/Cu/Co/Ru/Co/IrMn/Ta.

The Ta seed layer encouraged growth in the $\langle 111 \rangle$ direction and a textured fcc crystalline structure in subsequent layers. The NiFe/Co bi-layer acted as the free layer. The Co was used to enhance the GMR signal [30]. Enhanced GMR is desirable in future applications. The AAF itself was a Co/Ru/Co tri-layer. The thickness of the Ru was specified so that the two Co layers couple at the first antiferromagnetic alignment, section 3.1. A thinner layer of Ru could be non uniform with pin-holes giving direct contact between the two Co layers and hence ferromagnetic coupling. A thicker Ru layer reduces the GMR of the material. The IrMn biasing layer was selected due to a comparatively high blocking temperature which would permit the possibility of the material being used at higher temperatures in applications. The Ta cap acted as a protective layer by preventing corrosion of the magnetic layers through oxidisation.

A series of 10 thin film samples was investigated. All 10 specimens were fabricated in the same growth run and under the same growth conditions at the University of Leeds. In each sample, only the second Co layer of the AAF was varied, the rest of the layers in the structures remained unchanged. In the first sample the thickness of the second Co layer was $\frac{1}{4}$ the thickness of the first Co layer with the last sample having the second Co layer twice the thickness of the first.

All samples were grown onto a substrate which incorporated $100 \times 100 \mu\text{m}^2$ electron transparent silicon nitride (Si_3N_4) windows. The TEM windows were fabricated within the Electronic and Electrical Engineering Department. Sample growth was carried out in a DC magnetron sputtering machine in conjunction with Dr Chris Marrows at the University of Leeds. A description of the sputtering technique can be found in section 2.4. The samples were grown in a 200 Oe field parallel to the plane of the sample.

The layer thicknesses in Å of each sample were:

Substrate/Ta 47/NiFe 64/Co 7/Cu 31/Co 60/Ru 7/Co **X**/IrMn 107/Ta 32

where **X** = 14, 25, 37, 48, 60, 71, 83, 94, 106, 117 for samples 1...10. The uncertainty in the layer thicknesses was less than 10%.

3.5 Physical Microstructure

Alongside the investigation into the free layer reversal, it was considered beneficial to investigate the physical microstructure of the specimens in order to permit an understanding of the physical properties of the material. They may also help with an explanation of any unexpected results in further analyses. The analysis of the physical microstructure was carried out in a JEOL 2000FX TEM. This TEM was similar to the CM20 in that it possessed a field free region at the specimen plane. However, in place of the twin lenses and principal objective lens of the CM20, the JEOL 2000FX had a modified objective lens with a large pole piece gap supplying the field free region. This enabled a structural study to be carried out without affecting the magnetic state of the samples.

Two sets of measurements were carried out. The first determined the grain size of the specimen, the second determined the lattice parameters of the materials present within the structure.

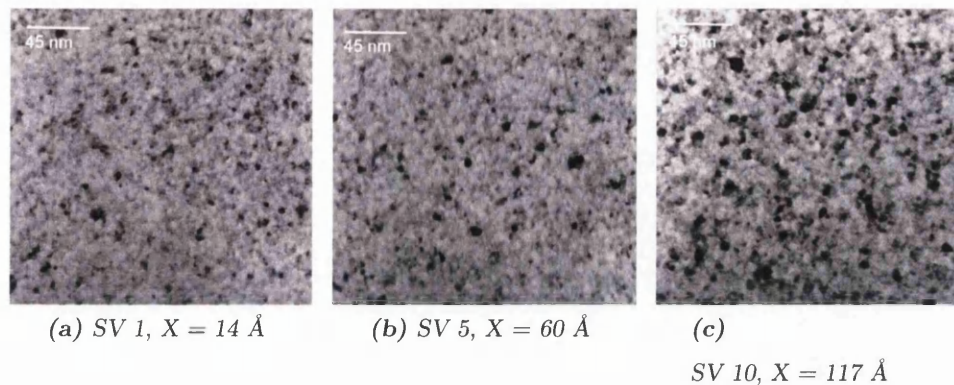


Figure 3.14: Bright field image of crystallites for samples 1, 5 and 10.

Bright field images of the crystallites from specimens 1, 5 and 10 are shown in Fig 3.14. The thickness of the second Co layer is specified in each case. Specimens 1, 5 and 10 were chosen as they represented a cross section of the specimen range. To determine the grain size, the bright field images were recorded at a magnification suitable for viewing the individual grains ($\sim \times 100 \text{ K}$). To calculate the average grain size, either the number of grains between two set points a known distance apart were counted or a number of individual grains were measured. Both these measurements were taken using the negative of the bright field image. The second method was the one employed in this case. Once the average grain size on the negative has been obtained, it was divided by the microscope magnification to obtain the actual grain size.

A plot of the crystallite size w.r.t. total sample thickness (Fig 3.15) indicated that the grain size increased with specimen thickness as expected. Grain growth is columnar and favourably aligned grains grow at the expense of those less favourably aligned. Therefore, as the thickness increased the maximum grain size would increase. The smallest grains were approximately 4 nm in size and were found in all specimens. As the total sample thickness increased, both the mean grain size and the spread in grain size increases. On closer inspection of the thickest specimen (SV 10), it was observed some of the largest grains

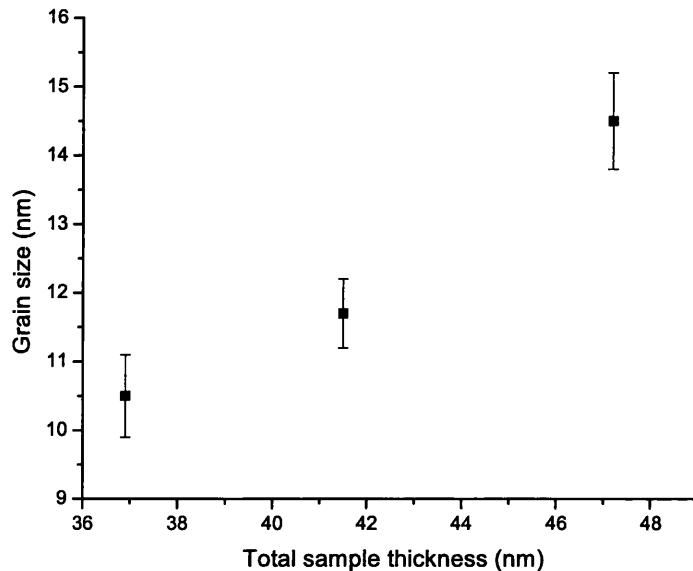


Figure 3.15: Variation in grain size with increasing sample thickness

observed (~ 20 nm) consisted of several smaller grains clustered together. It is possible these smaller grains had coalesced during deposition.

Diffraction patterns of the structure were recorded in order to evaluate the crystalline properties and level of texturing of the specimens. The diffraction pattern arose from the deflection of electrons from Bragg planes within the material. By measuring the radii of the diffraction rings and plotting R^2 vs $N(=h^2 + k^2 + l^2)$, the following equation could then be used to obtain the lattice parameter

$$a = \frac{L\lambda}{\sqrt{\frac{dR^2}{dN}}} \quad (3.9)$$

where L = camera length of the microscope and λ = electron wavelength.

Two diffraction patterns using the same camera length were used to determine the ring radii. Firstly an image was recorded with no specimen tilt and

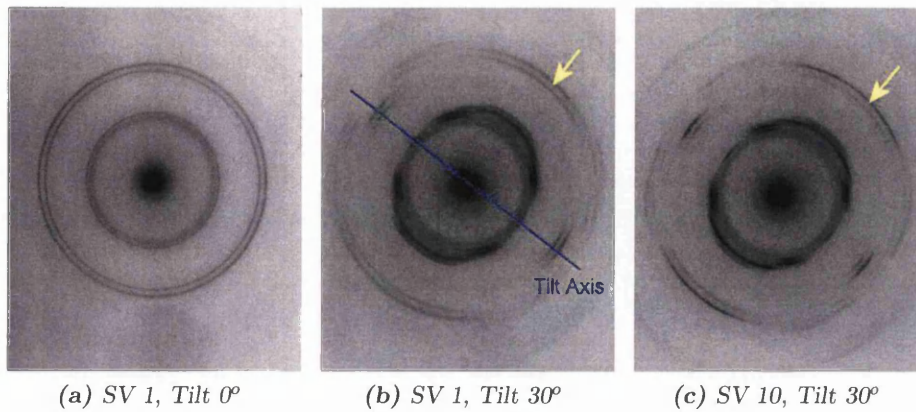


Figure 3.16: Diffraction patterns from specimens 1 and 10. Arrows indicate texturing in the specimens at 30° tilt. Specimen 10 was thicker and as such, had a better defined grain structure which increases texturing.

then a second was taken at a specimen tilt of 30° . Tilting the sample resulted in scattering from Bragg planes at a different alignment to those at 0° . A more precise calculation of the lattice parameters could be made by taking into account both diffraction patterns.

Fig 3.16a shows a diffraction pattern from sample 1 at 0° tilt, in which the rings were homogeneous due to the polycrystalline nature of the material. The second diffraction pattern, taken at a tilt of 30° , Fig 3.16b, shows additional Bragg reflections and considerable texturing. Comparison between the tilted diffraction patterns from sample 1 and sample 10, Fig 3.16c, indicated that texturing increased with overall specimen thickness as expected. Texturing is defined by the arc length, which has become slightly better defined. A large change was not expected as the overall thickness did not change dramatically. Also, the definition of the rings were sharper in the thicker specimen. This is due to electron diffraction off of a larger number of unit cells due to the larger grains giving more unit cells per crystallite.

The double ring structure observed in all diffraction patterns arose from

	a_{TM} (Å)	$\delta_{a_{TM}}$ (Å)	a_{IrMn} (Å)	$\delta_{a_{IrMn}}$ (Å)
SV 1	3.62	0.09	3.83	0.10
SV 5	3.61	0.09	3.81	0.10
SV 10	3.59	0.10	3.80	0.11

Table 3.1: Measured lattice parameters of Spin Valves 1, 5 and 10.

the different lattice parameters of the SV layer structure. The IrMn layer had a lattice parameter of $a = 3.82$ Å [43]. The transition metals all had a very similar, smaller lattice parameter of $a \simeq 3.61$ Å [43, 53] and are therefore indistinguishable on the diffraction pattern. The Ta seed and cap layers had a lattice parameter of $a = 3.3$ Å [53]. The thickness of the Ru layer is too thin to be resolved within the diffraction pattern.

Indexing of the diffraction patterns confirmed that the magnetic layers are fcc and are the layers which contribute to the double ring structure and texturing. It could also be observed that the Ta contributes an untextured background. The calculated lattice parameters for samples 1, 5 and 10 are presented in Table 3.1. From this, it can be seen that the measured lattice parameters agree within experimental error of the accepted values.

Further study of the tilted diffraction pattern showed that the (220) rings lay on the tilt axis which is consistent with a $\langle 111 \rangle$ zone axis. This confirmed that the Ta seed layer promoted $\langle 111 \rangle$ growth of subsequent layers as desired [54].

These studies of the physical microstructure confirmed that the grain size increased with specimen thickness and that the materials expected are present.

3.6 Magnetic Reversal

3.6.1 Introduction

Magnetic studies were undertaken on the ten samples. Each sample was first examined in the “as-grown” state, i.e. the magnetic state the film was in immediately after deposition. The easy axis reversal mechanism of the specimens was then investigated.

3.6.2 As Grown State

Fresnel images were taken in the CM20 of the specimens in the as-grown state by Dr Aitchison. The differences between the magnetic configurations supported by the films varied significantly with the thickness of the second Co layer in the AAF, Fig 3.17.

Magnetisation ripple was easily observed in the majority of the specimens, the only exception being specimen 7 which supported a very complex domain structure. The presence of magnetisation ripple indicated a preferred direction of magnetisation or easy axis within the film. It had been anticipated that a preferred direction would be observed due to the external field of 200 Oe applied during growth of the specimens. The magnitude of the ripple increased through specimens 1 to 5 (observable in Fig 3.17a-e). Specimen 7 had a highly complex domain structure. In specimens 8 to 10, the domain complexity decreased with the increase of the thickness of the second Co layer in the AAF and ripple was again observable.

It should be noted that specimens 1 to 6 showed considerably less domain structure than specimens 7 to 10. This change in domain complexity could have arisen from changes in the AAF coupling due to the increase in thickness of the second Co layer. As the second layer increased in thickness, it would have competed with the first layer to lie parallel the growth field direction.

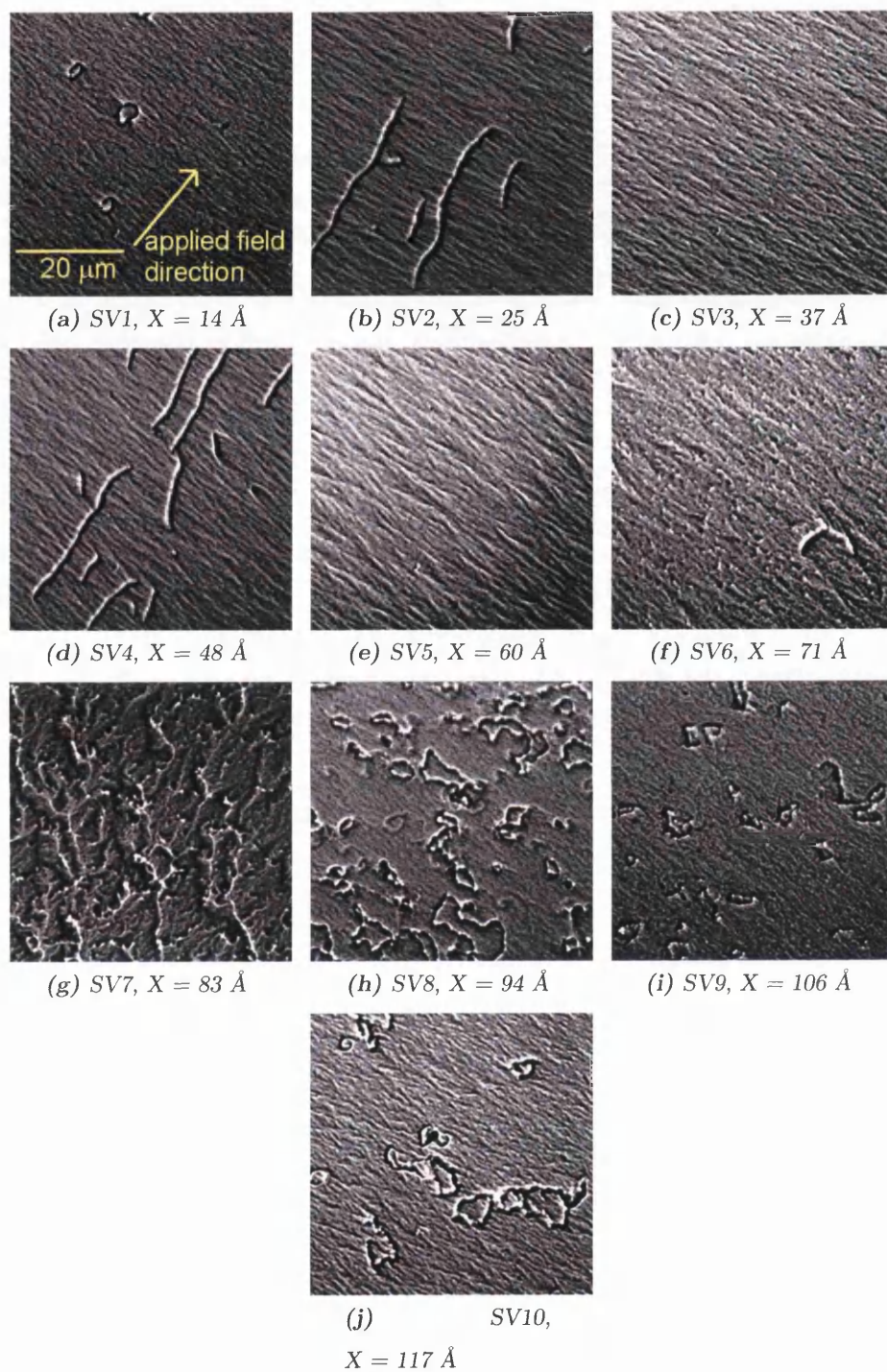


Figure 3.17: Fresnel Images of As Grown states of specimens. X is the thickness of the second Co layer within the AAF biasing trilayer.

For specimens 1 to 6 where the second Co layer of the AAF was either thinner or comparable to the first, the first Co layer would have remained parallel to the growth field direction. As the thickness of the second Co layer became significantly larger than that of the first (specimen 7), it is conceivable that the two layers could have formed a complex multi-domain state in the AAF which would have been pinned by the antiferromagnetic IrMn biasing layer. This would have mapped through to the free layer through non uniform weak coupling giving a complex domain state observable in the free layers and no easily identifiable preferred direction of magnetisation. As the thickness of the second layer increased further, the complexity of the AAF biased layer would have been reduced. Accordingly, a reduction in the number of domains in specimens 8 through 10 was observed.

3.6.3 Magnetising Experiments

In the studies described here, the easy axis reversal mechanisms of the free layer were investigated. The film was oriented in the microscope such that the applied field was parallel to the preferred direction of magnetisation in the free layer of the SV. As described previously, section 3.3.2, the preferred direction was deduced from the magnetisation ripple.

Following this, in a typical experiment, a high field was applied parallel to the specimen plane to align the free layer with the applied field. The strength of the applied field was subsequently reduced to enable observation of the reversal process. In this series, the reduced field was ~ 50 Oe and from this point, the field in the plane of the specimen was swept from $+30$ Oe to -30 Oe. The reversal process was recorded on a CCD camera below the viewing screen of the microscope. These fields correspond to an objective lens current of 50 mA providing a vertical field of ~ 50 Oe with the specimen plane being tilted $\pm 30^\circ$ from the horizontal. $\pm 30^\circ$ tilt is suitable for viewing

the reversal mechanism without experiencing significant foreshortening of the viewed image. The high field and reversal sweep was repeated for the opposite field direction and the Fresnel images of the reversal were again recorded. The in plane field range +30 Oe to -30 Oe was selected as this represented the range where most changes in the free layer magnetisation distribution took place whilst having negligible effect on the AAF coupling. A considerably larger field (> 7000 Oe) is required to alter the AAF coupling. Positive numbers in the applied field denote an applied field in the opposite direction to the preferred orientation of the free layer.

The reversal mechanisms for specimens 1, 4, 5, 7 and 10 are presented below. These provide a representative cross section of the domain reversal processes observed.

Sample 1

As introduced previously, the layer structure of sample 1 was:

Substrate/Ta 47/NiFe 64/Co 7/Cu 31/Co 60/Ru 7/Co 14/IrMn 107/Ta 32

with all thicknesses in Å.

The magnetic state of the sample was recorded as the externally applied field was reduced from a forward field of +30 Oe to a reverse field of -30 Oe. The Fresnel images of this outward reversal are shown in Fig 3.18a-e and illustrate the most important stages of the reversal process. Fresnel images of the return path are also shown, Fig 3.18f-l. As the images show, 360° loops, which proved remarkably difficult to eliminate, were a common feature of this sample. It was also observed that they had a tendency to be found in the same film locations on repeated cycles, suggesting that they were associated with specific micro-structural features. It must also be recalled that the images related to the projected induction distribution through the whole multilayer stack; as such it was difficult to ascertain in which magnetic layer(s) the 360°

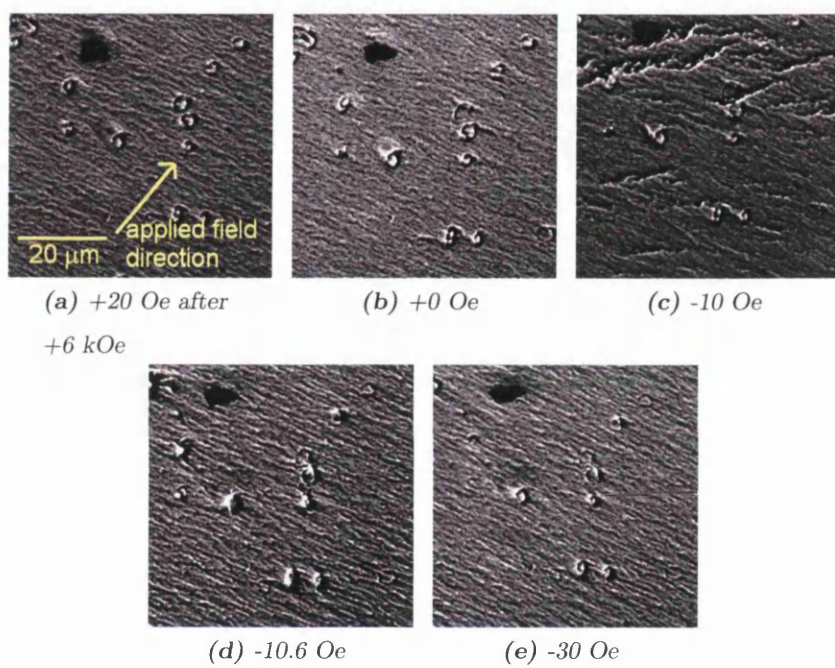


Figure 3.18: SV 1, $X = 14 \text{ \AA}$, Outward reversal

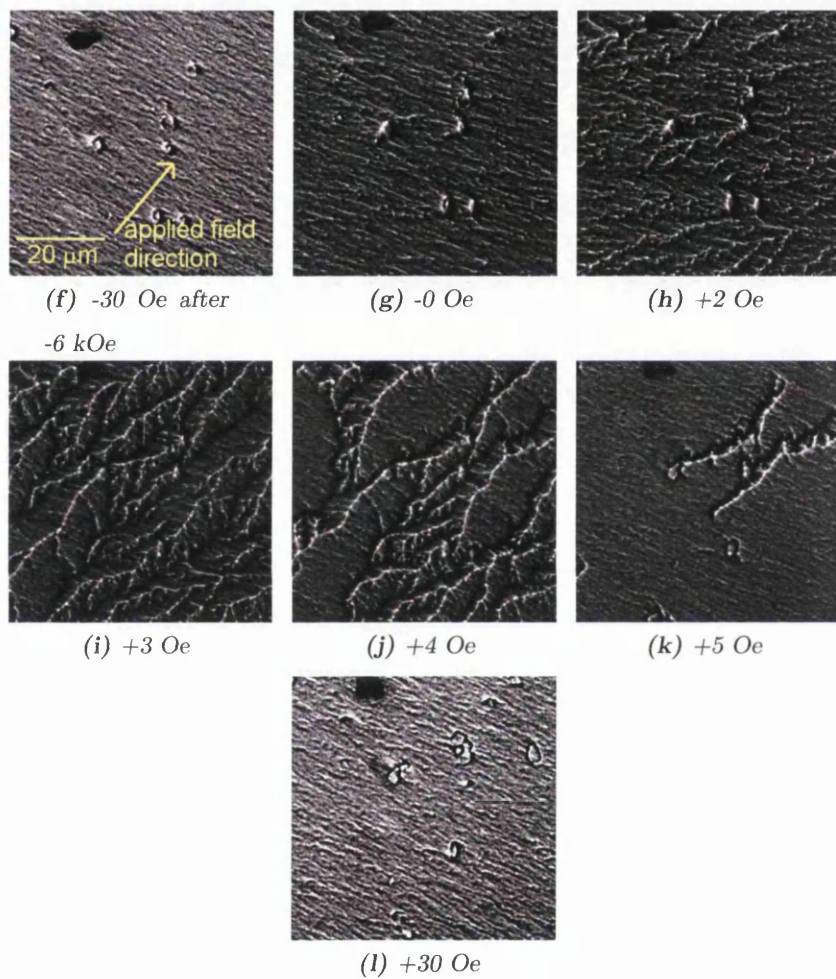


Figure 3.18: SV 1, $X = 14 \text{ \AA}$, Return reversal

loops formed. It is by no means certain that the loops were in the free layer as they seemed to play little if any part in the low field reversals that can clearly be observed in Fig 3.18. One theory is that the second Co layer of the AAF, being only $\simeq 14 \text{ \AA}$ in thickness did not form a complete layer and thus enabled the formation of pin holes between the Ru AAF spacer layer and the IrMn biasing layers.

Differences were observed in the way the free layer reversed on the outward and return paths of the magnetisation cycle. Along the outward path, Fig 3.18a-e, ripple intensified modestly before a rapid switch, involving a very small number of highly mobile walls, effected the reversal with the midpoint of the reversal occurring at an applied field of $\simeq -10 \text{ Oe}$. The reversal itself occurred so rapidly that it could not be recorded on the CCD camera. On the return path, Fig 3.18f-l, a more complex array of rather irregular walls were involved in the reversal at an applied field of $\simeq -3 \text{ Oe}$. The complex array persisted over a field range $> 1 \text{ Oe}$ with the consequence that details of its formation and evolution could be more readily studied. The mean orientation of the walls was parallel to the field direction and as such was reminiscent of an easy axis reversal of a single layer. The process differed, as has been observed elsewhere [55], in the irregularity and comparatively low mobility of the walls. This led to chain like structures forming during reversal as seen in Fig 3.18f,e/. This was indicative of modest local pinning. Based on observation of the fields at which reversal occurred, the offset field is $\simeq -3.5 \text{ Oe}$.

Sample 4

The layer structure of sample 4, as introduced in section 3.4, was:

Substrate/Ta 47/NiFe 64/Co 7/Cu 31/Co 60/Ru 7/Co 48/IrMn 107/Ta 32

with all thicknesses in \AA . The thickness of the second Co layer (48 \AA) in the AAF of a similar thickness to the first layer (60 \AA). The reversal process was

recorded on the CCD as the externally applied field was swept through the +30 to -30 Oe cycle described in the introduction to this section. The Fresnel images of the reversal process as are shown in Fig 3.19. In this specimen, the field applied was perpendicular to the ripple direction and reversal was observed to take place at fields of $\simeq -11$ Oe and $\simeq -3$ Oe. This was indicative of an offset field of $\simeq -7$ Oe and was somewhat greater than was observed for sample 1. It should also be noted that no 360° loops were observed in this specimen and also that time dependent effects were significant, Fig 3.19c-d. In both directions, as the magnitude of the applied field approached that of the reversal fields, a modest increase in magnitude of ripple was observed. Reversal, however, differed along the outward and return paths. The outward reversal, Fig 3.19a-d, primarily occurred through walls with a mean orientation parallel to the applied field direction. This was similar to the easy axis reversal mechanism of a single magnetic layer. The walls are also relatively low mobility, indicative of local pinning. Both the mean wall orientation being parallel to the applied field direction and low mobility were observed previously in the reversal mechanism of sample 1. Fig 3.19e-h shows the return path. In the images taken, the domain wall does not appear to be parallel to the applied field direction. This has been observed previously by King [56, 57, 58].

A number of points require to be noted. Firstly, variation in the reversal mechanism could be realised by modest changes of the applied field direction with respect to the preferred direction of magnetisation within the specimen. Thus, offsetting the applied field by $+5^\circ$ with respect to the preferred direction of magnetisation, led to a reversal that involved a combination of rotation of magnetisation and wall processes, Fig 3.20. Inevitably, the orientation of the walls that effected the reversal changed. On the outward reversal, the domain walls remained broadly parallel to the applied field direction. However for the return reversal the average wall direction was approaching perpendicular to that of the outward reversal wall direction. Secondly, changes to the reversal

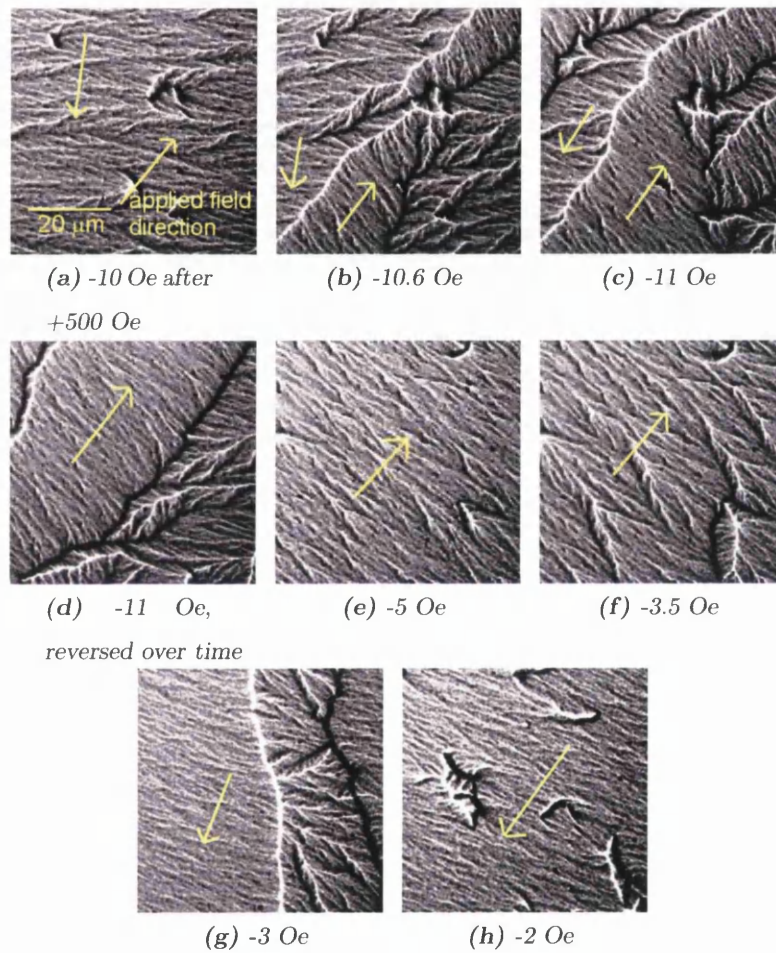


Figure 3.19: Reversal mechanisms of SV4, $X = 48 \text{ \AA}$. (a-d) Outward reversal, (e-i) Return reversal.

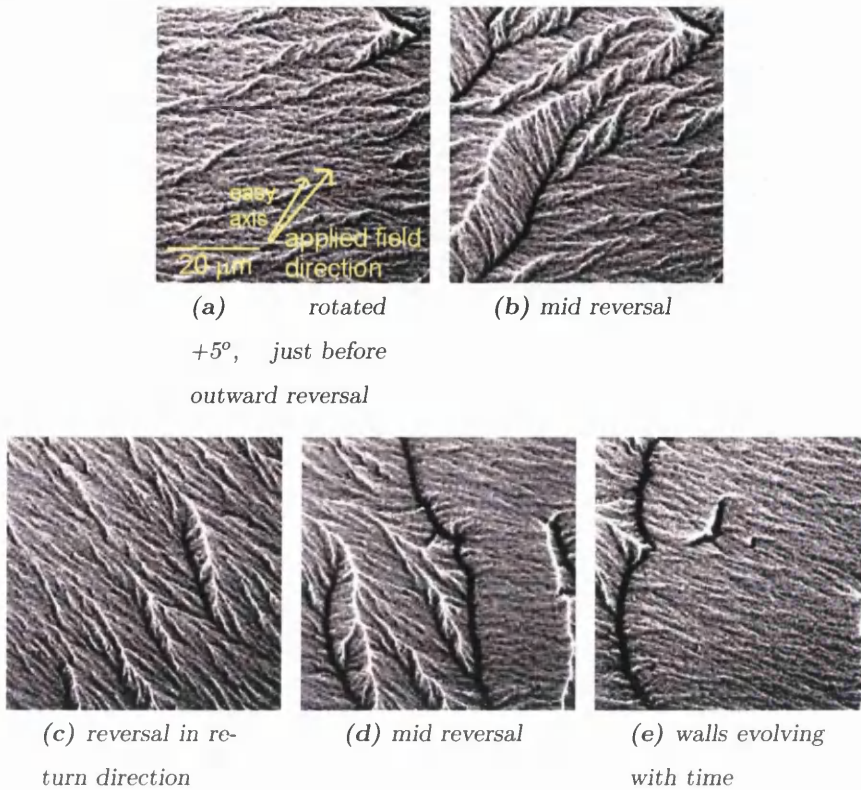


Figure 3.20: Reversal mechanism of SV4 with specimen rotated $+5^\circ$ from applied field direction.

mechanism could be realised by changing the magnetic field history, i.e. by subjecting the sample to different field processes prior to observing a particular reversal.

As the external applied field direction is applied between $+10^\circ$ and $+15^\circ$ to the preferred direction of magnetisation of the specimen, the walls arising during outward and return reversals become perpendicular to one other and are at 45° to the ripple direction. At an applied field direction $\sim +20^\circ$ from the easy axis the walls facilitating the reversal become parallel to each other and the applied field direction once again. An angle of say, $+35^\circ$ with respect to the easy axis led to rotation being the principal method for reversal whereas

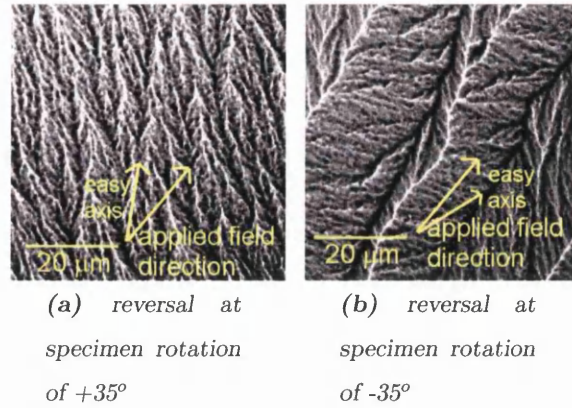


Figure 3.21: Reversal mechanism of SV4 with specimen rotated $\pm 35^\circ$ from applied field direction

an applied field at -35° degrees between the applied field and easy axis led to reversal being effected by domain wall processes, Fig 3.21. This break in symmetry between reversals at positive and negative rotation of the easy axis with respect to the applied field direction is surprising. It is not known why the break in symmetry occurred.

Sample 5

Sample 5 had a layer structure of:

Substrate/Ta 47/NiFe 64/Co 7/Cu 31/Co 60/Ru 7/Co 60/IrMn 107/Ta 32

with all thicknesses in Å. The second Co layer in the AAF was of the same thickness as the first layer. Fresnel images of the reversal process were taken as before with the CCD. Figure 3.22 shows the reversal process for both the outward and return paths. As with sample 4, no persistent 360° loops were observed. The externally applied field was parallel to the preferred direction of magnetisation of the specimen and reversal occurred at fields of $\simeq -11$ Oe and $\simeq -0$ Oe. This implied an offset field of ~ -5.5 Oe, more comparable to that of sample 4 than sample 1. It was also observed that the reversal in one

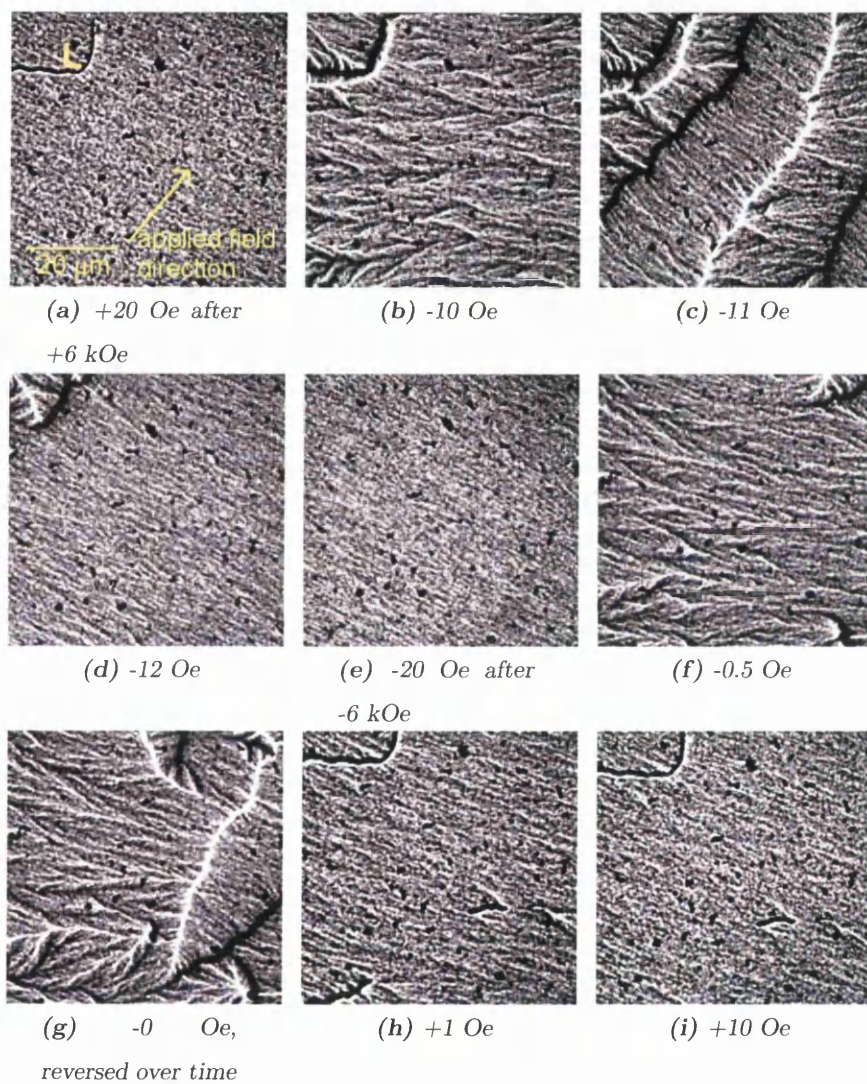


Figure 3.22: Sample 5, $X = 60 \text{ \AA}$. a-d reversal in outward field direction, e-i reversal along return path.

direction was similar to that in the other. Figs 3.22a-d, showed the reversal on the outward path; in this case there was an increase in the magnitude of the ripple, some domain growth from the persistent loops (marked L in Fig 3.22a) followed by domain walls parallel to the applied field direction effecting reversal. Domain walls present within the sample tended to be irregular which was indicative of local pinning. Figures 3.22e-i, show the return path. Here, free layer reversal occurred by a similar method to the outward path, with an increase in the magnitude of the ripple and walls parallel to the applied field reversing the direction of magnetisation.

It can be observed that the reversal processes seen here related more closely to those of sample 4 than sample 1. Due to the similarities in the AAF layer structure with the thickness of the second Co layer comparable to that of the first, this was expected.

Sample 7

The layer structure of specimen 7 was:

Substrate/Ta 47/NiFe 64/Co 7/Cu 31/Co 60/Ru 7/Co 84/IrMn 107/Ta 32

with all thicknesses in Å. In this specimen, the thickness of the second Co layer in the AAF exceeded that of the first.

Quite different magnetic structures were observed compared to those from the previous samples. The first observation is that attainment of an apparently saturated state was hard to achieve, even at fields of 250 Oe. Fig 3.23a-d illustrates this for the sample in various orientations. On removing the field, Fig 3.23e, the complexity of the domain structure increased further making it extremely difficult to identify any well-defined reference direction. The difficulty in identifying a reference direction and achieving a saturated state made it impossible to study the reversal mechanisms of this specimen.

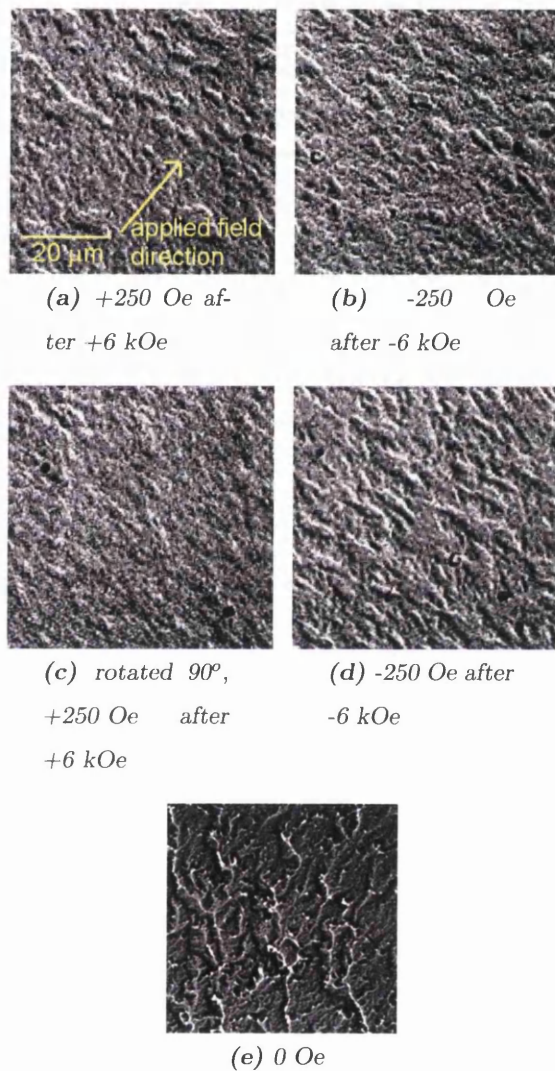


Figure 3.23: Sample 7, $X = 84 \text{ \AA}$. Illustrating difficulties in alignment of specimen with applied field direction

Sample 10

The layer structure of specimen 10 was:

Substrate/Ta 47/NiFe 64/Co 7/Cu 31/Co 60/Ru 7/Co 114/IrMn 117/Ta 32
with all thicknesses in Å. In this specimen, the thickness of the second Co layer in the AAF was almost double that of the first.

The outward reversal is shown in Fig 3.24a-f. It should be noted that 360° loops are present, even after an applied field of +6000 Oe. Chain like structures form and grow as the applied field is increased in the negative direction effecting the reversal. Fewer 360° loops remain following the reversal of the bulk of the material. The majority of the remaining loops were eliminated by a field of -100 Oe and all were removed by the application of a large field. The reversal was not abrupt and occurred predominantly over a field range of ~ -10 Oe to ~ -20 Oe.

Fig 3.24g-l shows the return reversal. The 360° walls observed in the outward reversal had been eliminated and the magnitude of the ripple was greater. A modest increase in the magnitude of the ripple was observed before chain like structures reversed the magnetisation. A number of 360° loops were present following the reversal. These loops were difficult to remove and persisted beyond an applied field of +100 Oe. After the application and removal of a large field, the loops were still present. As with the outward reversal, the return reversal occurred over a field range, ~ -2 Oe to $\sim +6$ Oe. This gives an offset in the hysteresis loop of $\simeq -7$ Oe.

It should be noted that the direction of the domains walls were at an angle of $\sim -30^\circ$ to the applied field direction in the outward reversal but were approximately $+45^\circ$ from the applied field direction in the return reversal. This change in wall orientation on outward and return reversals had been observed previously in specimen 4 and has a possible explanation if the two layers of the AAF were not exactly antiparallel. Also, chain like structures and 360° loops

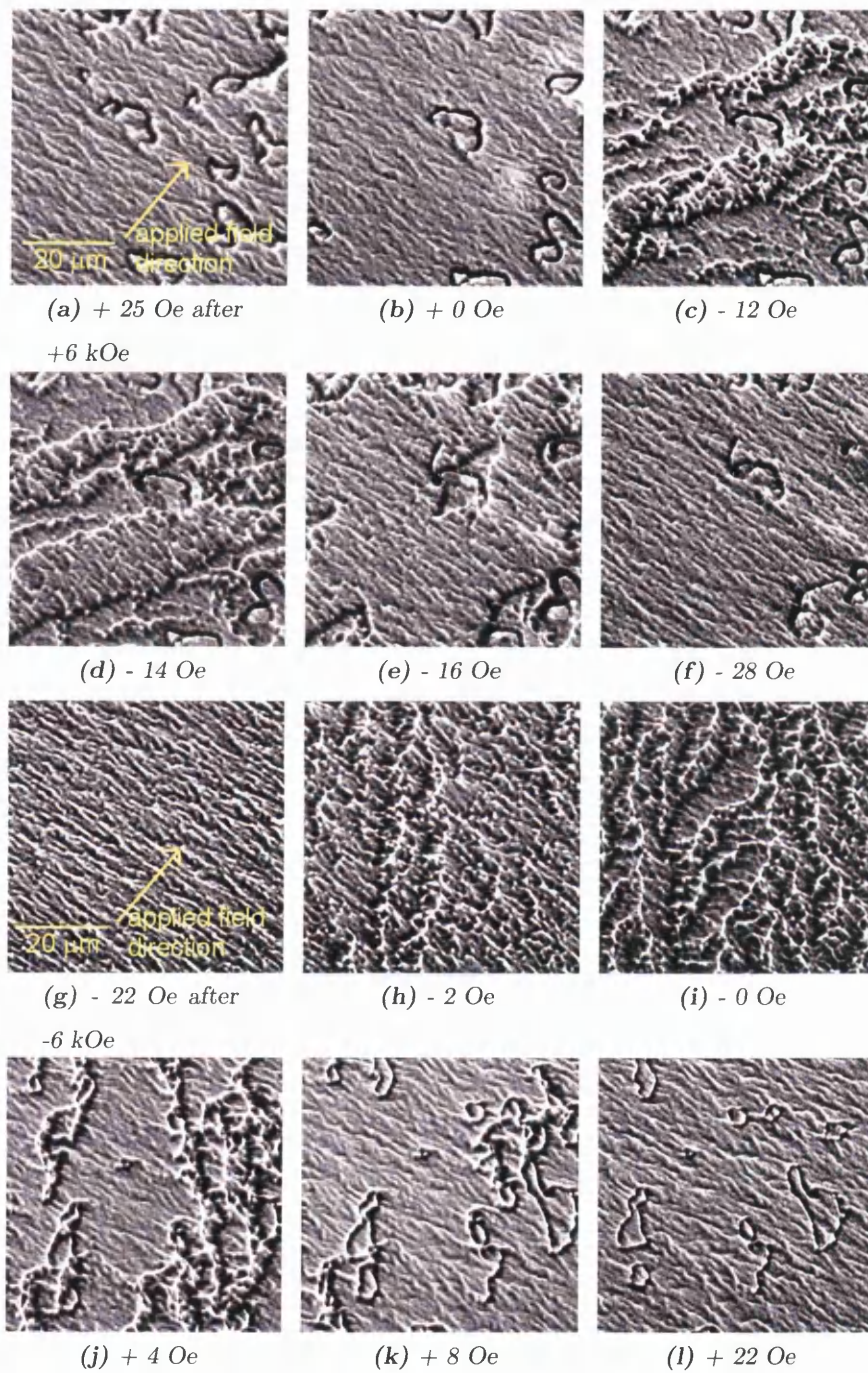


Figure 3.24: Sample 10, $X = 114 \text{ \AA}$. Outward and return reversals.

were observed in specimen 1. The chain like structures are well understood. However, the 360° loops observed in both specimens differ. In specimen 1, the loops remained in the same position from reversal cycle to reversal cycle and proved very difficult to remove in either a positive or negative applied field. The loops in specimen 10 were considerably larger in size and were removed after the application of a reasonable negative field. The behaviour of this specimen is not simple, however, it is consistent with an unbalanced AAF in the spin valve structure unlike specimen 7.

3.7 Magnetoresistance Measurements

Magnetoresistance measurements of each specimen were obtained using the standard 4 probe CIP arrangement introduced in section 1.5.1. These results were collected by Dr Chris Marrows at the University of Leeds. Actual GMR curves were not available for study. However, a plot of the maximum GMR amplitude as a function of the second Co layer thickness for eight of the specimens is shown in Fig 3.25. From this, it can be observed that in general the GMR decreases as the second Co layer increases in thickness. The principal exception to this is specimen 7 which is discussed separately. The decrease in GMR can be attributed to the second Co layer shunting the current; as the thickness of the second Co layer increases, the current through this layer increases reducing the current flowing through regions in which spin dependent effects occur.

Specimen 7 proved difficult to study magnetically with a highly complex domain structure, no observable preferred direction of magnetisation and with domains that proved difficult to remove. This suggests it would support a very low MR. Moreover, samples of this structure had been shown in previous work to display only small effects [43]. The inability to realise a uniformly magnetised free layer whose orientation reverses over a modest field range is

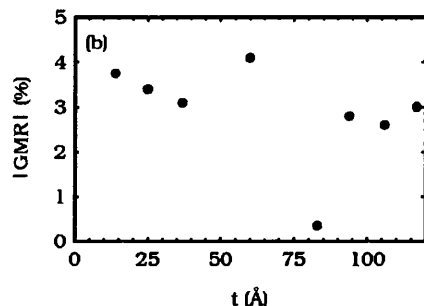


Figure 3.25: Maximum GMR amplitude as a function of second Co layer thickness

consistent with the small GMR observed.

As shown in specimen 4, the reversal mechanism varies as the applied field direction is moved away from parallel to the preferred magnetisation direction of the specimen. Although no data is available for this specimen, plots of the variation of the GMR with applied field angle for other samples are shown in Fig 3.26. These show that the GMR varies depending on the applied field direction in all specimens. This is in agreement with the variation in the reversal mechanisms observed in specimen 4. The applied field direction with respect to the easy axis affects the reversal mechanisms. The change in the relative orientation of the magnetic layers away from parallel and antiparallel affects the change in the measured resistance and hence the MR. It can also be noted that the one specimen where the GMR does not vary significantly as the applied field direction is varied is specimen 7.

3.8 Discussion and Conclusions

During growth, as the first Co layer of the AAF was deposited, the expectation was that the magnetisation would align parallel to the applied field of 200 Oe. Then, as the second Co layer of the AAF was deposited, the magnetisation of the second Co layer would compete with the first layer to lie parallel to the

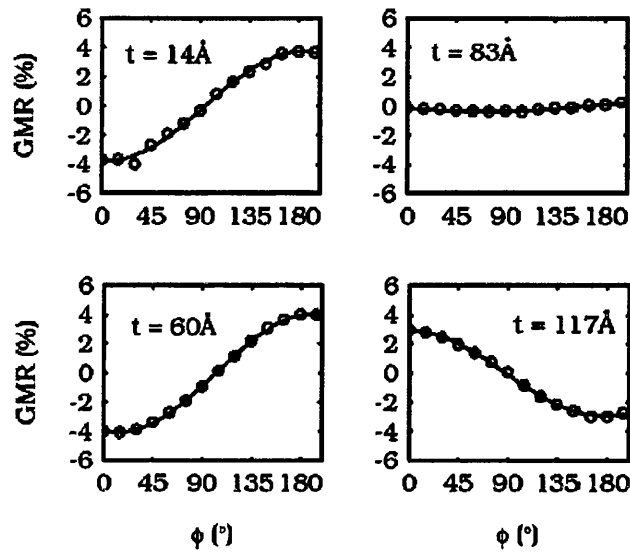


Figure 3.26: Variation of GMR amplitude as a function of applied field direction with respect to preferred direction of magnetisation

applied field direction. It was thought that as the thicknesses of the two Co layers became comparable, the magnetisation of the two layers would rotate to be perpendicular to that of the applied field to leave a balanced system. This would subsequently be pinned in by the growth of the AFM layer. Beyond this, it was expected that once the thickness of the second Co layer was significantly greater than that of the first Co layer in the AAF, the second Co layer would rotate to lie parallel with the applied field, and thus cause the first Co layer to reverse through the AAF coupling. Moreover it was thought that the system would behave like a conventional SV in the situation where there were considerable differences in the two Co layer thicknesses of the AAF. This expectation was observed.

Major disagreement was found when attention was paid to where changes in behaviour were observed within the sample series. Thus samples 1, 4 and 5 showed rather similar behaviour despite the fact that the thicknesses of the two

Co layers in sample 1 differed markedly whilst in sample 5 they were notionally identical. Moreover anomalous behaviour, with virtually no GMR present, was not observed until sample 7 where the second Co layer should have been much thicker than the first layer. That GMR did reappear, but with the anticipated phase change, for samples with much larger thicknesses from the second Co layer is apparent from Fig 3.26.

When taken together, the above throws strongly into question whether certain layer thicknesses were close to their notional values. For that reason, a further structural study was undertaken to see what could be learned of true layer thicknesses.

3.8.1 Cross Section Study

An investigation was carried out to examine the true layer thicknesses of some of the samples. The expected layer structure with all thicknesses in Å of the specimens was

Si/SiN/Ta 47/NiFe 64/Co 7/Cu 31/Co 60/Ru 7/Co X/IrMn 107/Ta 32

with $X = 14$ or 60 for samples 1 and 5 respectively.

To facilitate this structural characterisation, a TEM specimen was prepared by Mr Brian Miller of the Solid State Physics group using Cross Section Encapsulation. This technique is outlined briefly below. High resolution TEM and Scanning TEM images of the cross sections were taken and analysed by Dr Sam McFazdean, also of the SSP group, on the Tecnai [59] microscope. The results of these measurements are shown below.

Cross Section Encapsulation

The TEM specimen sought consists of two thin sections of the sample material, with the faces of interest adjacent to one another, that has been thinned until electron transparent.

A 2 mm diameter molybdenum rod with a slot, $\sim 380 \mu\text{m} \times 15 \text{ mm}$, cut in a section of the rod was prepared. Two strips of the specimen to be investigated were ground until the thickness of each was half the width of the slot. The specimens were joined (faces of interest facing one another) using epoxy resin. They were then inserted into the slot of the Mo rod and secured using epoxy resin. The rod and specimen were mounted into a brass rod and cured at $130 \text{ }^\circ\text{C}$ for 1 hour.

A diamond saw was used to cut slices from the cured encapsulation. 3 to 6 discs of thickness 500 to $800 \mu\text{m}$ were obtained from each encapsulation. These discs were thinned to $\sim 120 \mu\text{m}$ using silicon carbide paper of varying grades and polished using $3 \mu\text{m}$ diamond paste on a rotating felt polishing pad. Each side of the disc was thinned in turn to achieve the desired thickness.

The encapsulated specimen was then dimpled until the centre of the specimen was $\sim 10 \mu\text{m}$ in thickness. For a silicon based specimen, this can be recognised when the thinned region transmits light of a red/orange colour. From this point, the specimen was thinned further to electron transparency by using ion milling. Ion milling progressively removes sample material until an area of material becomes electron transparent. It creates an elliptical hole in the middle of the cross section (major axis along the glue line), the electron transparent region surrounding the edges of this hole.

TEM investigation of the cross sectioned specimen

The cross sectioned encapsulation of the AAF biased SV specimens were investigated in the Tecnai [59] TEM microscope. Fig 3.27 shows a bright field TEM image of the specimen 1. The total width of the cross section (the specimen thickness) was measured to be 456 \AA . The total width of specimen 5 was found to be 471 \AA . These are not in very good agreement with the expected thicknesses of 369 \AA and 415 \AA .

Fig 3.28 shows STEM annular dark field images of specimens 1 and 5. In

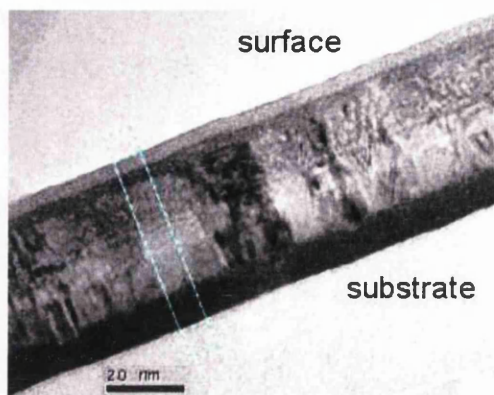


Figure 3.27: HRTEM image of specimen 1

this imaging mode contrast relates strongly to the mean atomic number of the region under the probe. Regions with high Z appear brighter as they scatter more strongly. The bright band at the right hand of the spin valve is the Ta seed layer. To the left of the seed layer is the free layer, the spacer and the first Co layer of the AAF. These are indistinguishable due to the similarity in their atomic weights. To the left of that is the bright Ru band. The second Co layer of the AAF tri-layer can be seen between the Ru and the IrMn biasing layer. The tri-layer is easier to observe in specimen 5 as the second Co layer was expected to be $\sim 60 \text{ \AA}$ corresponding to a significant separation between the Ru and IrMn layers. In the unbalanced AAF, the second Co layer was expected to be $\sim 14 \text{ \AA}$ and as such, was more difficult to observe. At the left hand side of the spin valve is the Ta cap layer. It appears much less bright than the Ta seed layer as it is thinner than the seed due to the specimen being wedge shaped. There are thus fewer atoms for scattering, hence there is a reduction in the brightness.

To confirm correct identification of the layers, energy dispersive X-ray (EDX) spectra were recorded for various positions within the cross section. Fig 3.29 shows the results for specimen 5. In the figure, the left hand images are annular dark field STEM images, the red square marks the area used for

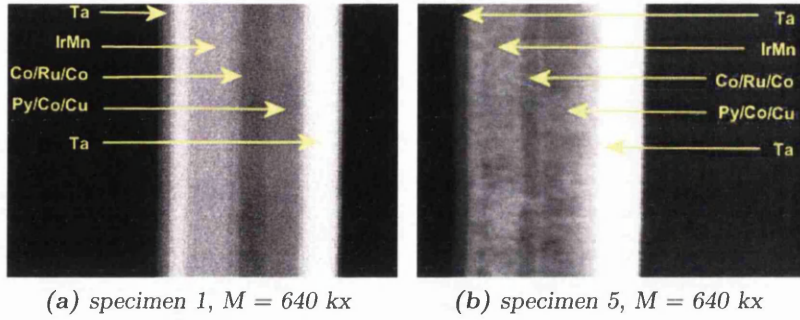


Figure 3.28: Annular dark field STEM images of specimens 1 and 5

automatic drift correction and the red line represents the line scan. An EDX spectrum of the marked point (cross) on the line scan is shown next to the image. Five different points from the line scan are shown in Fig 3.29: in the Ta seed layer; in the NiFe free layer; close to Cu spacer; around the Co/Ru boundary; and in the IrMn biasing layer. Ta is observed in all spectra presumably due to the redeposition of Ta atoms during the fabrication of the cross section.

Overall the spectra are at least qualitatively consistent with expectation. The resolution however, is insufficient for an accurate measure of layer thicknesses, for this we return to what can be extracted from the annular dark field images. Table 3.2 shows the layer thicknesses of specimen 5 obtained from the ADF images.

Layer	Subs	Ta	NiFe / Co / Cu / Co	Ru	Co	IrMn	Ta
Expected		47	162	7	60	107	32
Measured		108	152		39	96	43

Table 3.2: Expected and measured layer thicknesses of specimen 5 in Å.

The most obvious feature of the table, apart from the wide discrepancy in expected and observed Ta layer thicknesses which should not affect the

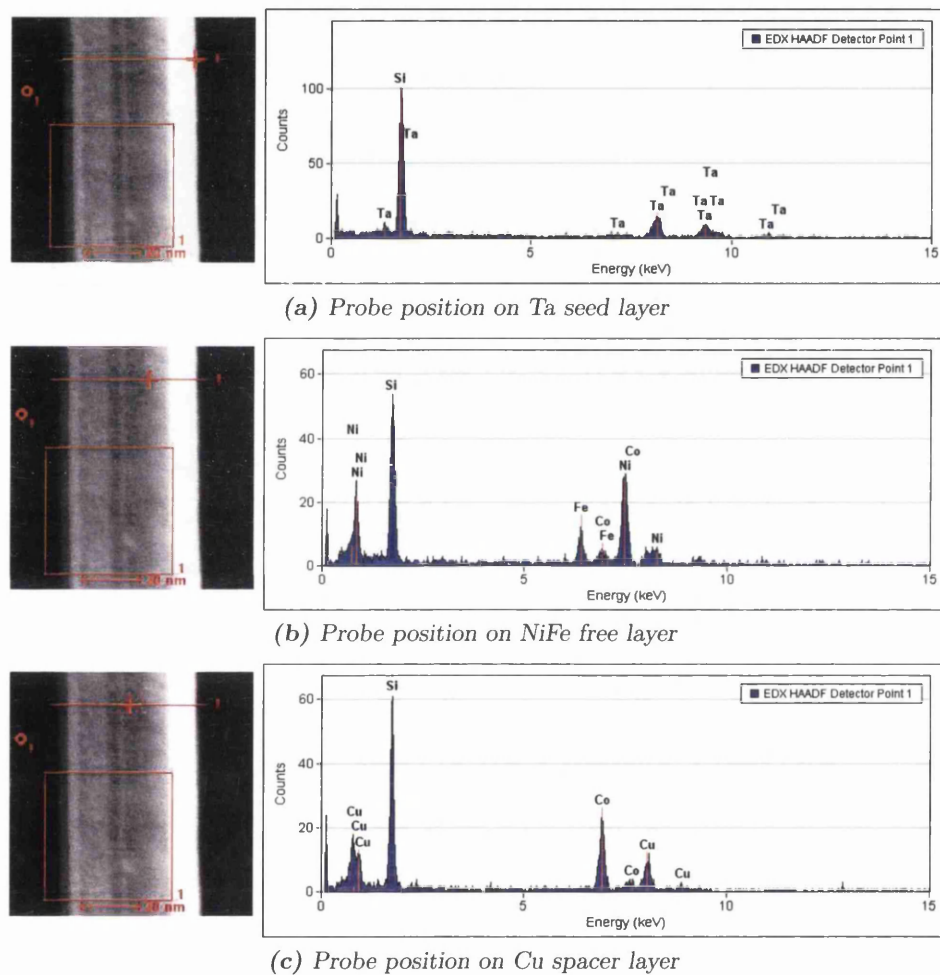
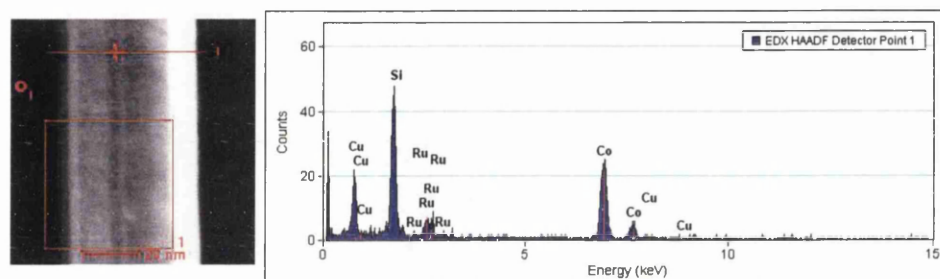
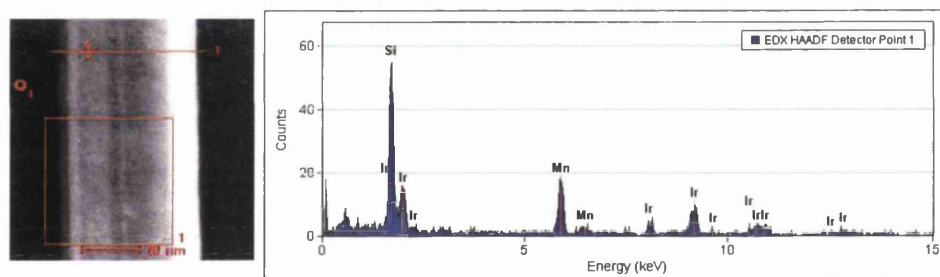


Figure 3.29: EDX spectra of five points across the spin valve stack



(d) Probe position on Co Ru Co biased AAF trilayer



(e) Probe position on IrMn biasing layer

Figure 3.29: EDX spectra of five points across the spin valve stack (continued)

magnetic properties, is the discrepancy between the expected and observed thicknesses of the second Co layer. Whereas the confirmed thickness of the NiFe/Co/Cu/Co layer is within 6 % of expectation, the thickness of the second Co layer is only 2/3 of the expected value. In sample 1, the very detection of the second Co layer is difficult, a fact that would be easier to understand if, once again, the true thickness was significantly smaller than expectation. Consultation with the film growers provided no obvious reason how such discrepancies could arise, but their existence allows a re-evaluation of the earlier results to be made. This is given in the Conclusions.

3.8.2 Conclusions

The discovery that the thickness of the second Co layer in the AAF was less than expected aids explanation of some of the magnetisation studies presented earlier in this chapter. It is assumed from the results obtained in the cross sectional study that the second Co layer of all specimens is thinner than expected.

Specimen 1, where the second Co layer of the AAF was assumed to be 14 Å, exhibited 360° walls which were present throughout the reversal cycle. The reduced thickness could have led to a non uniform layer, with pin holes between the Ru and IrMn. These pin holes could provide sites that stabilised the 360° walls observed experimentally.

Specimens 4 and 5, where the thickness of the second Co layer was thought to be approximately that of the first Co layer in the AAF showed behaviour more similar to CSV's. This is consistent with the observation that the second Co layer was thinner than the first Co layer for both these samples and so we have an explanation of the behaviour being different from that expected.

Following on from this, if the thickness of the second Co layer was consistently $\simeq 2/3$ of the expected value, for specimen 7 it would be between

55 Å and 60 Å. Thus specimen 7 is likely to be close to the balanced AAF composition consistent with the highly complex domain structure, no observable preferred direction of magnetisation and virtually zero GMR.

For specimen 10, the thickness of the second Co layer was truly significantly greater than the first with simpler GMR behaviour again being observed.

Chapter 4

Transmission Electron Microscopy of Patterned Spin Valves

4.1 Introduction

Spin valves biased with artificial anti-ferromagnets are modified SVs designed to give a high level of sensitivity and an improved range of operating temperatures. Thin films of these AAF structures were investigated in Chapter 3 to gain an insight into the bulk properties. However, for use in applications such as magnetic memory and read/write heads, it is more desirable to investigate magnetic elements.

The reversal properties of magnetic elements have been investigated for many years; both single layer elements [60, 61, 62] and multilayer elements [63, 64, 65] have been studied. With magnetic elements, the physical dimensions and shape can affect the reversal mechanisms; this is shown in [66, 67]. This chapter discusses the characterisation of AAF biased SV elements with the same layer structure as the bulk material investigated in Chapter 3.

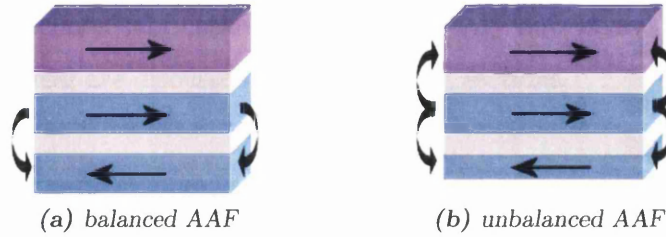


Figure 4.1: Schematics of stray field coupling in balanced and unbalanced AAF spin valves

As shown by Yi et al [67], the size and end shape of an element can affect the reversal process. In the case of multilayer stacks, the layer structure can also alter the reversal mechanism. Some of the interlayer coupling mechanisms for thin films spin valves and artificial anti-ferromagnetically biased spin valves have been introduced previously (sections 1.5.1, 3.1 and 3.4). However, for elements, these coupling mechanisms are modified due to the finite size of the element. At the edges of an element, stray field coupling between the magnetic layers exists. In conventional SVs, this extra coupling between the pinned and free layers can contribute to a larger offset in the hysteresis loop. This is rarely desirable for use in applications.

For AAF biased SVs, the edge field coupling can be modified by varying the relative thickness of the two magnetic layers of the AAF. If both layers of the AAF were equal, Fig 4.1a, the free layer should experience essentially no stray field coupling though other interlayer coupling is still present. For an unbalanced AAF, Fig 4.1b, there would be a net stray field from the two layers of the AAF and the system should act more like a conventional SV. From this, it would be possible to tune the layer thicknesses so that the stray field coupling offset is equal and opposite to that arising from interlayer coupling. This would leave the element free to reverse round zero field.

This chapter investigates elements of two AAF biased spin valves with a range of dimensions, shapes and orientations with respect to the growth field

direction. Specimen fabrication, a structural study and investigations in the magnetic reversal are discussed in the following sections.

4.2 Specimen Fabrication

As discussed in the introduction, the reversal mechanisms of AAF biased SV elements were investigated in the CM20. Two different layer structures corresponding to specimens 1 and 5 discussed in Chapter 3 were studied. These were chosen to enable the study of an unbalanced and a balanced AAF system. However, from the results of the cross sectional study presented in Chapter 3, it was found that the second Co layer of both specimens was thinner than anticipated. This indicated that both specimens had an unbalanced AAF and that the second Co layer in specimen 1 may have been non uniform.

The elements chosen for investigation varied in size and shape. Three different end shapes were investigated: rectangular ends; rounded ends; and elliptical ends. For each shape, four different sizes were fabricated: $4 \times 2 \mu\text{m}^2$; $1.5 \times 0.75 \mu\text{m}^2$; $0.75 \times 0.375 \mu\text{m}^2$; and $0.4 \times 0.2 \mu\text{m}^2$. Also, for each shape and size, a range of orientations with respect to the growth field direction was investigated. These were parallel to the growth field, 22.5° to the growth field, 45° to the growth field, 67.5° to the growth field and perpendicular to the growth field direction. Fig 4.2 shows a SEM image of the fabricated pattern. The large area in the top right hand corner was an area of continuous thin film to enable direct comparison between the elements and bulk material.

The pattern was transferred onto TEM windows by e-beam lithography (section 2.2.1). The TEM windows had previously been fabricated using the standard technique, broken into groups of four and coated in a bi-layer of resist. The desired layer structure was sputtered (section 2.4) onto patterned windows at the University of Leeds. Lift-off completed the fabrication process. Due to the nature of the specimen, charging while in the TEM was a significant

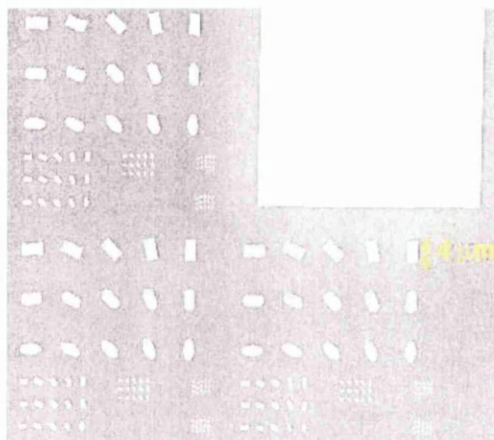


Figure 4.2: SEM image of elements for investigation in the TEM

problem. This was overcome by coating the specimen with a thin carbon layer to improve conductivity. The carbon coating procedure was undertaken in an evaporator similar to the evaporator described in section 2.4. The difference was that, instead of heating a crucible of the desired metal, a high current was passed through carbon fibres leading to thermal evaporation and coating of the specimen. The group of four TEM windows were then separated into single windows for investigation in the Philips CM20.

4.3 Magnetic Studies of Specimen 5

Specimen 5 was originally chosen for further investigation as it was thought that this specimen possessed a balanced AAF layer structure. The cross section investigation presented in Chapter 3 showed that the AAF was not balanced and therefore the behaviour should be more like a conventional SV. The experimentally measured layer structure in Å of specimen 5 was

Substrate/Ta 108/NiFe Co Cu Co 152/Ru /Co 39 /IrMn 96/Ta 43.

In the studies described here, the easy axis reversal mechanisms of the free layer were investigated. The elements were oriented in the microscope such that

the applied field was parallel to the growth field, i.e. the preferred direction of magnetisation in the free layer of the continuous film. Initially the as grown state was investigated.

Following this, in a typical experiment a high field was applied parallel to the growth field direction to align the free layer with the applied field. The strength of the applied field was subsequently reduced to enable observation of the reversal process. The field in the plane of the specimen was then swept from this reduced field through zero field to the same field applied in the opposite direction. The reversal process was recorded using DPC imaging.

This high field and reversal sweep was repeated for the opposite field direction and DPC images of the reversal were again recorded. The field range differs between elements and in each case was selected to ensure substantial reversal of the free layer whilst having negligible effect on the AAF coupling. A considerably larger field (> 6000 Oe) is required to alter the AAF coupling. Negative numbers in the applied field denote an applied field in the same direction as the preferred orientation of the free layer.

4.3.1 DPC images of the as grown state

DPC images of the as grown state were taken. The direction of induction to which images are sensitive is shown above the first image.

Fig 4.3 shows images of the $4 \times 2 \mu\text{m}^2$ rectangular elements in the as grown state. It can be observed that the element with long axis parallel to the growth field direction was in a C state. This domain configuration is only possible when the growth field is along the easy axis confirming the direction of the applied field during growth. Looking at the elements at 22.5° , 45° and 67.5° to the growth field, it can be observed that the as grown state was an S state. This would be expected as the applied growth field would have tended to align the free layer magnetisation along the direction of applied field. After

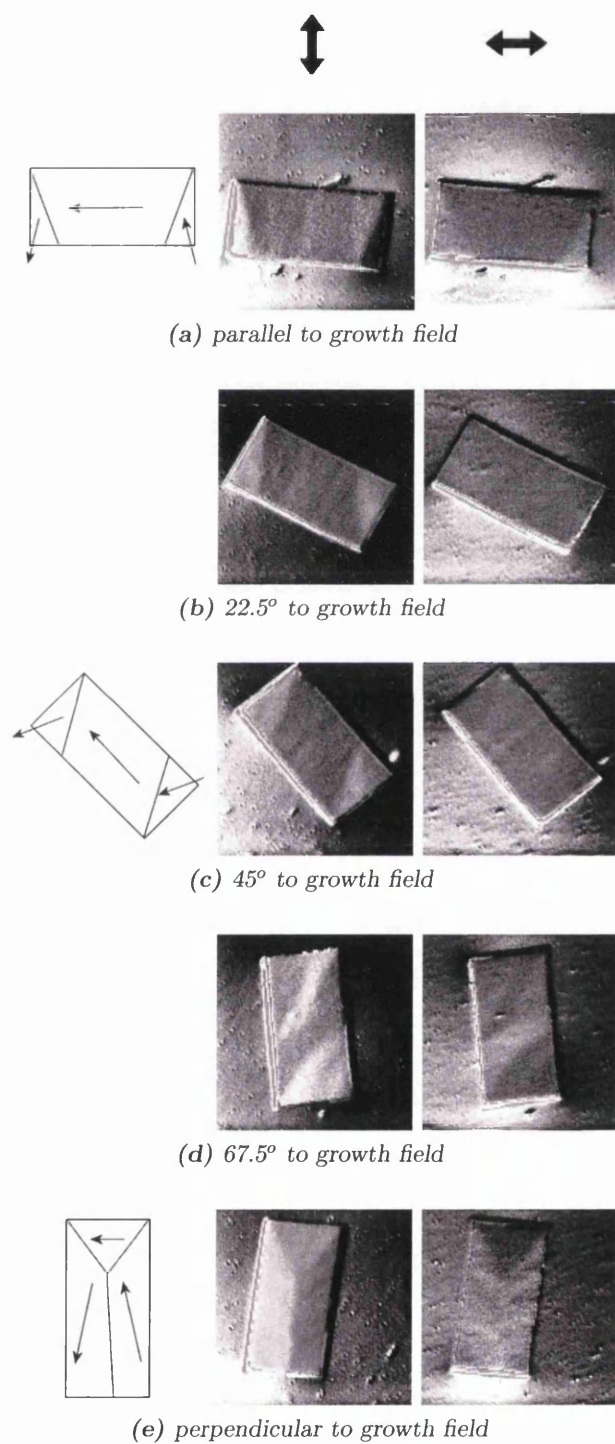


Figure 4.3: Images of $4 \times 2 \mu\text{m}^2$ rectangular elements in the as grown state 97

removal of the growth field, this element would relax into a lower energy state, the S state. The element perpendicular to the growth field was in a slightly more complex domain configuration. This was due to the growth field being applied perpendicular to the long axis from the element. This led to one end of the element being flux closed whereas the other has a 180° wall perpendicular to the end of the element. All images exhibit strong edge contrast. This could have arisen from edge flagging due to the fabrication process or due to possible interference fringes arising from a 'domain wall' between the internal and external magnetisation.

DPC images of the as grown state for the $4 \times 2 \mu\text{m}^2$ elements with rounded ends are shown in Fig 4.4. These elements exhibited more complex domain structures than the rectangular elements discussed previously. The element with major axis parallel to the growth field direction, instead of the C or S state observed in the rectangular element, possessed a complex domain structure at one end. This structure was possibly the start of a vortex. In the bulk of the element, a ripple like structure was also observed. It was also present in the elements at 22.5° and 45° to the growth field. The element at 45° to the growth field possessed a small vortex at one end of the element and again is significantly more complex than its' rectangular counterpart. The element perpendicular to the growth field direction was substantially flux closed with rotation at one end and a vortex structure at the other end of the element. Sketches of some of the domain structures can be seen adjacent to the DPC images. The increase in complexity for all elements was due to the lack of corners in these elements. Corners acted as domain nucleation and location points, without them, local effects within the element had a considerably larger effect leading to significantly more complex domain structures such as those observed here. This was also applicable for the elliptical elements discussed below.

Fig 4.5 shows the as grown states for the $4 \times 2 \mu\text{m}^2$ elliptical elements.

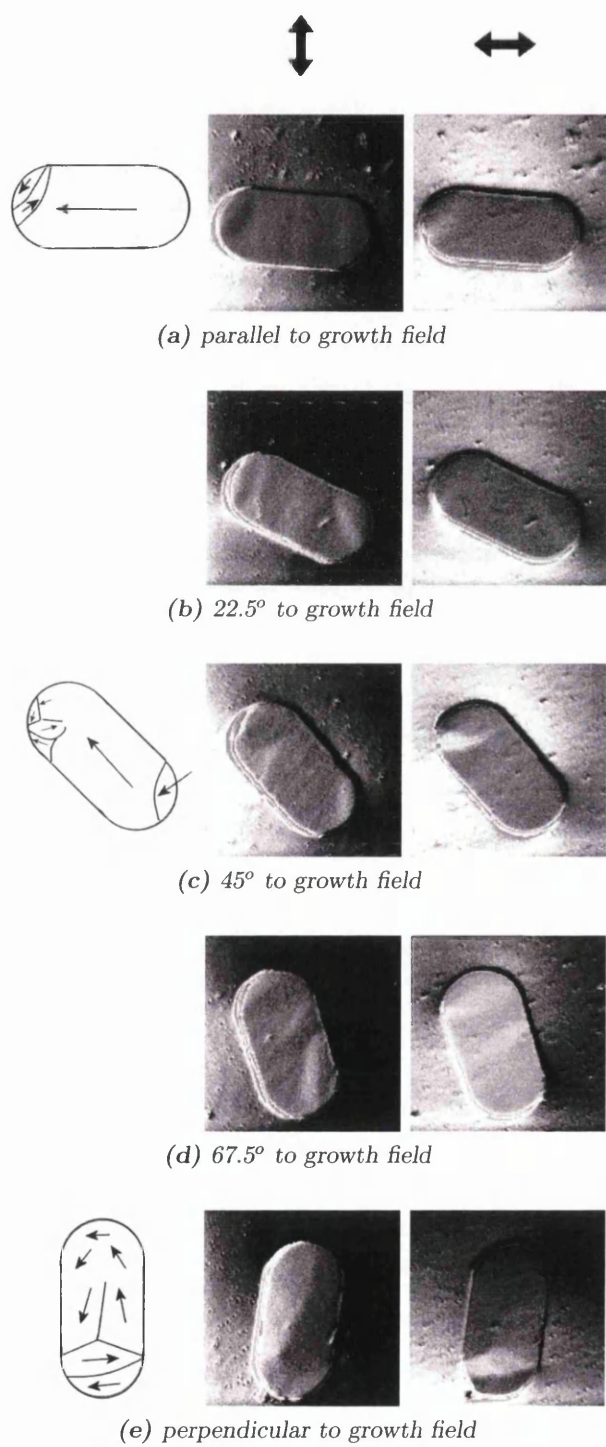


Figure 4.4: Images of $4 \times 2 \mu\text{m}^2$ elements with rounded ends in the as grown state

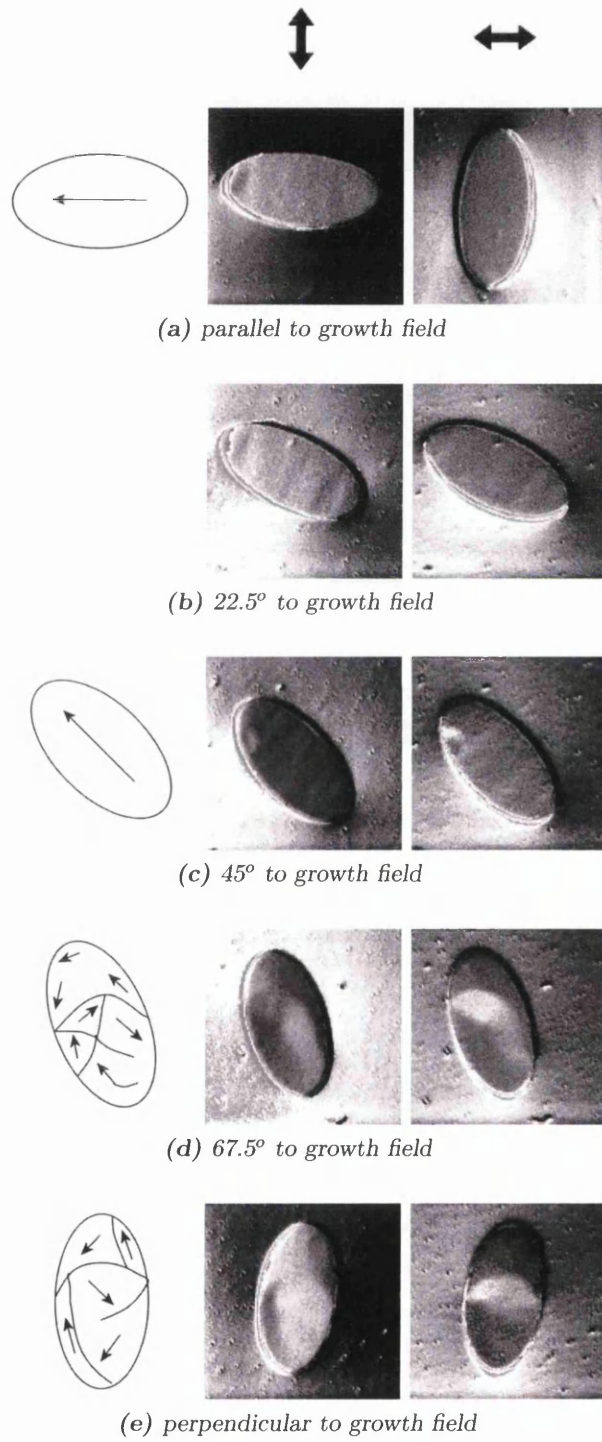


Figure 4.5: Images of $4 \times 2 \mu\text{m}^2$ elliptical elements in the as grown state 100

For the first three elements (parallel, 22.5° and 45° to the growth field) a simple single or very near single domain structure was observed. This structure was less complex than either that of the corresponding rectangular elements or the elements with rounded ends. A uniform ellipsoid possesses a uniform demagnetising field and is therefore more likely to relax into a single domain state. These ellipses were not perfect, hence some ripple was observed, but the magnetisation of the element was otherwise uniform. As before, the elements at 67.5° and perpendicular to the growth field exhibited a more complex domain structure. Both domain structures are sketched adjacent to the DPC images. The competition between the shape anisotropy and growth field was responsible for the more complex structures observed.

4.3.2 Reversal of $4 \times 2 \mu\text{m}^2$ rectangular element parallel to growth field

The reversal mechanism of the $4 \times 2 \mu\text{m}^2$ element parallel to the growth and applied field directions is shown in Fig 4.6. After the application of a large positive field to saturate the free layer in the applied field direction without affecting the AAF biased layers, the field was reduced and DPC images were recorded over the field range where reversal occurred. This was repeated for a field applied in the opposite direction. It should be noted that due to the long exposure times for obtaining a full reversal set, the contrast for the images cannot be directly compared in some cases.

On the outward reversal, it can be observed that by an applied field of $+27$ Oe, the element has formed an S state. Reversal then occurred over a wide field range ($\sim +6$ Oe to -9 Oe), with the magnetisation direction in the bulk of the element reversing before the edges. This gave a complex domain structure, sketched next to the DPC images taken at 0 Oe. There are an odd number of domains through the bulk of the element. This was due to

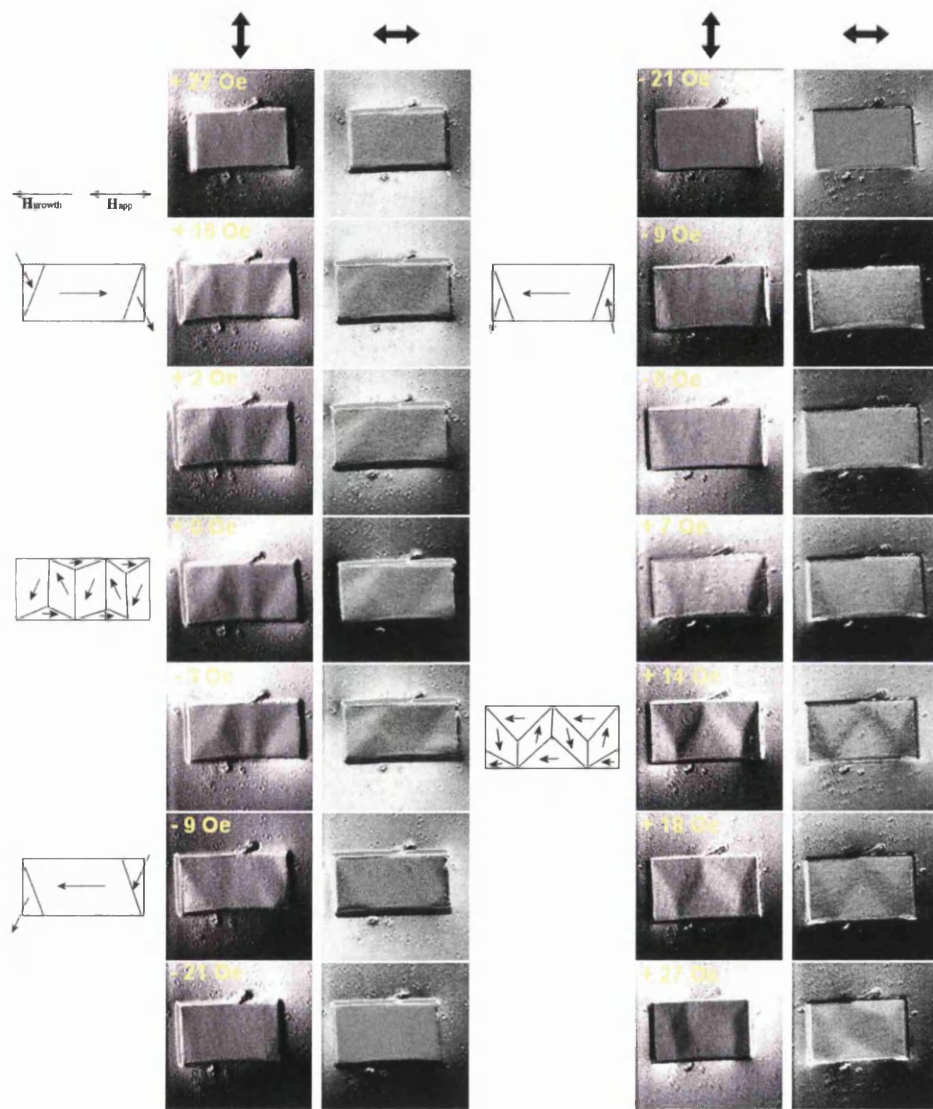


Figure 4.6: Reversal of $4 \times 2 \mu\text{m}^2$ element parallel to growth field

the initial S state where the magnetisation at both ends of the element was oriented in the same direction. By - 9 Oe, the element had reversed and was again approaching an S state.

The return reversal mechanism differed to that of the outward reversal. In this case, the element had relaxed into a C state. C and S states are very similar in energy so it is not unexpected that the element can relax into either state. Reversal occurred with the centre of the element undergoing reversal before the edges. This was consistent with the outward reversal. However, two points should be noted. Firstly, due to the initial C state, there were an even number of domains in the centre of the element whereas for the outward reversal there was an odd number. This is due to the magnetisation direction at both ends of the element being the same for an S state giving an odd number of domains and the magnetisation direction for a C state being in different directions leading to an even number of domains. The sketches adjacent to +0 Oe in the outward reversal and +14 Oe in the return reversal shown in Fig 4.6 show this diagrammatically. Secondly, the edge domains for the return reversal were considerably larger than those observed on the outward reversal. This was due to the initial magnetisation lying parallel to the preferred direction of magnetisation. For the return path, the field range over which reversal occurred over was $\sim + 7$ Oe to $>+ 27$ Oe. Taking into account the fields at which the outward and return reversal occurred, the offset in the hysteresis loop can be estimated to be $\sim + 15$ Oe. Clearly the hysteresis loop is broad without sharp transitions between $\pm M_S$.

4.3.3 Reversal of $4 \times 2 \mu\text{m}^2$ rectangular element at 45° to growth field

Fig 4.7 shows the reversal of $4 \times 2 \mu\text{m}^2$ element at 45° to growth field. Again, a large field saturated the free layer in the applied field direction, was reduced

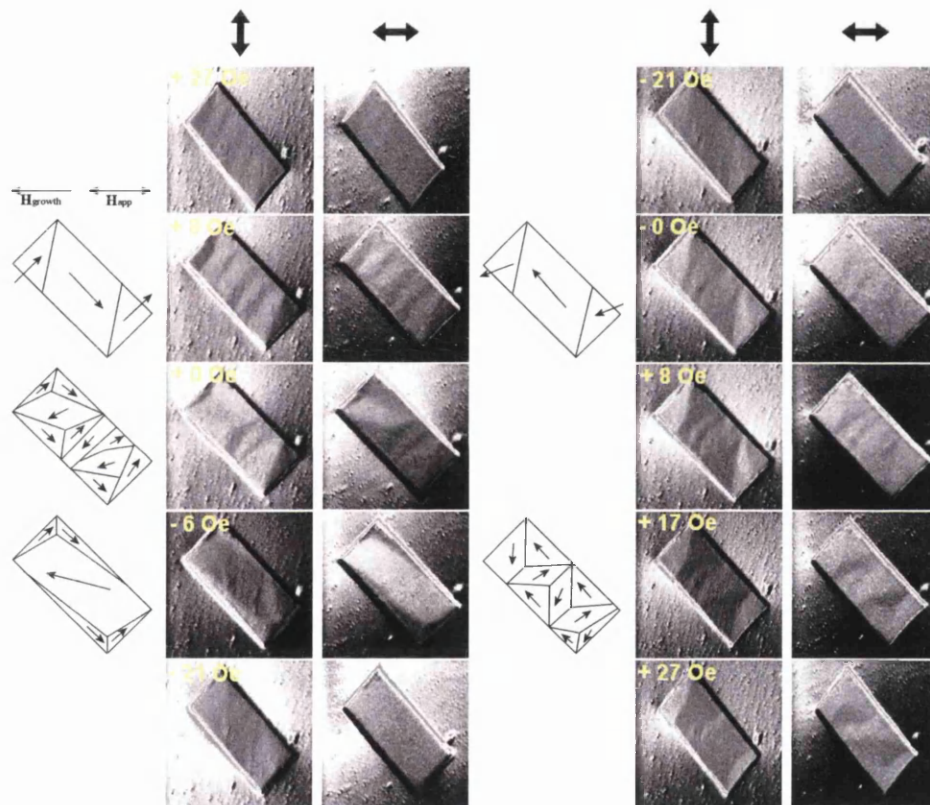


Figure 4.7: Reversal of $4 \times 2 \mu\text{m}^2$ element at 45° to growth field

and DPC images of the reversal were recorded. The field was then applied in the opposite direction to enable the return reversal to be investigated. As with the reversal of the element parallel to the applied and growth fields, an S state existed in a modest positive field. Also observable was a faint ripple effect at an applied field of + 27 Oe. This intensified at + 8 Oe. As the applied field was further reduced, reversal began to occur and was almost midway by 0 Oe. At 0 Oe, a complex domain pattern was observed with the centre of the element reversing before the edges. Adjacent to the DPC images, a sketch of the domain structure shows 7 domains in the centre of the element. This odd number was necessary due to the initial S state. As the field was increased in the negative direction to - 6 Oe, it can be seen that the reversal had almost completed with the bulk of the element reversed and only two corners possessing domains. By - 21 Oe, these domains have been removed and the element has fully reversed into an S state. It was not possible for the element to relax into a C state as the applied field was at an angle to the the element long axis.

Reversal on the return path occurred with the centre of the element reversing before the edges. As the applied field was reduced, the element relaxed into an S state. From this, a complex domain structure formed with domains at the edges being larger than those observed on the outward reversal. Reversal started at $\sim + 8$ Oe and was past midway by + 27 Oe. This gave an offset in the hysteresis loop of $\sim + 11$ Oe with both the outward and return reversal taking place over a wide field range.

The remanant magnetic states of the rectangular elements parallel and at 45° to the growth and applied field directions are shown in Fig 4.8. From this, it can be seen that the elements are in a more complex domain configuration after the application of a large positive field. This corresponds to the states observed during the reversal of both elements and also indicates that both elements have the same preferred direction of magnetisation. As both elements

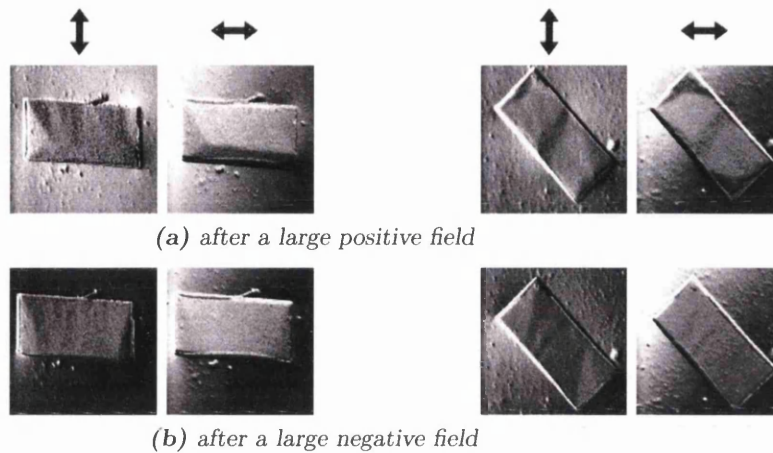


Figure 4.8: Remanant images of rectangular elements parallel to and at 45° to the growth field direction. The images at remanence were taken from a separate set of measurements to those in Fig 4.7

were grown together under the same conditions, this was expected.

It is interesting to note that the element parallel to the applied field direction was in a C state after a large negative applied field and during reversal whereas during the reversal cycle, a S state was observed during the outward reversal. The domain configuration after a large positive field was more complex but there was some indication that a S state had been present. Further investigation indicated that both the S and the C state were equally likely in this element after both negative and positive applied fields, this was expected as the S and the C state are of similar energy. However, for an element at 45° to the growth and applied field directions this was not observed. Fig 4.9 gives a diagrammatic explanation.

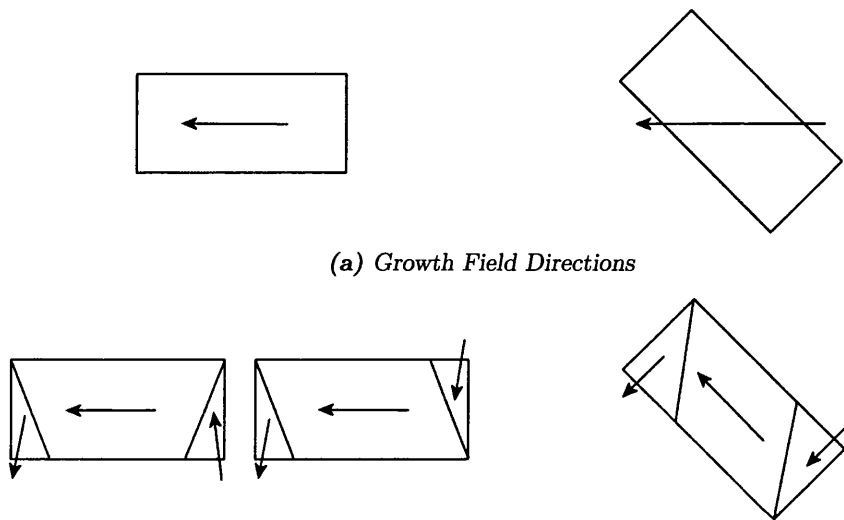


Figure 4.9: Schematic diagrams of elements parallel to and at 45° to the growth field direction. The local magnetisation prefers to lie near parallel to the edge of the element, hence C and S states are equally favourable for elements parallel to the growth field direction. For the element at 45° , the C state is not possible as for the magnetisation to lie parallel to the edge, the direction of magnetisation at one end of the element would have to be against the preferred direction of magnetisation/applied field direction which requires considerably more energy than the S state shown.

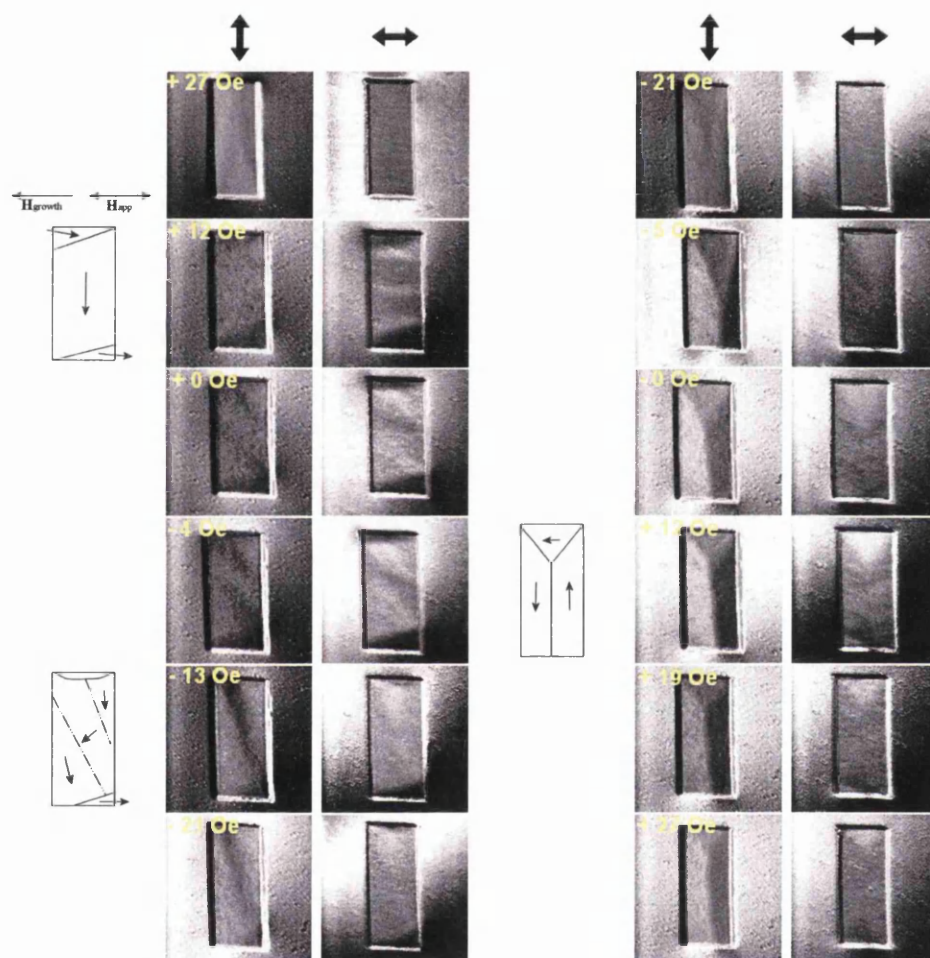


Figure 4.10: Reversal of $4 \times 2 \mu\text{m}$ rectangular element perpendicular to growth field

4.3.4 Reversal of $4 \times 2 \mu\text{m}^2$ rectangular element perpendicular to growth field

The reversal of a $4 \times 2 \mu\text{m}^2$ rectangular element aligned such that the major axis of the element is perpendicular to the growth and applied fields, is shown in Fig 4.10. The free layer was saturated by the application of a large field. After reducing the applied field, the reversal was recorded using DPC imaging. At a positive applied field of 12 Oe, a S state was observed. Also visible was a ripple like structure. This is similar to the elements parallel and at 45° to the growth and applied fields where a S state was also observed. Reversal occurred over a wide field range. The structure shown at - 21 Oe persisted beyond an applied field of - 35 Oe.

The return reversal mechanism differed to that of the outward reversal. In this instance, the element formed a flux closure state at one end of the element with the central 180° wall persisting to the other end. This state evolved slowly to applied fields of + 35 Oe. Both the growth and applied fields were along the minor axis of the element. Due to shape anisotropy, the magnetisation would prefer to lie along the major axis of the element. An applied field would have led to the magnetisation lying parallel to the short axis of the element. Reducing this field enabled the element to relax into a state with the magnetisation the long axis of the element. Increasing the field in the opposite direction caused the magnetisation to reverse, once again, lying parallel to the applied field direction and the short axis of the element. It was estimated from the contrast variations in the images sensitive to induction parallel to the major axis that the offset in the hysteresis loop was $\sim + 12$ Oe.

The structural characterisation in Chapter 3 discovered that layer thicknesses were not as expected. In particular, the second Co layer in the AAF was thinner than anticipated, giving an unbalanced AAF. This meant that the free layer would experience some stray field coupling from the AAF. If the

AAF had been perfectly balanced with all layers very smooth, the free layer could be thought of as a single magnetic layer. The field range over which reversal occurs for a single magnetic layer can be estimated by considering the demagnetising factor and the saturation magnetisation. For an element with the applied field perpendicular to the long axis of the element, the offset is

$$\mathbf{B} = (N_l - N_w)\mathbf{M}_s. \quad (4.1)$$

$$N_l = \frac{\pi t}{4l} \left[1 - \frac{1}{4} \frac{l-w}{l} - \frac{3}{16} \left(\frac{l-w}{l} \right)^2 \right] \quad (4.2)$$

and

$$N_w = \frac{\pi t}{4l} \left[1 + \frac{5}{4} \frac{l-w}{l} + \frac{21}{16} \left(\frac{l-w}{l} \right)^2 \right], \quad (4.3)$$

where N_l is the demagnetising factor along the length of the element, N_w , the demagnetising factor across the width of the element, l the length of the element, w the width of the element and t the thickness of the single magnetic layer. The equations were obtained from Chikazumi [68].

Using only first order terms, this simplifies to

$$\mathbf{B} = \frac{\pi t}{4l} \frac{3l-w}{2w} \mathbf{M}_s \quad (4.4)$$

and by substituting suitable values for the length, width and thickness of the element ¹ this gives a field range of ~ 29 Oe over which reversal would occur. This is in reasonable agreement with the experimentally measured field range over which reversal occurred. The difference can be attributed to edge field coupling between the free and pinned layers. Also, the free layer has a small Co layer adjacent to the NiFe layer which will have an affect on the offset along with the stray field coupling due to both layers of the AAF being unbalanced.

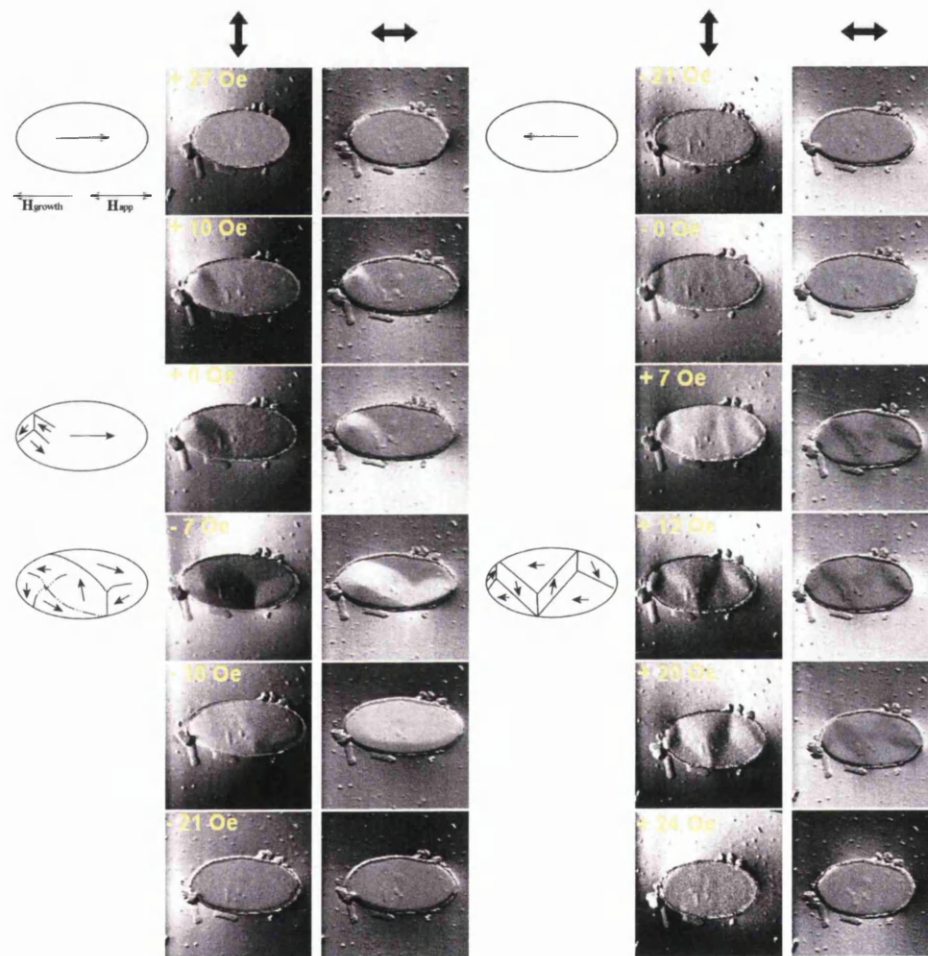


Figure 4.11: Reversal of $4 \times 2 \mu\text{m}^2$ elliptical element parallel to growth field

4.3.5 Reversal of $4 \times 2 \mu\text{m}^2$ elliptical element parallel to growth field

A $4 \times 2 \mu\text{m}^2$ elliptical element, aligned such that the long axis of the element was parallel to the growth and applied fields, was investigated in the Philips CM20 TEM. DPC images of the reversal mechanisms were recorded and are shown in Fig 4.11. The DPC images show there is contamination surrounding the specimen. Some contamination arose from surface defects on the TEM window which were present prior to the deposition of the element. Further contamination occurred during the carbon coating process following deposition of the element. Both forms of contamination were non magnetic and were not believed to affect the reversal of the element.

Prior to recording the reversal, the element was subjected to a large applied field to saturate the free layer. This was reduced and the reversal recorded. DPC images of the outward reversal show that a small vortex formed at $\sim + 10$ Oe near the top left hand edge of the element. As the applied field was reduced through 0 Oe, the vortex moved across the element. By - 7 Oe, the element was near flux closed with two vortices present. These moved towards the bottom edge of the element and were removed as the applied field was increased in the negative field direction. Reversal occurred over a field range of $\sim + 10$ Oe to $\sim - 12$ Oe.

In both the outward and return reversals, the centre of the element reversed before the edges. However, a very different domain structure formed during the return reversal. Here, four central domains effected the reversal, becoming visible at $\sim + 7$ Oe and growing as the magnitude of the applied field increased. Initially the edge domains were large indicating that the magnetisation therein lay in the preferred direction as expected. By + 24 Oe, reversal had completed. This gave an offset in the hysteresis loop of $\sim + 6.5$ Oe.

¹ $M_S = 10864$ Oe for NiFe, $l = 4 \mu\text{m}$, $w = 2 \mu\text{m}$, $t = 9$ nm.

Two points should be noted. Firstly, the lack of corners meant that there were fewer domain nucleation and wall location points than for the rectangular elements. This explains the motion of the vortex across the element during the outward reversal as the domains were not pinned by corners. Secondly, a small imperfection in the edge of the element on the top left hand edge acted as a domain nucleation point for both outward and return reversals. This suggests that ellipses could be susceptible to differing reversal mechanisms.

4.3.6 Reversal of $4 \times 2 \mu\text{m}^2$ elliptical element at 45° to growth field

The reversal of a $4 \times 2 \mu\text{m}^2$ elliptical element aligned so that the long axis of the element was at 45° to the growth and applied field directions was studied. Fig 4.12 shows DPC images of the main points in the reversal cycle. As with the elliptical element parallel to the applied field direction, contamination observed in the images was non magnetic and the investigation was carried out using standard techniques described previously.

Faint ripple was observed in the outward reversal from an applied field of $\sim + 4$ Oe. The ripple intensified leading to the formation of a well defined domain structure by $- 5$ Oe. The centre of the element underwent reversal before the edges with three domains present along the length of the element. The domains were uneven in size, that aligned favourably with the applied field direction being larger. This had been observed previously in the rectangular element with a similar orientation and was to be expected. A small increase in the applied field strength removed the majority of domains with only small edge domains remaining. These disappeared as the applied field was further increased. Reversal occurred over a field range of $\sim - 1$ Oe to $\sim - 12$ Oe.

The return reversal occurred in a not dissimilar manner. Ripple became apparent at $\sim - 0$ Oe, intensified, then domains somewhat reminiscent of those

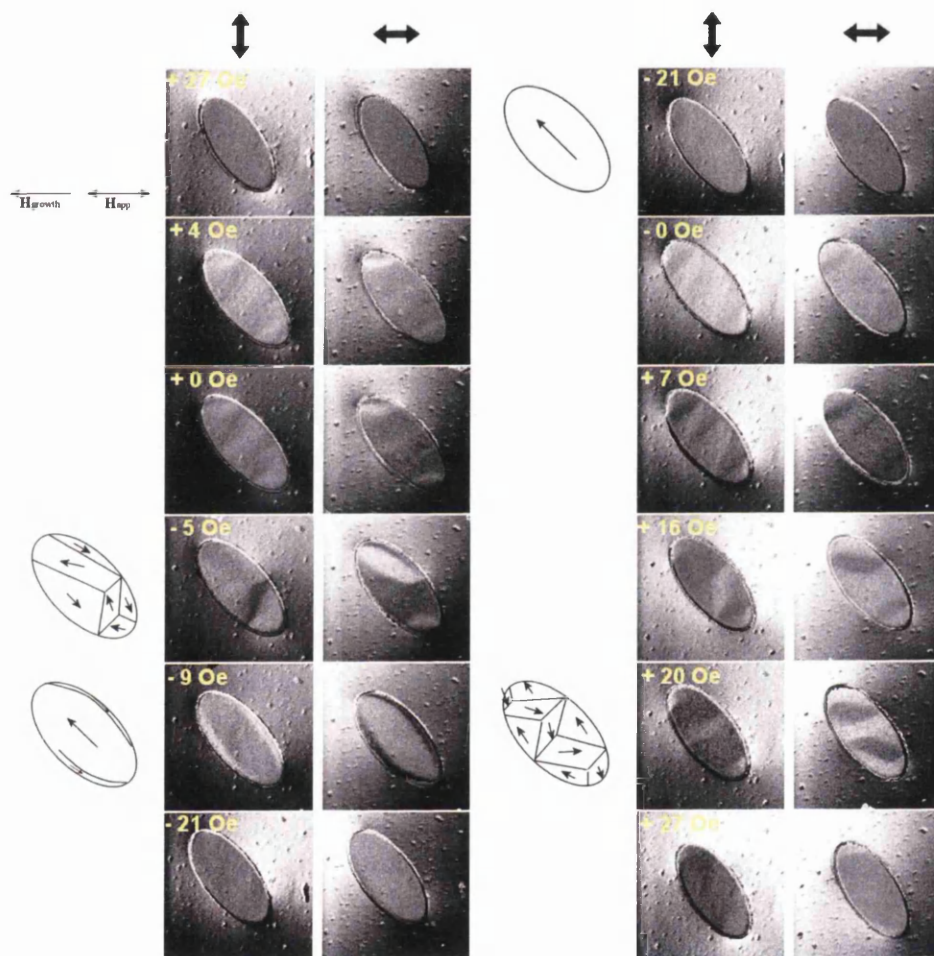


Figure 4.12: Reversal of $4 \times 2 \mu\text{m}^2$ elliptical element at 45° to growth field

in the outward reversal formed. In this instance, five domains were observed along the length of the element. Again, those domains favourably aligned with the applied field were larger in size. The odd number of central domains was necessary due to the orientation of the element with respect to growth and applied field directions. The return reversal occurred over a field range of $\sim + 7$ Oe to -25 Oe giving an offset in the hysteresis loop of $\sim + 7.5$ Oe, similar to the elliptical element parallel to the applied field direction.

4.3.7 Reversal of $4 \times 2 \mu\text{m}^2$ elliptical element perpendicular to growth field

The reversal of a $4 \times 2 \mu\text{m}^2$ elliptical element aligned perpendicular to the applied and growth field directions is shown in Fig 4.13. Contamination observed in the DPC images is non magnetic as discussed previously.

In both the outward and return reversals, the field range over which domain structure was present was greater than that over which images were recorded. Significant points in the reversal are shown in the figure. Domain structure formed during the outward reversal was difficult to observe due to no distinct domain structures. The return reversal possessed a more distinct domain configuration. One point, marked P in the figure, possibly acted as a domain nucleation and wall location point leading to the domain structure shown in the sketch. As the applied field increased in the positive direction, the edge domains reduced in size. The offset in the hysteresis loop was estimated to be $\sim + 7$ Oe.

4.3.8 Discussion

The results presented showed that similar reversal mechanisms were found in the majority of elements, both rectangular and elliptical. The dominant reversal mechanism was where the centre of the element started to reverse

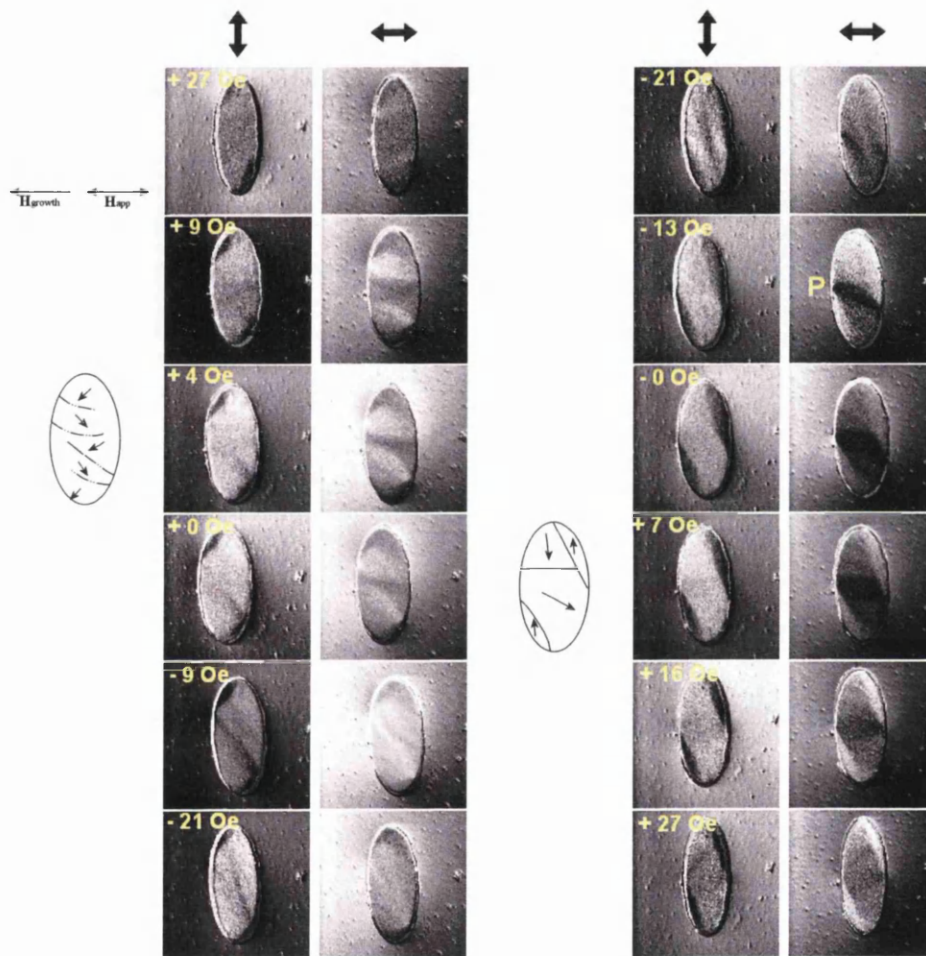


Figure 4.13: Reversal of $4 \times 2 \mu\text{m}^2$ elliptical element perpendicular to growth field

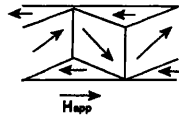


Figure 4.14: Domain structure mid-reversal from an initial S state

before the edges giving a complex domain structure shown in Fig 4.14. Several points regarding the reversal should be noted. Only the elements parallel to the growth and applied field directions could form an initial C state. This led to an even number of central domains whereas an initial S state led to an odd number of central domains. In the elements parallel to the growth and applied field direction, the C or the S state were equally likely. In all elements which exhibited this structure, the edge domains were larger when aligned parallel to the growth field direction. This was due to the initial magnetisation being parallel to the preferred direction. For the elements at 45° to the growth and applied field direction, the domains were not uniform in size. Those aligned favourably with the applied field direction were larger than those aligned in a different direction. This was discussed in Fig 4.9. The number of central domains differed between elements and ranged from 3 to 5 domains.

Not all elements underwent reversal in the same manner. For example, the rectangular element with the long axis perpendicular to the growth and applied field directions formed a flux closure at one end with a 180° wall continuing to the other. The differences observed in the reversal process can be attributed to the orientations of the elements with respect to the growth and applied field directions. The element grown with the long axis parallel to the growth field will be biased along this long axis. However, for the element perpendicular to the growth field, the biasing will be more complex and may be along the short axis of the element. Due to shape anisotropy, the magnetisation of the free layer would prefer to lie along the long axis of the element. These two effects

along with the externally applied field across the short axis of the element have different influences on the domain structure leading to the more complex domain structures observed.

A second difference in the reversal mechanism was observed in the outward reversal of the elliptical element aligned such that the long axis was parallel to the growth and applied field directions. One possibility for the difference is that the elliptical element has fewer points where domains can be easily nucleated and/or walls pinned leading to a more complex domain structure dependent on variations in the local physical structure of the element. In one case, an edge defect acted as a domain nucleation point.

The rectangular elements had offsets in the hysteresis loop of + 15 Oe, + 11 Oe and + 12 Oe for the elements parallel, at 45° and perpendicular to the applied field respectively. These are similar in magnitude which was to be expected as the elements have the same layer structure, growth conditions and shape.

The elliptical elements had offsets of + 6.5 Oe, + 7.5 Oe and + 7 Oe for the elements parallel, at 45° and perpendicular to the applied field respectively. Again, these are very similar in magnitude which was to be expected as the elements have the same layer structure, growth conditions and shape. There was, however, a difference between the magnitude of the offsets between the rectangular elements and the elliptical elements. Also, in all elements, domains persisted over a wide field range giving a broad hysteresis loop without sharp transitions between $\pm M_s$,

4.4 Magnetic Studies of Specimen 1

Specimen 1 was originally chosen for further investigation because this specimen possessed a strongly unbalanced AAF layer structure. The cross section investigation presented in Chapter 3 showed that the layer structure in Å was

Substrate/Ta 108/NiFe Co Cu Co 152/Ru /Co /IrMn 96/Ta 43.

It was originally thought that the second layer of Co in the AAF was 14 Å thick. The results of the cross section investigation in Chapter 3 showed that the thickness of the layer was less than anticipated. Both the Ru and second Co layer of the AAF were too thin to be measured accurately.

For a strongly unbalanced SV element, there should be some stray field coupling between the free and pinned layers in addition to the conventional interlayer coupling. It was thought that this would lead to the specimen behaving more like a conventional spin valve.

In the studies described here, the easy axis reversal mechanisms of the free layer were investigated. A description of the experimental techniques can be found in section 4.3. The as grown states and reversal mechanisms of selected elements for specimen 1 are shown below.

4.4.1 DPC images of the as grown state

Images of the as grown state for the $4 \times 2 \mu\text{m}^2$ rectangular elements are shown in Fig 4.15. It can be observed that the element with its long axis parallel to the growth field direction was in a C state. As shown in section 4.3.3, only elements parallel to the growth field direction have the option of relaxing into a C or a S state. Therefore, the presence of a C state confirms the orientation of the growth field with respect to the elements. The element at 22.5° to the growth field direction exhibited a more complex domain structure with partial flux closure present near the ends. The element at 45° to the growth field showed a deposition or lift-off problem making it difficult to observe any domain structure at one end of the element. Both the elements at 67.5° and perpendicular to the growth field direction were flux closed or nearly so.

Fig 4.16 shows DPC images of the as grown state for $4 \times 2 \mu\text{m}^2$ elements with rounded ends. The element parallel to the growth field direction was in

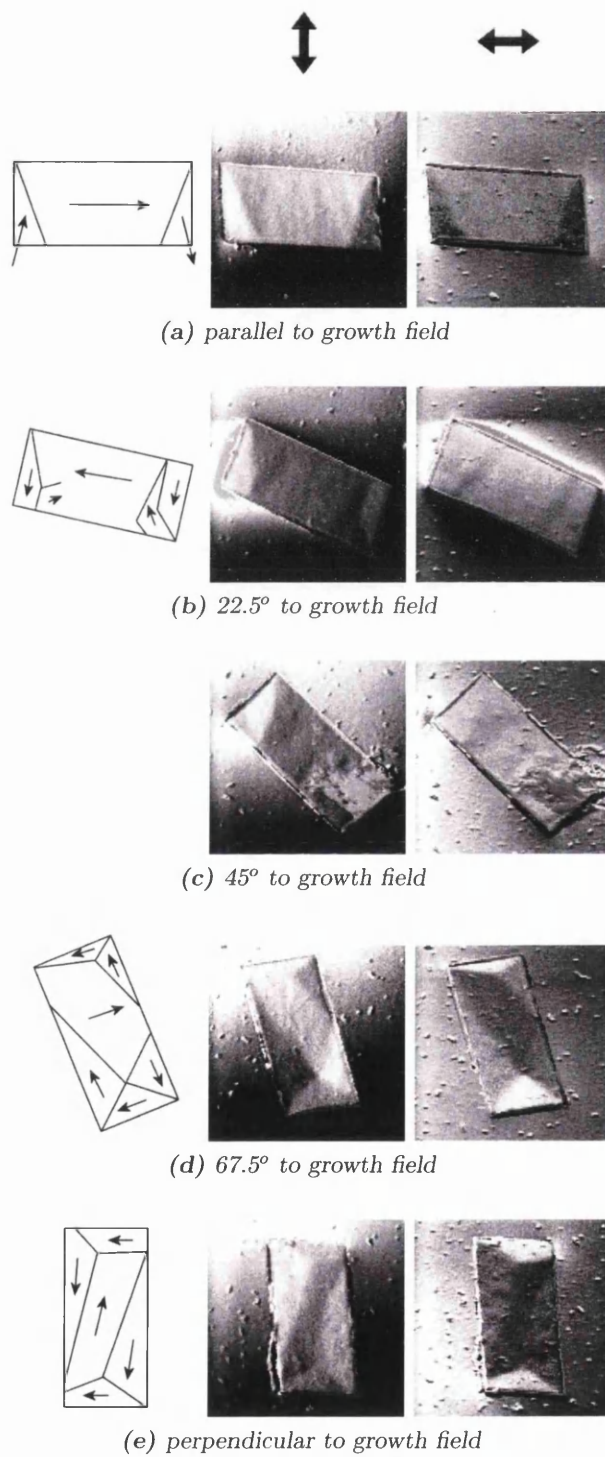


Figure 4.15: DPC images of $4 \times 2 \mu\text{m}^2$ rectangular elements in the as120 grown state

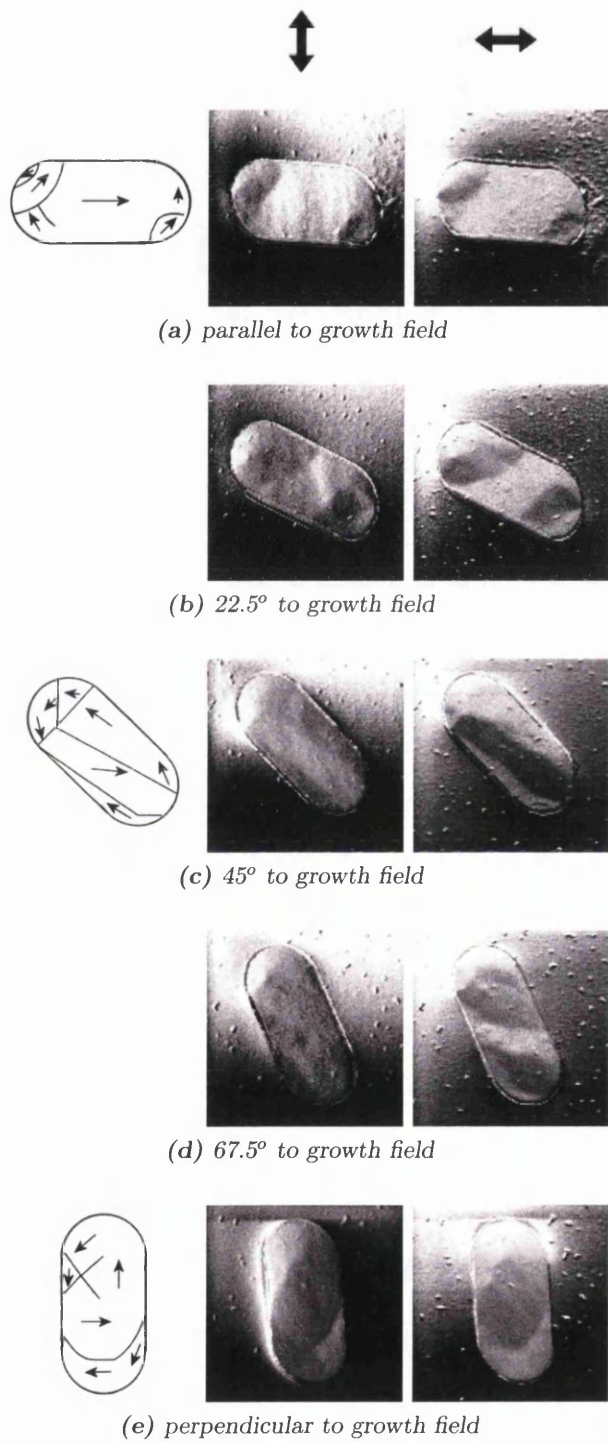


Figure 4.16: Images of $4 \times 2 \mu\text{m}^2$ elements with rounded ends in the as_{121} grown state

a more complex state than its rectangular counterpart. However, it could be seen that the element was in something resembling a S like state. As with the rectangular elements, more complex domain structures were seen in the other four elements. Each element had relaxed into a (near) flux closure structure, the nature of which varied between elements. Sketches adjacent to the DPC images show some of the domain patterns. The lack of corners for domain nucleation and wall location points again meant that the physical structure of the element played a more important role and could have affected the domain structure. The domain configurations observed were more complex than those observed in the rectangular elements.

The $4 \times 2 \mu\text{m}^2$ elliptical elements in the as grown state can be seen in Fig 4.17. Again, complex domain structures were observed. The element lying with its long axis parallel to the growth field direction exhibited a ripple-like structure and was more complex than the rectangular element with this orientation. Both the elements at 22.5° and 67.5° from the growth field direction supported a 3 domain structure with the domains lying approximately along the length of the elements. The element at 45° was in a configuration reminiscent of those frequently observed during reversal in specimen 5 and the element perpendicular to the growth field direction had relaxed into a near flux closure state. Again, without corners acting as domain nucleation and wall location points, the physical structure of the element played a significant role leading to more complex domain structures.

The as grown states for specimen 1 were, in general more complex than those observed in specimen 5. Both the elements with rounded ends and elliptical elements lack domain nucleation points in the form of corners which can give rise to less simple domain structures in elements in the size range studied here. Also, the change in the layer structure by reducing the thickness of the second Co layer in the AAF will have led to a modification in the edge field coupling possibly enabling the formation of more complex domain

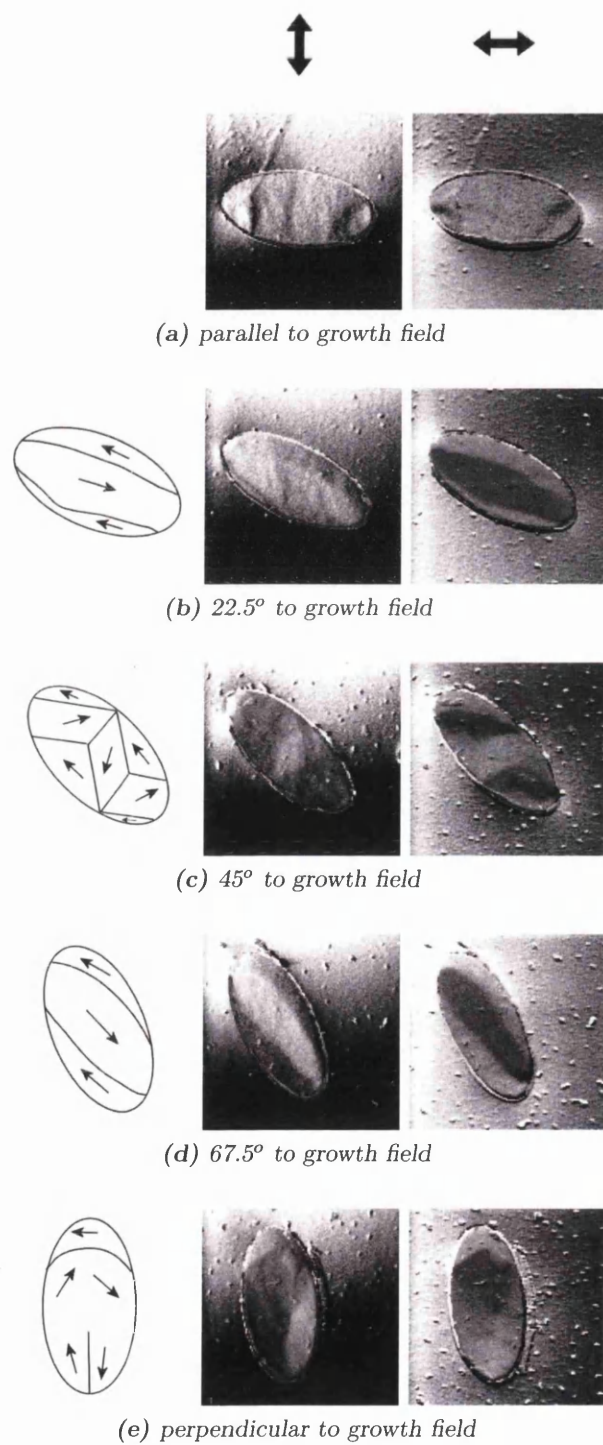


Figure 4.17: DPC images of $4 \times 2 \mu\text{m}^2$ elliptical elements in the as grown₁₂₃ state

structures.

4.4.2 Reversal of $4 \times 2 \mu\text{m}^2$ elements

DPC images of the reversals of a range of $4 \times 2 \mu\text{m}^2$ elements were obtained in a similar manner to the results presented for specimen 5. For the recorded reversals of elements with the layer structure of specimen 1, contrast was often observed in all images of the reversal. It was not clear from which layers the contrast arose although it is unlikely that all the contrast arose from the free layer due to the presence of the structure in all images. This led to the conclusion that there was some variation in the biased layers; in particular, inhomogeneities in the second Co layer of the AAF. Considering the discrepancy between expected and actual thicknesses in this layer, a non-uniform layer was not wholly unexpected.

The presence of domain structure from a layer other than the free layer prohibits analysis such as that given for specimen 5. For this specimen, some of the reversals of higher quality elements will be discussed followed by a range of the observed defects.

Reversal of $4 \times 2 \mu\text{m}^2$ rectangular element parallel to growth field

DPC images of the reversal of a $4 \times 2 \mu\text{m}^2$ rectangular element with its long axis parallel to the growth and applied fields are shown in Fig 4.18. A large positive field was applied to saturate the free layer in the applied field direction which should not have affected the AAF biasing layers. This field was reduced to within the range suitable for imaging. DPC images were recorded over the field range where reversal of the free layer occurred. This was repeated for a field applied in the opposite direction. As the applied field was reduced during the outward reversal, it can be seen that a flower state formed by + 12 Oe. A sketch of the structure can be seen adjacent to the DPC image. As the applied

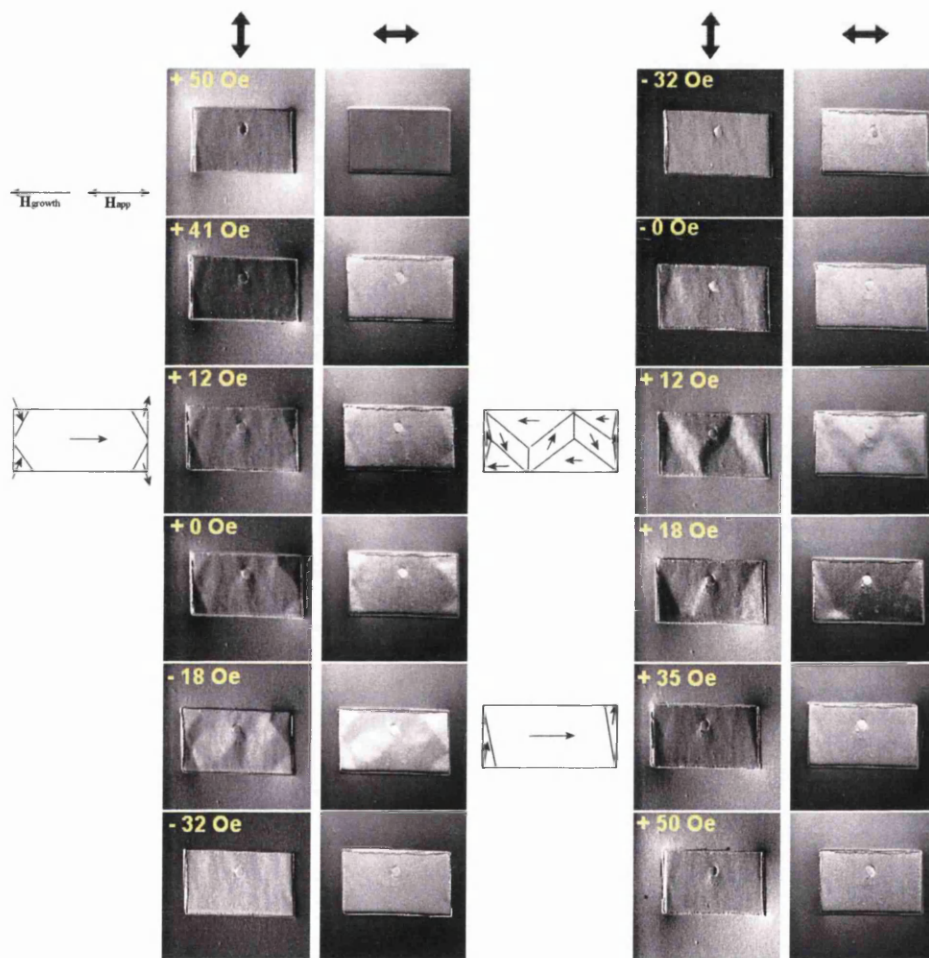


Figure 4.18: Reversal of $4 \times 2 \mu\text{m}^2$ rectangular element parallel to growth field

field passed through 0 Oe and increased in the negative direction, the domains at the corner of the element increased in magnitude and a complex domain state formed in the centre of the element effecting the reversal. Reversal was completed by ~ -20 Oe. All images show a feature close to the centre of the element. This is thought to have arisen in a different layer and does not affect the reversal process.

The return reversal mechanism differed to that of the outward reversal. In this case, a S state formed as the applied field was reduced. At $\sim +10$ Oe, the centre of the element began to reverse giving the complex domain state observed. A sketch adjacent to the DPC images indicates the domain structure. As the applied field increased in the positive direction, the edge domains reduced in size leaving the element in a S state at $+35$ Oe. It should be noted that there were three central domains. The odd number is consistent with the initial S state. From the outward and return reversals, it was estimated that the offset in the hysteresis loop was ~ -1 Oe. The hysteresis loop was broad without sharp transitions between $\pm M_S$.

Reversal of $4 \times 2 \mu\text{m}^2$ elliptical element perpendicular to growth field

The reversal of a $4 \times 2 \mu\text{m}^2$ elliptical element perpendicular to the applied and growth field directions is shown in Fig 4.19. After the application and reduction of a large applied field to saturate the free layer, the magnetisation during the outward reversal formed a C state across the short axis of the element by $+18$ Oe. As the element relaxed further with the reduction in applied field, a vortex was observed near the top of the element. As the magnitude of the applied field increased in the negative direction, the vortex moved along the length of the element with the DPC image obtained at -40 Oe showing the vortex nearing the lower end of the element. The domain configuration did not change past an applied field of -70 Oe and consisted of the majority of the

element reversed into a C state again. A larger applied field would complete reversal. This domain structure has been observed previously by Liu et al [69].

Domain structure was visible during the return reversal by an applied field of - 20 Oe. As the field passed through 0 Oe and was increased in the positive direction, the central, favourably aligned, domain increased in size compressing the lower of the two edge domains by + 30 Oe. The remaining domain structure was removed from the element by + 50 Oe leaving the element in a single domain state. It should be noted that the outward and return reversal mechanisms are significantly different. One explanation could be that a defect (marked D in Fig 4.19) along the edge of the element acted as a domain wall location point in the return reversal. The defect could be a magnetic defect in that changes did occur in the other magnetic layers in the structure due to the imperfectly formed second Co layer. More clear cut examples of domains forming in other than the free layer are discussed in the next section. The estimated offset in the hysteresis loop was $\sim + 1$ Oe.

Reversal of elements with domain structure present in the biased layers

Fig 4.20 highlights some of the persistent domain structures observed in a number of the elements due to a non-uniform second Co layer in the AAF. The first series of images shows the outward reversal of a rectangular element at 45° to the applied field direction. A possible 360° wall was present over most of the field range shown in the image sequence. This domain structure does not greatly affect the reversal mechanism in the free layer as domains which effect the reversal were observed nucleating from the other end of the element. Following reversal, the persistent structure was removed by the application of a large field applied in the negative direction.

The second series of DPC images shows the reversal of an elliptical element parallel to the applied field direction. Contrast was observed across the short

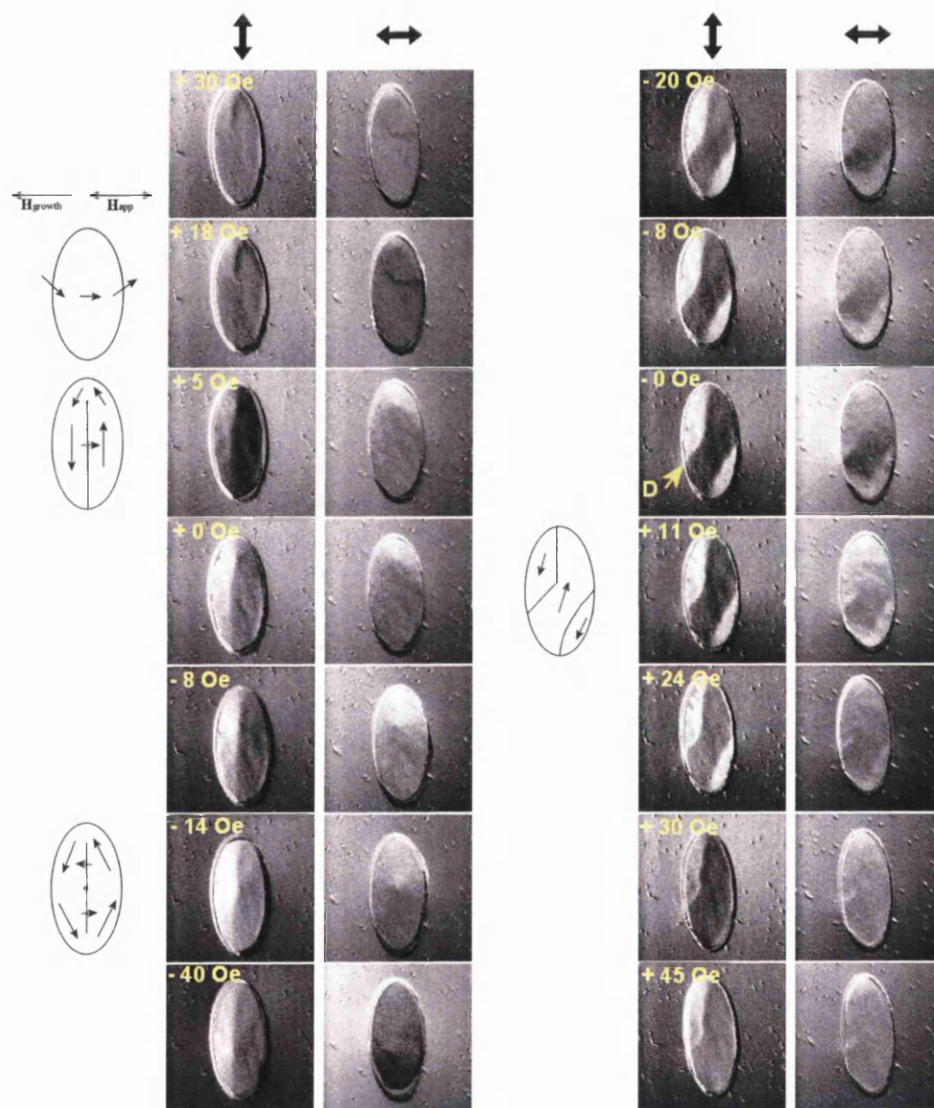


Figure 4.19: Reversal of $4 \times 2 \mu\text{m}^2$ elliptical element perpendicular to growth field

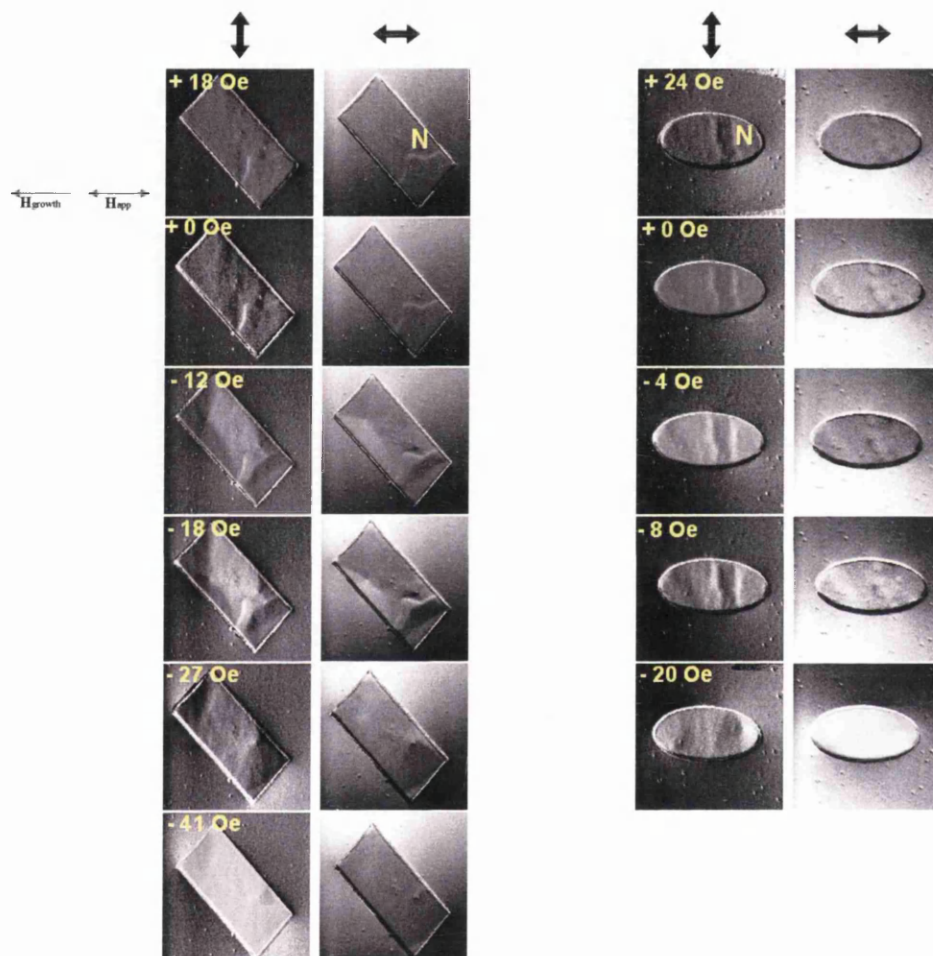


Figure 4.20: Outward reversals of a $4 \times 2 \mu\text{m}^2$ rectangular element at 45° to the growth field and a $4 \times 2 \mu\text{m}^2$ elliptical element parallel to the growth field. In both series, N indicates the non free layer magnetic structure

axis of the element in all images taken. As the field passed through 0 Oe, additional domain contrast became apparent. It intensified up to -8 Oe where reversal was mid-way and reversal completed by -20 Oe. Any role played by the persistent domains is unclear.

4.4.3 Discussion

The reversals of $4 \times 2 \mu\text{m}^2$ elements with the second Co layer of the AAF significantly thinner than that of the first showed more variation in observed reversal mechanisms than those from specimen 5. The large fields applied to fully saturate the free layer are thought to be partially reversing the pinned layers due to the poor quality of the second Co layer and this led to excessive variation between elements. It is difficult to see how the persistent domain structures observed during a number of the reversals could have existed in the free layer.

Of the elements without persistent domain structures, reversals could be rationally described. Similar domain structures to those observed in specimen 5 were seen in some of the elements, the domain structure in the return reversal of the rectangular element shown in Fig 4.18 highlights this.

Also, in the elements that behaved in a comprehensible fashion, the offsets in the hysteresis loops were considerably smaller than those from specimen 5. This could arise from edge coupling from the unbalanced AAF counteracting the interlayer coupling within the element.

4.5 Simulations

Simulations of element reversal processes were undertaken using the Landau-Lifshitz-Gilbert (LLG) simulation package [70]. The package operates by permitting the user to input a starting condition detailing the size, shape, layer structure and materials. Also, the cell size is defined and any applied or in-

trinsic fields are specified. The input parameters enable the calculation of the exchange, anisotropy and magnetostatic energies and external and demagnetisation fields prior to the start of the calculation. The calculation minimises the free energy of the system by solving the LLG equation [71]:

$$\frac{d\mathbf{M}}{dt} = \frac{\gamma}{1 + \alpha^2} \mathbf{M} \times \mathbf{H}_{\text{eff}} + \frac{\gamma\alpha}{(1 + \alpha^2)M_S} \mathbf{M} \times \mathbf{M} \times \mathbf{H}_{\text{eff}} \quad (4.5)$$

where γ is the gyromagnetic ratio and α the damping parameter. H_{eff} is the effective field;

$$\mathbf{H}_{\text{eff}} = \frac{-dE_{TOT}}{d(M_S\alpha)}, \quad (4.6)$$

and incorporates all effects of the exchange, anisotropy and magnetostatic energies and the external and demagnetising fields. For the equilibrium condition, $\frac{d\mathbf{M}}{dt} = 0$ which means \mathbf{H}_{eff} is parallel to \mathbf{M} . This means that the differential equations need not be solved directly. Instead, the magnetisation is relaxed iteratively by positioning the magnetisation along H_{eff} throughout the mesh. When the largest residual of $\frac{\mathbf{M} \times \mathbf{H}_{\text{eff}}}{|\mathbf{M}| |\mathbf{H}_{\text{eff}}|}$ is less than the convergence value set by the user, the calculation will stop. A fuller explanation can be found in Hubert and Schaefer [3] and the LLG package [70]

Due to simulation limitations and the complexity of the system being studied, it was only possible to investigate the smaller elements. It is also due to prohibitively long simulation times for larger elements. To reduce simulation times, the cell size would have had to been increased which led to un-physical results. Simulations were carried out on both balanced and unbalanced AAF systems. Assistance in the setting up of the simulations was given by Mike Scheinfein.

4.5.1 Simulations on a Balanced AAF structure

The simulated layer structure (in Å) was;

$$\text{Co 60/Vacuum 10/Co 60/Vacuum 40/Co 10/NiFe 70.}$$

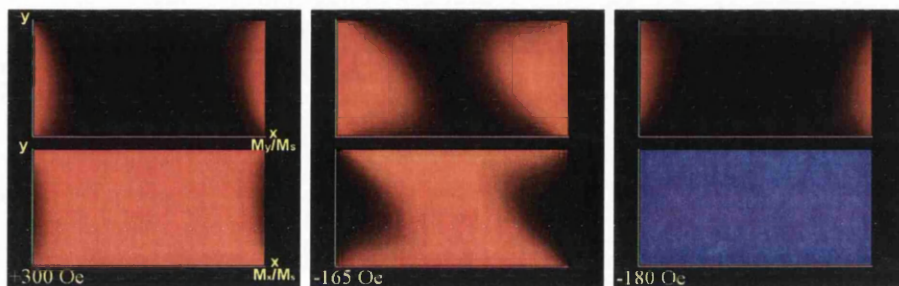
Non magnetic layers were represented by a vacuum and the two, 60 Å, Co layers were pinned antiferromagnetically. The Co/NiFe bi-layer represented the free layer of the experimental system.

The simulated free layer reversal of a $0.4 \times 0.2 \mu\text{m}^2$ rectangular element is shown in Fig 4.21a. The cell size was set at 50 Å in the x and y directions and the thickness of the layer in the z direction for this and all simulations. The field range and number of stages in the hysteresis loops differ between simulations; however, the field step is always set at 15 Oe.

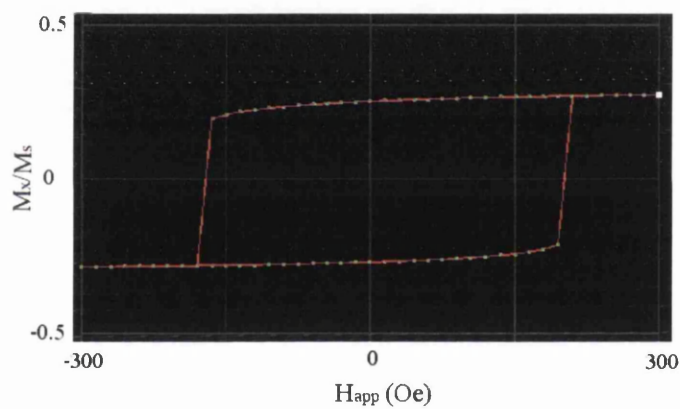
From Fig 4.21a, it can be seen that at the maximum applied field, the element was in a S state. As the applied field reduced and approached that of the reversal field, the magnitude of the end domains increased making the S state more pronounced. Reversal occurred rapidly in both outward and return reversals. The mechanism was similar in both cases, hence only the outward reversal is shown here. The fields at which reversal occurred were - 170 Oe and + 200 Oe and due to the rapid switch, the hysteresis loop, Fig 4.21b, showed a sharp jump. In the hysteresis loop, $M_{Max} \neq M_s$ when the free layer was fully saturated as the loop took into account the magnetisation of all layers. The antiparallel alignment of the pinned layers therefore reduced the magnetisation from M_s .

Using a different viewing orientation, it was also possible to study a cross section of the element, Fig 4.21c. This showed that the only layer in which reversal occurred was the free layer. Both ferromagnetic layers of the AAF were unaffected by the external applied field.

It was not known where the biasing within the elements at 45° to the growth field lay. Two separate simulations were therefore taken representing the two possible extremes. Firstly, a $0.4 \times 0.2 \mu\text{m}^2$ element, biased along the long axis with the applied field at 45° to the long axis was investigated. Secondly, a $0.4 \times 0.2 \mu\text{m}^2$ element with the bias and applied field at 45° to the long axis was studied. The applied field range for these simulations was ± 600 Oe with



(a) LLG images of outward reversal. Red indicates the direction of magnetisation is to the right of the image. The upper image shows magnetisation in the y direction, the lower, magnetisation in the x direction.



(b) Simulated hysteresis loop



(c) LLG images of the cross section. The bottom layer represents the free layer in both images.

Figure 4.21: Simulation of $0.4 \times 0.2 \mu\text{m}^2$ rectangular element parallel to the applied field direction

field steps of 15 Oe. In the first case, reversal occurred in a similar manner to the element with all fields applied along the long axis, with magnetisation reversing through a jump. The outward reversal occurred at - 350 Oe and the return at + 200 Oe. In the second simulation, reversal occurred at - 160 Oe and + 210 Oe.

Simulations of rectangular elements with the applied field and bias across the short axis of the element were investigated. It was found that reversal occurred through rotation. Initially, the magnetisation was parallel to the applied field direction. As this reduced, it rotated to lie along the long axis of the element. As the applied field increased in the reverse direction, the magnetisation rotated once again to lie along the short axis of the element. This occurred over a wider field range than the elements investigated previously.

Reversal mechanisms of elliptical elements were also explored. It was observed that for a $0.4 \times 0.2 \mu\text{m}^2$ elliptical element, with both the pinning and applied fields along the long axis of the element, reversal occurred by a jump as observed previously in the rectangular elements. The fields at which reversal took place were - 145 Oe and + 180 Oe for the outward and return reversals respectively.

An elliptical element with the same dimensions and an applied field at 45° to the biasing direction and long axis of the element was also studied. Again, reversal was via a jump in the magnetisation. Fig 4.22 shows LLG images of the reversal process. The fields at which reversal occurred were - 118 Oe and + 145 Oe. As with the rectangular elements, simulations were also undertaken with the biasing direction and applied field at 45° to the long axis of the element. Reversal occurred by a similar mechanism observed previously at -105 Oe and +150 Oe.

Simulations of an elliptical element with the applied field and bias across the short axis of the element were investigated. Fig 4.23 shows the magnetisation rotating smoothly as the applied field altered. Once again, the reversal

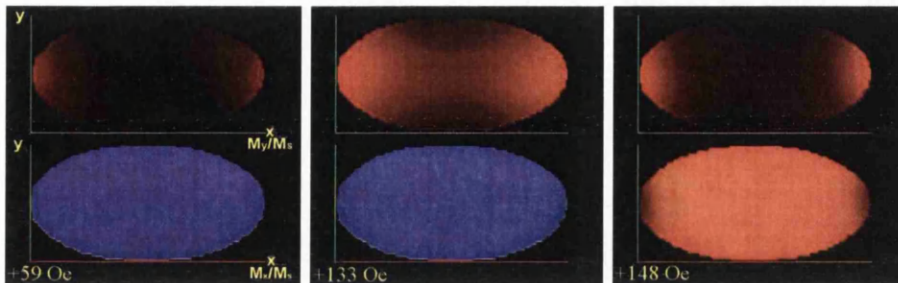


Figure 4.22: LLG images of the return reversal for a $0.4 \times 0.2 \mu\text{m}^2$ elliptical element with the biasing along the long axis and an applied field at 45° to the long axis.

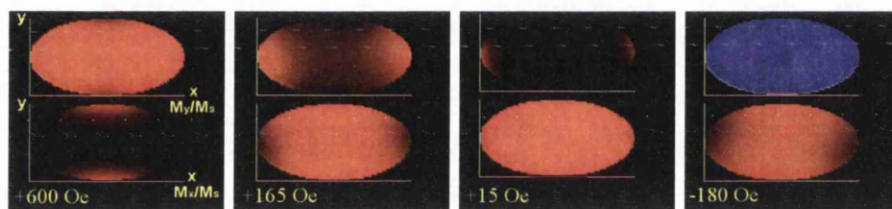


Figure 4.23: LLG images of the outward reversal for a $0.4 \times 0.2 \mu\text{m}^2$ elliptical element with the bias and applied field across the short axis.

occurred over a wide field range.

As discussed previously, time limitations enabled only the experimental investigation of the larger elements. A second limitation was low magnetic contrast levels using DPC imaging due to the element layer structure. The low contrast and lack of domain walls in the smaller elements prohibited Fresnel imaging as an alternative for detailed studies. However, Fresnel imaging could be used to investigate the reversal fields by studying Fresnel fringes surrounding the elements under a large de-focus. As reversal occurred, the fringes changed. Fig 4.24 shows the $0.4 \times 0.2 \mu\text{m}^2$ elements before and after reversal of a number of the elements. Although the differences between the two images are not large, the applied field at which reversal occurred could be noted as it was possible to observe directly any change in the fringes as reversal occurred.

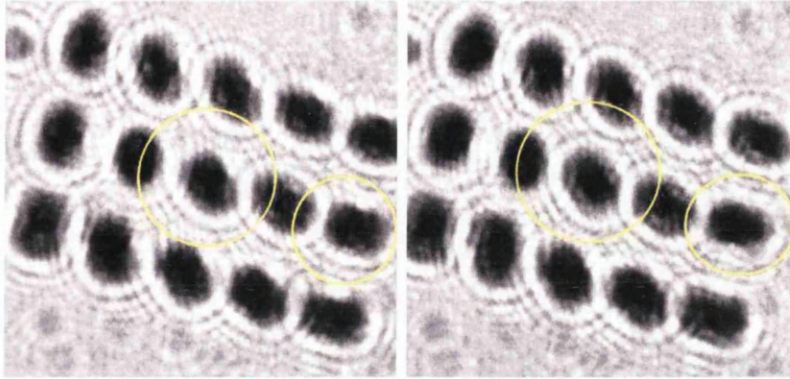


Figure 4.24: Fresnel images of 400×200 nm elements before and after reversal.

Experimental reversal fields were obtained for comparison some of the simulated elements. Table 4.1 shows the experimentally measured and simulated reversal fields. It should be noted that the simulations were undertaken when it was thought that specimen 5 had a balanced AAF. Time constrictions prohibited further simulation of the system, therefore, the comparisons here will not be exact.

For the two elements with major axis parallel to the applied field direction, the fields at which the elements reverse are not too dissimilar and the difference within the offsets are reasonable. This could possibly be improved by simulations using the corrected layer structure. Results from the elements with the applied field at 45° to the long axis of the element have more variation. From these results, it can be seen that one theoretical offset is negative unlike all the others. Discounting this, the other offset is just over half the experimental offset. This implies that the pin within the experimental element does not lie along the long axis or at 45° to the long axis but somewhere in between. Further simulations would be required to confirm this.

Element	Simulation			Experimental		
	Outward	Return	Offset	Outward	Return	Offset
Rectangle, parallel	-170	+200	+15	-150	+175	+12.5
Rectangle, 45 °	-350	+200	-75	-112	+200	+44
	-160	+210	+25			
Ellipse, parallel	-145	+180	+17.5	-100	+125	+12.5
Ellipse, 45 °	-118	+145	+13.5	-150	+220	+35
	-105	+150	+22.5			

Table 4.1: Comparison of experimental and simulated reversal fields. All fields are in Oe. For the elements at 45° to the applied field, the first row corresponds to the bias applied along the long axis of the element. The second row with the bias at 45° to the long axis of the element and parallel to the applied field.

4.5.2 Simulations on an Unbalanced AAF structure

The simulated layer structure (in Å) was;

$$\text{Co 15/Vacuum 10/Co 60/Vacuum 40/Co 10/NiFe 70.}$$

As with the previous simulation, non magnetic layers were represented by a vacuum and the two Co layers were pinned antiferromagnetically by a field of magnitude such that the AAF was unaffected by the field applied to reverse the free layer.

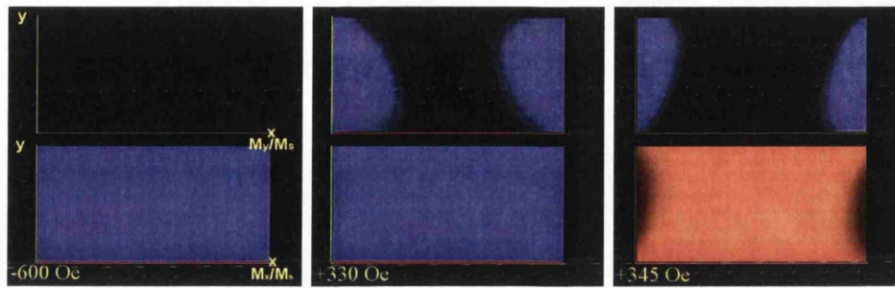
Fig 4.25a shows the simulated free layer reversal of a $0.4 \times 0.2 \mu\text{m}^2$ rectangular element. The cell size was 50 Å in the x and y directions and the layer thickness in the z direction. For this and all simulations in this series, the applied field range was ± 600 Oe with field steps of 15 Oe. From the figure, it can be seen that as the field reduced from the maximum, the element relaxed into a S state. As the applied field approached that at which reversal

occurred, the size of the end domains increased in size leading to a fast switch. The reversal mechanism was similar in both the outward and return reversals; only the return reversal is shown here. Reversal occurred at - 60 Oe on the outward path and + 340 Oe on the return path giving an offset in the hysteresis loop of +140 Oe. The hysteresis loop for the simulated reversal is shown in Fig 4.25b. Due to the hysteresis loop taking into account all layers, $M_x/M_s \simeq 0$ in one orientation of the free layer and $M_x/M_s \simeq 0.75$ in the other. This is different from the balance system where $\pm M_x/M_s$ was symmetric about 0. Although not shown, cross section images were obtained and showed that reversal occurred only in the free layer with the two layers of the AAF remaining unaffected.

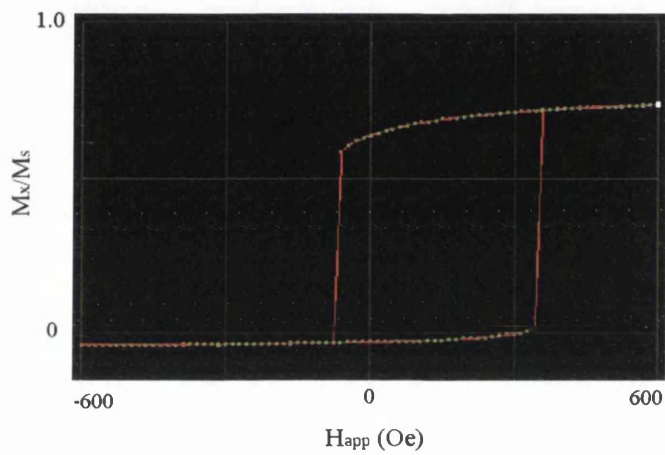
As with the simulations of the balanced AAF with the applied field at 45° to the long axis, two separate simulations were undertaken with the pin parallel and at 45° to the long axis. The fields at which the element pinned parallel to the long axis reversed were - 330 Oe and + 315 Oe giving an offset of - 7.5 Oe. This was significantly different to the simulation where both the pin and applied field were at 45° to the long axis where the reversal occurred at - 30 Oe and + 410 Oe which gave an offset of +190 Oe.

Again, the reversal of elliptical elements were considered. Reversals occurred via a jump in the magnetisation direction in both the elements with long axis parallel and at 45° to the applied field direction. The fields at which the element parallel to the applied field reversed were - 30 Oe and +370 Oe. This gave an offset of + 170 Oe. For the element at 45° to the applied field with the pin along the long axis, the reversal fields were - 100 Oe and +270 Oe giving an offset of +85 Oe. The return reversal is shown in Fig 4.26. The fields at which the element with the applied field and pin at 45° to the long axis of the element were -80 Oe and + 300 Oe giving an offset of +110 Oe.

Experimental values of the reversal fields were obtained for these elements and are shown in table 4.2 alongside the simulation results. It can be seen that



(a) LLG images of outward reversal



(b) Simulated hysteresis loop

Figure 4.25: Reversal of a $0.4 \times 0.2 \mu\text{m}$ rectangular element with applied field parallel to the long axis of the element.

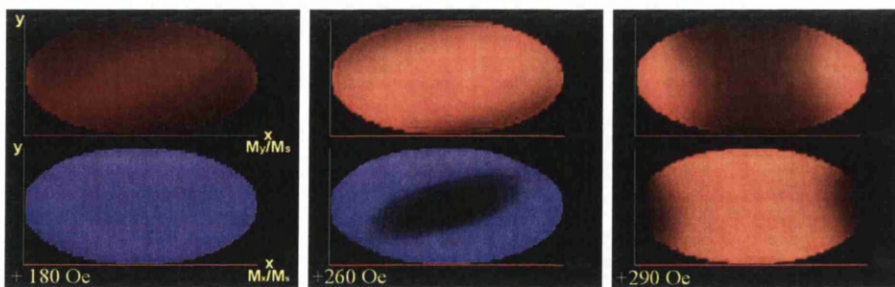


Figure 4.26: LLG images of return reversal of a $0.4 \times 0.2 \mu\text{m}$ elliptical element with the applied field applied at 45° to the long axis of the element.

agreement between the simulations and experimental results is poor. This can be attributed to the second Co layer of the AAF in the specimens being thinner than anticipated and possibly not fully formed which as already seen seriously affected the experimental measurements.

Element	Simulation			Experimental		
	Outward	Return	Offset	Outward	Return	Offset
Rectangle, parallel	-60	340	+140	-100	+120	+10
Rectangle, 45 °	-330	315	-7.5	-140	+230	+45
	-30	+410	+190			
Ellipse, parallel	-30	370	+170	-90	+190	+50
Ellipse, 45 °	-100	270	+85	-115	+170	+27.5
	-80	+300	+110			

Table 4.2: Comparison of experimental and simulated reversal fields. All fields are in Oe. For the elements at 45° to the applied field, the first row corresponds to the bias applied along the long axis of the element. The second row with biasing at 45° to the long axis of the element and parallel to the applied field.

4.6 Conclusion

Specimens 5 and 1 had originally been chosen as it was thought that they represented a balanced and an unbalanced AAF system. Further investigation showed that both specimens possessed an unbalanced AAF with the second layer in the AAF $\simeq \frac{2}{3}$ and $< \frac{1}{4}$ the thickness of the first. DPC images recorded of the reversals of a range of $4 \times 2 \mu\text{m}^2$ elements from both specimens yielded some interesting results.

It was apparent from many of the reversals that one reversal mechanism

dominated. This was where the centre of the element reversed before the edges giving a complex domain structure. From an initial C state, four central domains were present while three or five domains played a major role the reversal from an initial S state. Edge domains were eradicated as the magnitude of the applied field increased.

The reversal mechanism depended on the orientation of the element with respect to the growth and applied field directions. In elements oriented at 45° to the applied fields, domains aligned favourably with the applied field tended to be larger than those not aligned with the applied field direction. More notably, elements perpendicular to both fields had a tendency to form a flux closure state at one end of the element. This was due to competition between the shape anisotropy along the length of the element and the applied field perpendicular to this.

Greater variation in the reversal mechanisms was observed in elements with the layer structure of specimen 1. Accompanying this, some elements possessed a persistent domain structure which did not have its origin in the free layer. One explanation for this is that the second layer of the AAF, being less than 10 \AA thick, had not completely formed creating a non uniform magnetisation in the AAF. This is consistent with the results from the same specimen in chapter 3 where pinholes enabled the formation of persistent 360° walls.

The reversal mechanisms of both layer structures was also dependent on the shape of the element. Elliptical elements, possessing no corners, lacked domain nucleation and wall location points with the local physical structure playing a more dominant role. Accordingly, defects in the elements had a greater effect on the reversal leading to differences in the reversal process.

The shape dependence of the reversal is also seen in the offsets of the hysteresis loops with elliptical elements having a lower offset than rectangular elements in specimen 5. Elements from specimen 1, having a lower offset, generally did not exhibit this difference. Finally, all elements possessed a

broad hysteresis loop with no sharp transitions between $\pm M_s$.

Simulations of the reversal mechanisms of a balanced and unbalanced AAF biased SV with dimensions $0.4 \times 0.2 \mu\text{m}^2$ showed that the reversal of smaller elements was rapid between two stable states of magnetisation. This was also observed experimentally. For the balanced specimen, the fields at which the simulated elements with the field applied parallel to the long axis were in reasonable agreement with the experimental measurements. However, for other elements, agreement was poor. This can be attributed to the poor quality of specimen 1, commented on earlier.

Chapter 5

Transport in Hybrid Magnetic/Semiconductor Devices

5.1 Introduction

Semiconductor heterostructures and their transport properties, introduced in section 1.5.2, can be used to investigate interactions between a magnetic structure on the surface of the semiconductor and electrons in the 2DEG of the system. Such hybrid ferromagnetic metal/semiconductor devices have been investigated for a number of years [72] and may have future applications as magnetic sensors, magnetic memory elements [73] or nanomagnetometers [74, 75] as well as exhibiting interesting fundamental physics. The standard structure for investigating these hybrid devices is a Hall cross with one end of the magnetic material positioned at or near the centre of Hall cross, Fig 5.1a. A second common structure is a Hall bar with a magnetic strip across a constriction between the two sets of voltage probes, Fig 5.1b.

Both device designs operate from the same principles. In each, the stray

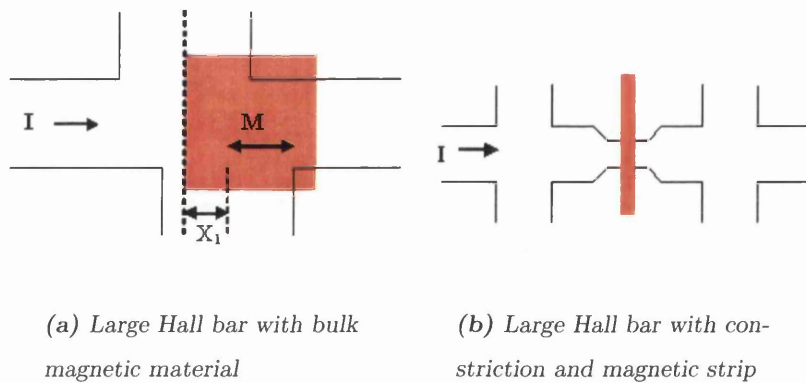


Figure 5.1: Schematic of two common Hall Bar structures for investigating hybrid ferromagnetic metal/semiconductor systems.

field from the magnetic material interacts with electrons in the 2DEG giving a measurable change in the transport properties of the material. The first system with magnetic material positioned at the centre of the Hall cross has attracted considerable interest from a number of research groups. One study by Johnson et al [73, 76, 77, 78] has investigated NiFe elements ($7 \times 7 \times 0.15 \mu\text{m}$) over a Hall cross. The voltage probes are offset by an amount X_1 , Fig 5.1a, introducing a component of longitudinal resistance into the transverse measurement. The magnitude of the offset was chosen so that the measured Hall resistance was zero with the magnetisation of the element saturated in one direction. Reversing the magnetisation gives a non-zero Hall resistance. The two resistance states (Lo and Hi) can be used to determine the magnetic state of the material and hence act as a magnetic sensor.

Using a similar system as above, disks of magnetic and superconducting materials deposited in the centre of a Hall cross have been studied by Geim et al [74, 79, 80, 81]. The Hall probes were $\simeq 1 \mu\text{m}$ in each dimension with the disks having a smaller diameter and a thickness of $0.15 \mu\text{m}$ and the system was used to enable a non-invasive study of the superconducting and magnetic particles.

A cross over between the two principal systems was carried out by Nogaret et al. [82] with the theory being studied by Reijniers et al. [83]. In this case, a long thin ferromagnetic stripe along the length of a Hall bar with a number of voltage probes was fabricated to study snake like electron orbits in a Hall system.

Finally, the second system, where a magnetic strip was deposited over a constriction in a Hall bar was investigated by Kubrak et al [75, 84, 85]. This system was used to detect the magnetic state of the material through changes in the longitudinal resistance whereas the previous results concentrated primarily on the transverse resistance.

Theoretical investigations of the transport of electrons through each of the above systems has been undertaken by Peeters et al. Refs. [86, 87, 88] relate to the systems of Johnson et al. The magnetic disks studied by Geim were simulated in refs [89, 90, 91] and magnetic stripes in [92, 93]. The first system is closely related to the work presented in this chapter and is discussed below.

5.1.1 Hall effect in inhomogeneous magnetic fields

As introduced above, Peeters et al. undertook a theoretical simulation of the experimental work carried out by Johnson et al. These simulations calculate the flux through the Hall cross. A simplified version of the calculations is shown below.

The transverse voltage is

$$V_y = R_H w J_x B_z \quad (5.1)$$

where R_H is the transverse resistance, J_x , the current density and B_z the flux density. Using $J_x = \frac{I_x}{w}$, this gives

$$V_y = R_H I_x B_z. \quad (5.2)$$

Also,

$$R_H = \frac{\Delta B}{ne} \quad (5.3)$$

From these, to calculate the change in resistance through the Hall cross, it is necessary to calculate the equivalent flux through the Hall cross:

$$\Delta B = \frac{\int B \cdot dA}{\int dA} = \frac{\sum B_z dA}{A}, \quad (5.4)$$

where A is the area of the Hall cross. Experimentally, R_H is calculated using the current and transverse voltage. Using equation 5.3, this enables the flux through the Hall cross to be calculated. Theoretically, the flux is summed over the Hall cross area and divided by the area. This can be compared with the value calculated from the experiments.

It should be noted that this approach does not hold in the diffusive limit where the mean free path is approximately that of the Hall bar size. For the experimental work presented in this chapter, the mean free path is greater than the Hall bar size and the system behaves ballistically. Reference [89] shows that the above calculation holds for ballistic electrons. This commonly accepted framework is used as the basis for data interpretation within this chapter.

One result from these calculations is that the flux through the Hall cross varies inversely with the size of the Hall cross. Therefore, reducing the size of the Hall cross effectively enhances any signal from the magnetic material.

The work undertaken in this chapter aims to investigate smaller magnetic elements than those studied previously, by reducing the Hall cross dimensions and using two Hall crosses with the element in the centre of the Hall bar. From this, more sensitive elements such as spin valves could be investigated leading to possible future applications as highly sensitive sensors. The design of a specimen suitable for investigating the structures introduced here is discussed in section 5.3.

This chapter discusses the measuring system used, followed by sample design and development, results of the measurements and discussion.

5.2 Cryostat Design/Operation

To facilitate the investigations into the modulation of the transport properties of the semiconductor substrate by a magnetic element, the specimens were cooled to a temperature of 1.5 K. This was carried out using the cryostat system described below.

The cryostat itself consists of a vacuum jacket, a liquid nitrogen bath, a liquid helium bath and a specimen chamber. A superconducting magnet sits within the He bath providing a uniform vertical field around the specimen. The cryostat used was an Oxford Instruments Teslatron [94].

The sample chamber was cooled by means of a needle valve and a vacuum pump. The valve allows a controlled flow of liquid helium into the chamber. As the liquid evaporated, it was pumped out of the chamber by a vacuum pump lowering the temperature of the system. In this system it was possible to cool the specimen to ~ 1.5 K. A heater, mounted on the inlet to the sample chamber enabled the specimen temperature to be controlled by controlling the temperature of the incoming helium. This enabled the temperature to be set at a desired value. The temperature range for the specimens investigated in this research was 1.5 K to 50 K.

The specimen is placed inside the chamber attached to a sample rod. This rod enables electrical contact to be made between external control and measuring equipment and the specimen. Three different sample rods were used to obtain the measurements. Initially, a rod where the specimen plane was perpendicular to the applied field was used, followed by a second rod where the specimen could be placed in a fixed inclined plane with respect to the applied field. However, with these inserts, in order to alternate between in-plane and

inclined plane measurements, the sample required to be warmed up to room temperature and then re-cooled. This led to difficulties in obtaining a full set of measurements as specimen properties could change between cooling cycles. Also, repeated heating and cooling caused damage to the small gates in the gated specimens (see section 5.3.2) rendering specimens unsuitable for further measurements.

These problems were overcome by the introduction of a new rotating specimen rod designed by Professor Andrew Long and Mr Tom McMullen [95]. This rod enabled the rotation of the specimen plane from an alignment of perpendicular to the applied field through to parallel to the applied field without requiring the heating of the specimen to room temperature.

In both rods where the specimen was at an inclined plane with respect to the applied field, it was possible to determine the orientation of the specimen plane with respect to the applied field by using the change in the conventional, field dependent Hall voltage. In an applied field, with the specimen plane perpendicular to the applied field, the Hall voltage is at its maximum. As the specimen is rotated, the measured Hall voltage drops until the specimen is parallel to the applied field and the Hall voltage is zero. By calculating the gradient of the measured Hall resistance against the applied field at perpendicular and the inclined plane, the values can be manipulated by basic trigonometry to give the angle of inclination of the specimen normal to the field direction.

$$\theta = \cos^{-1} \left(\frac{\frac{dR_H}{dB}}{\frac{dR_H}{dB}} \right). \quad (5.5)$$

Measurements were obtained using the equipment shown schematically in Fig 5.2. A known supply voltage was passed from lock-in ¹ amplifier 1 through

¹A lock-in amplifier contains a phase sensitive detector together with a.c. and d.c. amplifiers and filters. The input a.c. signal is multiplied by the reference signal and the resultant filtered to give an output proportional to the a.c. component synchronous with the reference. The lock-in's used for this work were also capable of supplying an a.c. signal synchronous with the reference which was used to excite the sample.

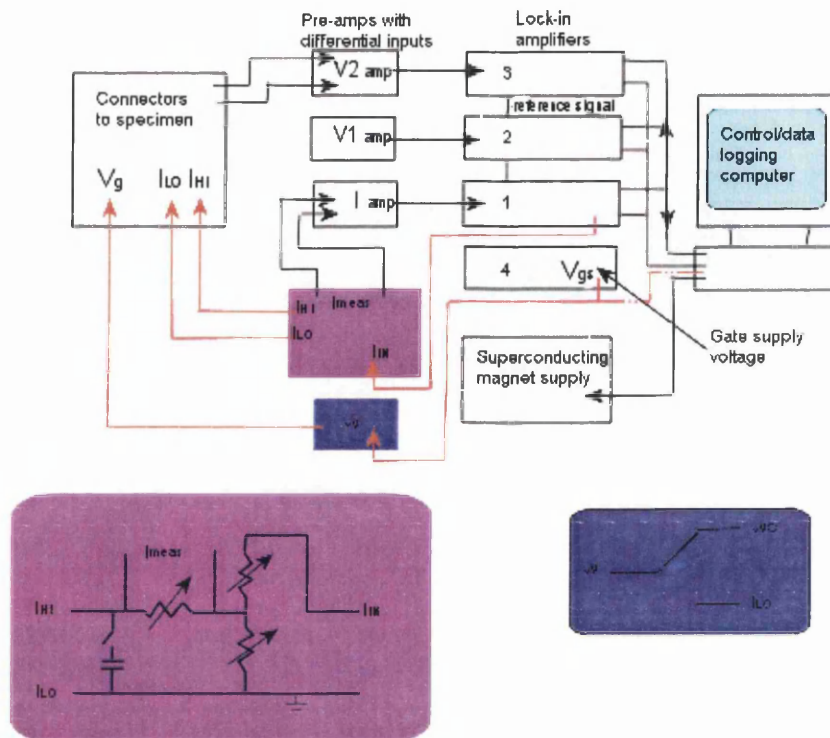


Figure 5.2: Schematic of measurement equipment

the control circuit and specimen. The control circuit (pink inset in Fig 5.2) had four outputs. This enabled the current to be directly measured through one set of outputs (I_{meas}) while the other set of outputs (I_{HI} and I_{LO}) provided the current supply for the Hall bar. Two separate voltage readings could also be measured simultaneously alongside the current using different contacts on the Hall bar.

All three signals were amplified and returned to computer controlled lock-ins. The computer also controlled and measured the magnitude and direction of the applied field. This enabled current and voltage measurements to be obtained at predefined intervals and known applied fields.

A bias voltage could be applied to gates in the specimen using power supply 4. This bias voltage created an electric field around the gates and for a negative

bias voltage, electrons in the 2DEG were depleted from the region under the gate defining the gate pattern into the 2DEG. The gate voltage supply could either be set manually or, for constant applied field, varied using computer control.

The control programmes were written by Dr B Milton [96] using LabView and were modified to record two sample voltages by Dr A Ganjoo. Measurements could then be obtained with the current passed through one set of contacts and voltage measurements taken across other two pairs of contacts. The connections made are discussed further in section 5.4.

5.3 Fabrication of samples

To enable an investigation into the effects of a magnetic element on a semiconductor, a Hall bar structure such as that introduced in section 1.5.2 was used. The Hall bar confined the electrons of the 2DEG into a current channel on top of which the ferromagnetic element was positioned. The particular configuration introduced here was designed to enhance the effects of any modulation of the electrons due to the magnetic element. Due to the complexity of the fabrication process, a number of separate samples were fabricated on one chip, then separated for measurement purposes. This section discusses the sample fabrication techniques particular to these specimens.

5.3.1 Wafer Fabrication

Wafers were grown by the Molecular Beam Epitaxy (MBE) group in the department of Electronics and Electrical Engineering at the University of Glasgow. A brief overview of MBE can be found in Sze [23]. Three different wafers were used in the fabrication of specimens: A1063, A1065 and A971. All are GaAs:AlGaAs heterostructures. Their layer structures are shown in Fig 5.3. Both A1063 and A1065 have a 38 nm deep 2DEG with A971 having a 48 nm

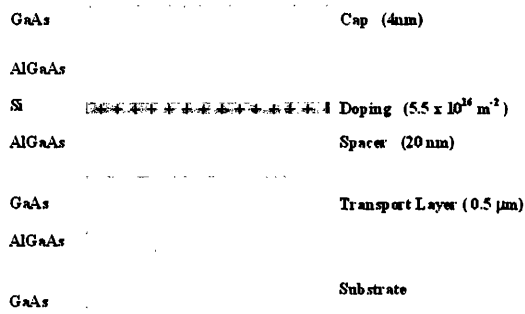


Figure 5.3: Layer structure of A1063, A1065 and A971. Layer thicknesses relate to A1063 and A1065. Not drawn to scale.

deep 2DEG. The depth is measured from the surface of the wafer. The difference between A971 and A1063/A1065 is that the spacer is 10 nm thicker in A971. This will lead to a lower carrier concentration in the 2DEG. A discussion of the modulation doping process used to form the 2DEG can be found in section 1.5.2

5.3.2 Hall Bar Fabrication

Wet-etched structure

The standard design of a Hall bar is well known and documented. Section 1.5.2 introduced the layout and the general transport properties. For the purposes of this research a relatively small Hall bar was required. Initially it was hoped that the Hall bar could be defined in the 2DEG using a wet etch (section 2.3). However, as discussed below, the etched Hall bar proved unsuitable for the desired measurements. A Hall bar of length $2 \mu\text{m}$ and width $1 \mu\text{m}$ of this type was designed using a CAD package (section 2.2.1) with three fabrication layers.

- Alignment marks to enable the registration of subsequent layers.

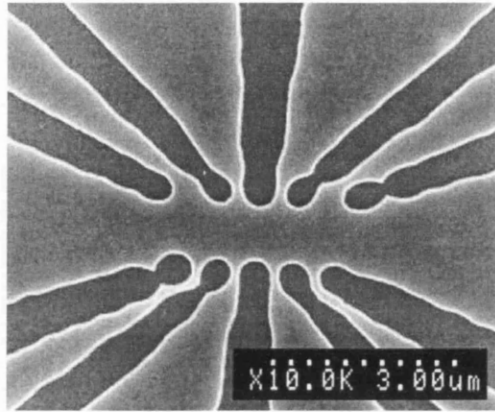


Figure 5.4: SEM image of etched HB. Voltage probes were designed to be 500nm

- Ohmic contacts to establish electrical contact between the 2DEG and an external current supply.
- Isolation to prevent current flow out with the Hall bar.

The fabrication details of each of these layers will be discussed shortly in the context of the successful Hall bar.

Figure 5.4 shows a SEM image of the completed structure. It can be observed that, due to the nature of the wet etch, the structure was not well defined and expanded from the desired dimensions as the depth of the etch increased. This led to the voltage contacts being highly constricted with the specimen unsuitable for further investigation. The bulbous ends at the edges of the isolation defining the Hall bar were typical of one of the difficulties arising from using a wet etch when defining features with small dimensions. If successful, this would have led to a comparatively simple fabrication process which was desirable as it gave a shorter fabrication time, a higher yield and increased reproducibility of specimens.

Structure defined by Schottky gate

In light of the fabrication difficulties defining the Hall bar into the 2DEG by wet etch, a second option of dry etching was considered. However, the expected process development time for this technique led us to dismiss it. Further consideration led to the Hall bar being defined by Schottky gates. These gates did not provide a current path from the external source to the 2DEG. However, when a negative bias voltage was applied to them, the resulting electric field repelled electrons from under the gate, leading to the temporary definition of the Hall bar in the 2DEG.

Fig 5.5 shows the CAD (computer aided design) pattern used for the fabrication of the gated Hall bar. It can be seen that a number of different structures were required. Each of these have a specific purpose and are described below. All follow the standard fabrication procedure introduced in table 2.7. The most important points of each step are described below with the full process being detailed in Appendix A.

Alignment Marks

The first layer to be fabricated consisted of alignment marks (marked A on Fig 5.5). These enabled all subsequent layers to be correctly aligned with respect to one another. This ensured that, for example, the ferromagnetic element was positioned in the desired location with respect to the Hall bar. The alignment marks were metallised using evaporation and lift off procedures. For this, and all other layers requiring metallisation during the fabrication of the Hall bar, the Plassys MEB 450 (section 2.4) was used. The layer thicknesses evaporated for the alignment marks were 33 nm Ti and 160 nm Au. The Ti was essential to achieve good adhesion between the evaporated Au and GaAs substrate as Au has a tendency to lift off when evaporated directly onto the substrate without a buffer layer. The overall thickness was such that the

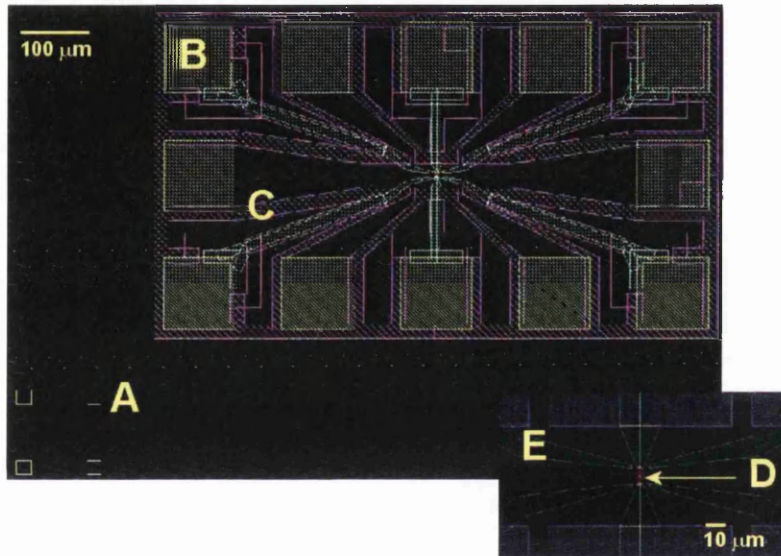


Figure 5.5: WAM [25] (see section 2.2.1) pattern of complete Hall bar layer structure. Inset shows centre of gated Hall bar. A represents the alignment marks, B the ohmics, C the isolation to define the large Hall bar into the 2DEG, D the small gates and E the large gates which define the small Hall bar into the 2DEG.

alignment marks were easily located by the automatic search facilities in the beamwriter.

Ohmic Contacts

The second fabrication layer consisted of the ohmic contacts. (marked B on Fig 5.5). These provided a current path from the surface of the semiconductor to the 2DEG and had dimensions of $150 \times 150 \mu\text{m}$. The dimensions were chosen so that an external current and voltage measurements could be carried out on the specimen through a gold wire bonded to the completed hybrid device. This will be discussed in more detail later. The ohmics comprised a number of evaporated layers. These were;

Ni 8 nm/ Ge 120 nm/ Au 130 nm/ Ni 80 nm/ Au 250 nm.

In this case, the buffer layer providing adhesion to the GaAs was nickel. After the completion of lift off, the substrate was annealed. The annealing process heated the specimen causing diffusion of germanium atoms from the metallised stack through the semiconductor to the 2DEG. The Ge atoms acted as dopants, forming a current path between the 2DEG and an external current source, thus enabling investigation of the completed specimens.

Isolation

The isolation layer was the third layer to be fabricated (marked C on Fig 5.5). This process confined the electrons within the device area by defining a large Hall bar ($100 \times 50 \mu\text{m}$) into the bulk substrate. The Hall bar was defined using a wet etch (section 2.3) to remove material to a depth of 40 nm, isolating the 2DEG from the surrounding material. The fabrication difficulties observed in the previous design were not found here as the dimensions etched were considerably larger. This large, etched Hall bar enabled basic characterisation

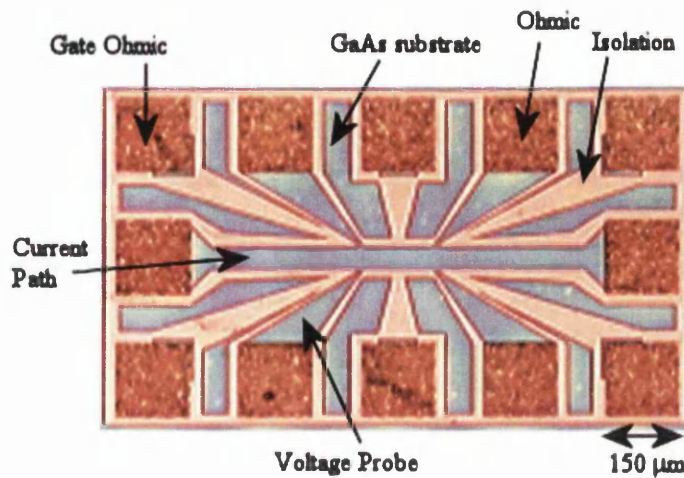


Figure 5.6: Photograph of ohmic contacts (orange) and isolation(buff). The GaAs substrate regions are blue/grey. The gated layers were added to the pattern layer

investigations into the bulk substrate. Fig 5.6 shows a photograph of the ohmic and isolation layers after fabrication.

Gates

The fourth and fifth layers (D and E on Fig 5.5) defined the small gates which were used to form a $2 \times 1 \mu\text{m}$ Hall bar at the centre of the larger etched Hall bar. Due to the dimensions of this smaller Hall bar, it was necessary to use two fabrication layers. The first of these, layer D, defined the central region of this smaller Hall bar using 12 nm Ti and 15 nm Au. The second, layer E, linked the central region of this gated Hall bar to the ohmic contacts. Layer E was considerably thicker (Ti 33 nm/Au 160 nm) than layer D. This thicker layer prevented cracks and breaks in the gates. A $2 \mu\text{m}$ overlap joined the two layers and provided current continuity. The thicker layer of metal was not used for the centre of the Hall bar as the thickness was two thirds

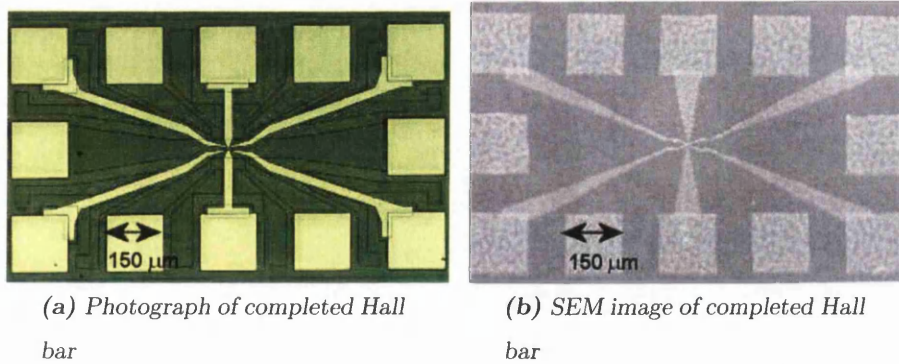
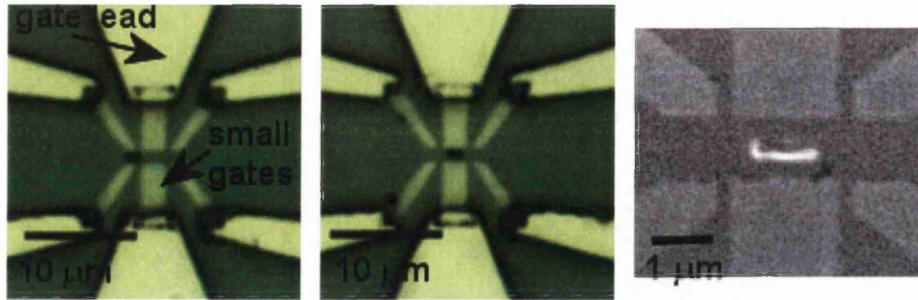


Figure 5.7: Completed Hall Bar

the width of the voltage probes and could have led to difficulties with lift-off at the high resolution required and when the gates were being defined by a biasing voltage. The ohmic contacts in this case, were contacts which were isolated from the 2DEG of the Hall bar by the isolating wet etch enabling electrical contact to be made to the gates without affecting the 2DEG of the Hall bar. Ohmic contacts were used to reduce the number of fabrication layers (fabricating contacts for the gates and the Hall bar unnecessarily increases the complexity of the design). An example of a gate ohmic is shown in Fig 5.6. It can be observed that isolation surrounds the ohmic contact, preventing current flow between the gate ohmic and the 2DEG of the Hall bar.

Figure 5.7 shows images of the completed Hall bar structure on a large scale. Both the large Hall bar etched into the substrate and the smaller, gated Hall bar can be seen in the photograph. In the SEM image, however, only the leads to the smaller gated Hall bar can be observed. The SEM detects backscattered electrons and the gold in the gates has a higher atomic weight compared to the GaAs substrate, therefore reflecting a higher proportion of electrons into the detector. The difference is such that the contrast can not be adjusted to observe both the gated and the etched Hall bars simultaneously in a SEM image.



(a) Photograph of magnetic element positioned with one end lying in the centre of a Hall cross

(b) Photograph of magnetic element positioned in the centre of the Hall bar

(c) SEM image of magnetic element positioned in the centre of the Hall bar

Figure 5.8: Small Hall bar indicating positions of $1 \times 0.5 \mu\text{m}$ magnetic elements.

Ferromagnetic elements

Magnetic elements were evaporated onto the surface of the Hall bar using the thermal evaporator in the physics department (section 2.4). They consisted of $1 \times 0.5 \mu\text{m}$ or $1.5 \times 0.5 \mu\text{m}$ rectangular elements positioned either with one end lying in the centre of a Hall cross (Fig 5.8a) or with the rectangular element in the centre of the Hall bar (Fig 5.8b, 5.8c). The materials used were either Cobalt or Permalloy with thicknesses of 50 nm and 20 nm respectively.

Cleaving and Bonding

As stated earlier, a number of samples were fabricated onto one chip. The spacing between bottom left hand corners of each sample was $1.5 \text{ mm} \times 1.0 \text{ mm}$. After completion, the samples were cleaved into individual specimens. To enable an investigation to be carried out, individual specimens were mounted onto a chip carrier using a conducting adhesive known as silverdag. Silverdag is a silver loaded conductive paint with a low resistance. The chip carrier

was of sufficient size to be handled easily without damaging the specimen and external current and voltage supplies could be connected with relative ease using the sample rod introduced in section 5.2. Gold wires of diameter $25\ \mu\text{m}$ were attached between the sample and contacts on the chip carrier by a process known as bonding, enabling the current to pass through the sample and voltages to be measured.

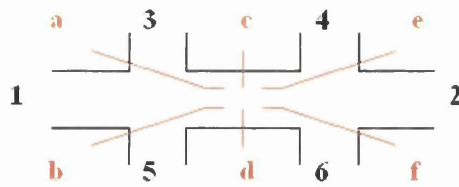


Figure 5.9: Schematic of large Hall bar. Gate positions for small Hall bar are shown in orange.

5.4 Experiments

Results are presented from a series of samples: basic Hall bars to characterise the substrate, investigate any non-magnetic modulations of the traces and characterise the equilibrium carrier concentration and mobility; Hall bars with 50 nm thick Co elements; and Hall bars with 20 nm thick NiFe elements. The investigations were all undertaken using the low temperature system described above. The aim was to progress from investigating single layer elements to spin valve elements. However, due to persistent adhesion problems between the Ta seed layer and GaAs substrate, it was not possible fabricate spin valve samples in the time available. It should be noted that the measure of magnetic field used in chapters 3 and 4 was oersteds. For Quantum Transport measurements, it is usual to quote B values in teslas (T) to characterise a magnetic field and will be the unit used here.

5.4.1 Large Hall Bar

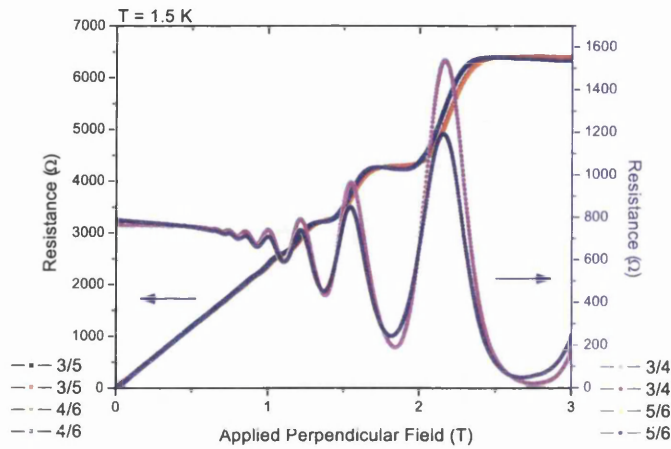
A schematic of the basic large Hall bar is shown in Fig 5.9. Numbered contacts were those used to supply and measure current and voltage. Lettered contacts were those used to define the small Hall bar using gates. For investigations on the large Hall bar, the lettered contacts (gates) were connected to the current low. In a typical experiment, the first measurements characterised the bulk substrate using the large Hall bar. This enabled the equilibrium carrier

concentration and mobility to be calculated, and gave an indication of the quality of the semiconductor substrate. In this measurement set, the current was passed between connections 1 and 2 with 3/4 (5/6) giving the longitudinal voltage and 3/5 (4/6) giving the transverse voltage.

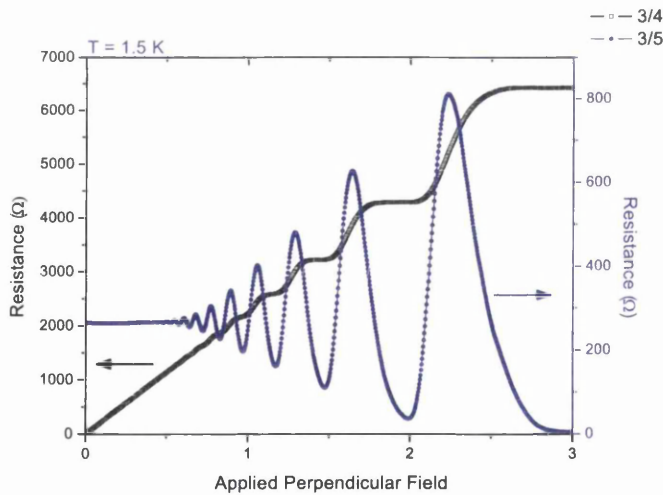
The bulk transport measurements for two basic Hall bars are shown in Fig 5.10. The first, Hall bar A (Fig 5.10a), was a Hall bar taken from near the edge of wafer A971 whereas the second Hall bar, B (Fig 5.10b), was taken from near the centre of wafer A1065. The differences between the two sets of traces in Hall bar A in both transverse and longitudinal measurements showed that the voltage probes were not identical. This sort of distortion of the Shubnikov de Haas amplitude or transverse resistance is not unusual. The carrier concentration and resistances (and hence the mobility) hardly differ. It was not possible to obtain transport measurements from both sides of Hall bar B due to difficulties with contacts. A discussion of the plateaux and the Shubnikov-de-Haas oscillations can be found in section 1.5.2. It should be noted that, as expected, minima in the Shubnikov-de-Haas oscillations occur at the same fields as Hall plateaux.

From these results, the longitudinal and transverse measurements were used to calculate the carrier concentration. For each specimen, the two values calculated from the different measurements were consistent. For Hall bar A, a carrier concentration of $n_{2D} = 2.60 \pm 0.03 \times 10^{15} \text{m}^{-2}$ and mobility $\mu = 8.5 \pm 0.3 \text{ m}^2 \text{ V}^{-1} \text{ s}^{-1}$ were calculated. The mobility was less than ideal; reasons for this are discussed below. For Hall bar B, the carrier concentration was $n_{2D} = 2.80 \pm 0.03 \times 10^{15} \text{m}^{-2}$ and the mobility $\mu = 30.1 \pm 0.3 \text{ m}^2 \text{ V}^{-1} \text{ s}^{-1}$ which was much more desirable for the specimens investigated here. The errors stated above for both the carrier concentrations and mobilities are applicable to all subsequent calculations. As such, they will not be stated explicitly but all results can be assumed to have similar errors present.

In all wafers tested, it was found that the mobility was dependent on the



(a) Bulk measurement for Hall bar near edge of wafer (A971). High longitudinal resistance (right hand Y axis) at $B=0$ ($R \simeq 800 \Omega$) indicates low mobility.



(b) Bulk measurement for Hall bar near centre of wafer (A1065). Lower longitudinal resistance (right hand Y axis) at $B=0$ ($R \simeq 300 \Omega$) indicates a more desirable mobility.

Figure 5.10: Bulk substrate characterisation measurements

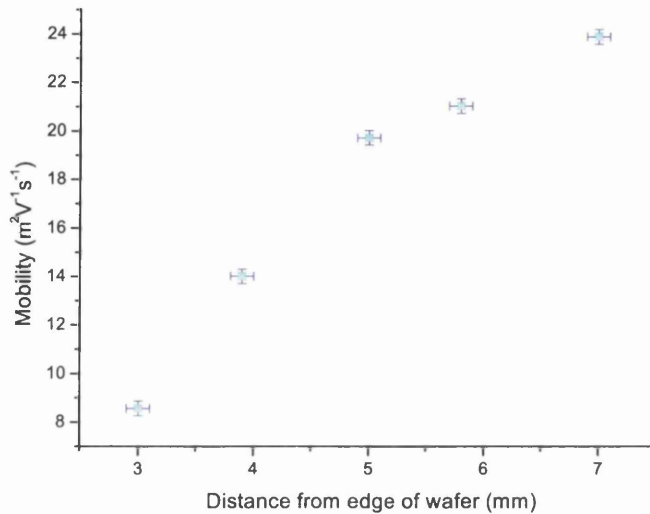


Figure 5.11: Variation of mobility with distance from edge of wafer (A971)

position of the specimen with respect to the centre of the substrate wafer. Fig 5.11 indicates the change in mobility with radial position from the edge of wafer A971. One possible explanation for this is a lack of uniformity in the any layer giving carrier concentration fluctuations in the wafer as a lack of uniformity in one layer will translate to all other layers. The lack of uniformity arose due to rotation during the MBE process which affects peripheral samples more than those from the centre of the wafer. From this result, the low mobility observed in the first bulk substrate measurements would not be unexpected. An explanation of the lower carrier concentration (and hence mobility) of A971, is that the deeper 2DEG of A971 would have led to a lower carrier concentration than either A1065 or A1063 if both samples had been taken from similar positions on the wafer.

Following measurements of the large Hall bar, gates were defined and checked. Both two terminal and four terminal measurements of resistance against gate voltage were taken. Fig 5.12 shows a graph typical of those ob-

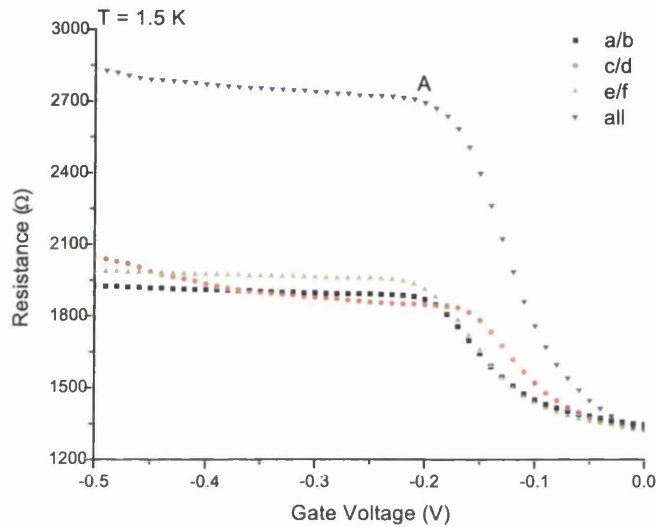


Figure 5.12: Two terminal gate characterisation (A1065)

tained for a two terminal measurement. This gate measurement was taken from sample B (wafer A1065) discussed earlier. The graph shows that at low applied gate voltages, there was no gate definition and the measured resistance was that of the large Hall bar. The high resistance at $V_g = 0$ V was due to both the current and voltage using connections 1/2, i.e. the 2-terminal technique. As the gate voltage was increased, the measured resistance began to increase. The region where the resistance was increasing indicated that the field from the gates was repelling electrons from under the gates and constricting the electron channel. Above a maximum applied voltage, the small Hall bar was fully defined in the 2DEG, the gate definition did not change significantly and there was little change in resistance. For this sample, it can be observed that gate definition commenced at ~ -0.1 V, full definition of the Hall bar occurred at ~ -0.2 V and beyond this the definition did not change greatly. The two terminal gate measurement confirmed that each pair of gates were working correctly and were not significantly damaged by the fabrication process. Us-

ing the information obtained, the most suitable gate voltage was applied to the samples to fully define the small Hall bar without risking damage to the gates could then be determined. This was just as the resistance measurement began to flatten out again after gate definition (point A in Fig 5.12).

One further point to consider is that for a conventional transport system, each gate pair could be considered as a variable resistor. With each pair defined individually, a change in resistance of $\Delta r \simeq 600 \Omega$ was measured for this specimen between $V_g = 0 \text{ V}$ and $V_g = -0.25 \text{ V}$. Defining all gates simultaneously could be represented as three resistors in series. It could be expected that classically, the change in resistance, ΔR , over the same applied gate voltage range would equal the sum of the changes in resistances of each gate pair, i.e.

$$\Delta R = \sum_{1-3} \Delta r \simeq 1800\Omega. \quad (5.6)$$

The measured change in the resistance with all gates defined gave $\Delta R \simeq 1450 \Omega$, which was less than anticipated for a conventional transport system. The mean free path length was calculated using

$$l = (R_c B) \mu = 2.5 \mu\text{m}, \quad (5.7)$$

where $R_c B = 1.651 \times 10^{-15} \text{ n}^{\frac{1}{2}} \text{ mT}$ at low temperatures. By considering the Hall bar as a series of three separate constrictions, the mean free path length is considerably greater than the length of each constriction and is comparable with the separation between the constrictions and therefore transport is ballistic. Therefore, equation 5.6 is not true. Similar systems for single constrictions have been investigated by van Houten et al [97], Thornton et al [98] and Wharam et al [99]. Wharam et al [100] showed experimentally that for a series of constrictions, $\Delta R \neq \Delta r_1 + \Delta r_2$, the same result observed here.

Due to the gates being defined electrostatically, the Hall bar pattern defined into the 2DEG alters as the applied gate voltage is altered. To help characterise this change, it was useful to take a second set of gate measurements using a

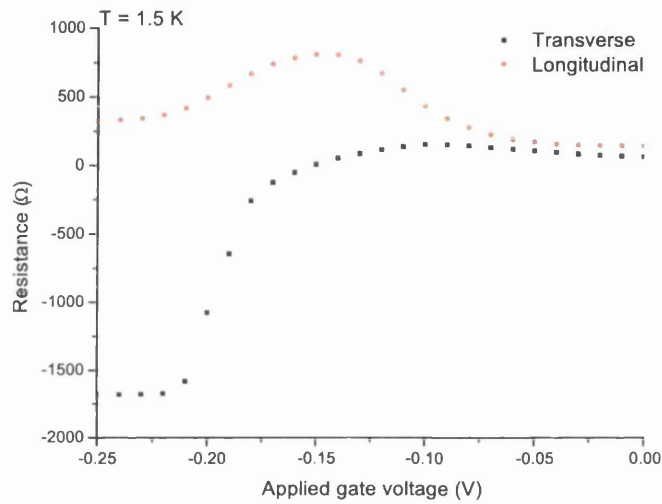


Figure 5.13: Four terminal gate characterisation. (A1063) All gates connected together, $I = 1/2 V_T = 3/5$ and $V_L = 3/4$. The reduction in the longitudinal resistance was unexpected and was not found on other specimens. The origin of this effect in this sample is unknown.

four probe arrangement. This led to results such as those in Fig 5.13. It can be observed that the longitudinal resistance increased with the constriction of the current channel. The transverse resistance however, changes sign with increased applied gate voltage. This can be observed in the measurements and gives a range of Hall offsets observed in all specimens. The change in the Hall offset due to applied gate voltage for this specimen is large. They can, however, be considerably smaller or vary between positive and negative depending on fabrication differences and differences in the underlying current flow patterns in different samples. Any changes in the Hall offset due to geometrical influences will be noted in the relevant sections.

Longitudinal and transverse magneto-resistance measurements of the specimens were then taken with the small Hall bar defined. There was little difference between the transverse traces of the large and small Hall bars (Fig 5.14). The offset at zero applied field is due to the gate definition of the small Hall bar as discussed above. This specimen exhibits a considerably smaller offset due to geometrical influences. Both traces show plateaux at the same fields and gave the same carrier concentration as the bulk measurement.

For Hall bars with magnetic elements, two offsets in the Hall measurement were observed. The first is the geometric offset due to the Hall bar definition by gates and the second is an offset due to the magnetic element. The magnetic contribution gives rise to a small hysteresis loop in the transverse measurement and will be discussed in more detail later.

In the longitudinal measurements, there was a notable change at low field between the large and small Hall bars. This is illustrated in Fig 5.15. The downward trend of the longitudinal resistance at low field was a common feature of all specimens, with and without a magnetic element, when the small Hall bar was defined. This decrease in resistance was ascribed to a mesoscopic shape effect arising from diffuse boundary scattering. This magnetostatic effect is further discussed in Thornton et al [98], and Beenaker and van Houten [101],

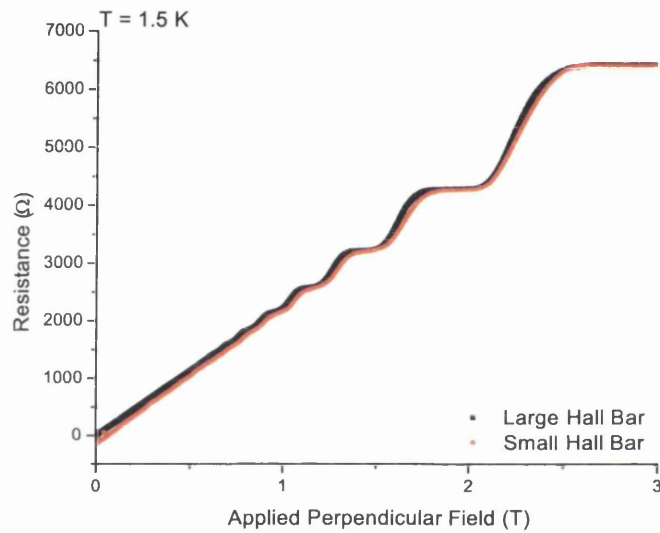


Figure 5.14: Comparison of the transverse measurements between the large etched, and small gated Hall bar in A1065. The carrier concentration is unaffected by the change in Hall bar dimensions although a non-magnetic change in $R_{B=0}$ is observed. This 150 Ω offset arose from the change in the applied gate voltage.

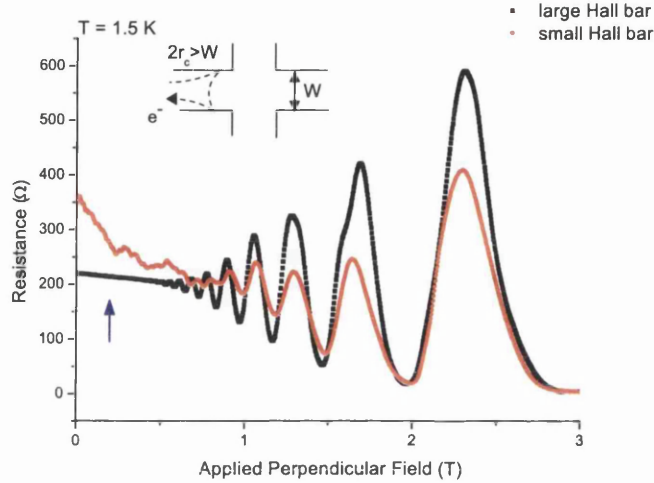


Figure 5.15: Longitudinal measurement on the same sample as shown in Fig 5.14 with small Hall bar defined, using contacts 4/6 on A1065.

section 5. At low applied fields, the electron mean free path length is greater than the width of the electrostatically defined Hall bar, i.e. the cyclotron diameter, $2r_c$, is larger than the channel width, W . Under these conditions, diffuse boundary scattering effects can reverse the direction of electron motion along the channel increasing the measured resistance. This is shown schematically in the inset of Fig 5.15. As the magnitude of the applied field is increased, the cyclotron diameter is reduced, equations 1.22 and 1.23. At the applied field when the cyclotron diameter becomes less than the channel width, diffuse boundary scattering can no longer reverse the direction of electron motion, i.e there is a reduction of backscattering with magnetic field and the measured resistance becomes the same as the bulk value.

The characteristic field over which the resistance would change depends on the cyclotron orbit and applied field. For these specimens, $r_c B = 100$ nm. The Hall bar width of $W = 1 \mu\text{m}$ gives a maximum cyclotron orbit of $r_c = 0.5 \mu\text{m}$ for diffuse boundary scattering. This gives a characteristic field of $B = 0.2$ T

which is the same field range over which the drop occurs, as seen in Fig 5.15 and Fig 5.16.

The detail within the mesoscopic resistance shape effect varies from specimen to specimen but is not affected by the presence of a magnetic element. The detail arises from mesoscopic fluctuations in the electron paths. At low fields, the mean free path is greater than the size of the Hall bar and electrons undergo many small angle scattering events before a large angle collision. Increasing the applied field affects the small angle scattering events, changing the electron trajectories and creating fluctuations in the measured resistance. These fluctuations are not self averaging as active areas of the device are small.

It was expected that the detail within the mesoscopic resistance shape effect would reduce with an increase in temperature. This was observed and is shown in Fig 5.16. As the temperature increases, the number of inelastic scattering events will increase due to increased thermal vibration of atoms within the 2DEG. This is particularly important in reducing mesoscopic fluctuations as inelastic scattering destroys the coherence of the electron waves.

It was also expected that the detail within the longitudinal shape effect would vary with applied gate voltage. A change in the applied gate voltage would alter the definition of the Hall bar and its position with respect to the scattering potential environment. It would also slightly decrease the electron concentration in the small Hall bar, hence making potential fluctuations more significant. This was also observed, Fig 5.17. In this sample, full gate definition was attained with an applied gate voltage of -0.25 V. With an applied gate voltage less than this, the Hall bar would not be fully defined, the voltage probes would be larger than expected and less detail in the resistance measurement would be expected. This was seen in the -0.1 V and -0.2 V traces. Above the full definition voltage, more detail would be expected in the trace at low fields, increasing with applied gate voltage and was found in the -0.3 V and the -0.4 V measurements. For a larger gate voltage, the transport channel would

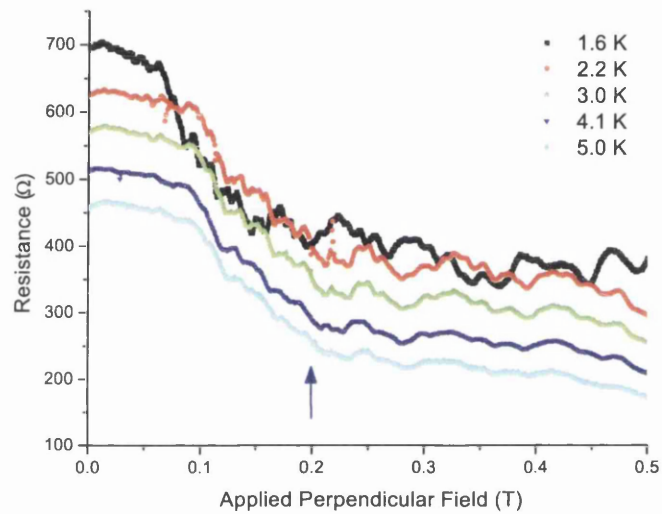


Figure 5.16: The change in longitudinal resistance with T (A1065). The measurement taken at 1.61 K is the original measurement with all higher temperatures being moved 50 Ω with respect to one another to enable easier comparison. $V_g = -0.15$ V

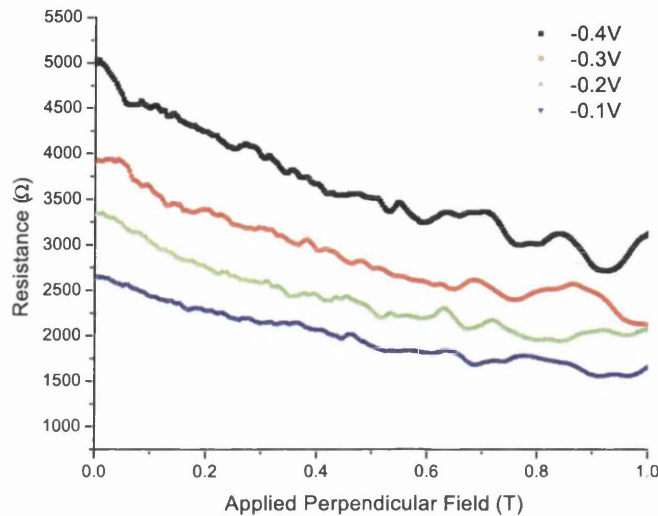


Figure 5.17: The change in longitudinal resistance with applied gate voltage. 2 terminal gate measurements (A1065).

have been considerably narrower than for lower gate voltages. The narrower channel means that collisions would have a greater effect on the measured resistance. Also, as the applied gate voltage increased, the Hall bar would increasingly constrict the current flow leading to a higher average resistance as observed in Fig 5.17.

5.4.2 $1500 \times 500 \times 50$ nm Co element with one end over a Hall cross

A $1500 \times 500 \times 50$ nm cobalt element was evaporated onto a Hall bar with one end of the element over a Hall cross. An SEM image of the specimen can be seen in Fig 5.18. All results from this and sections 5.4.3 and 5.4.4 were obtained using wafer A1063.

Due to the failure of contact 2, it was not possible to use conventional current contacts. This led to either 1/4 or 1/6 being used for the current

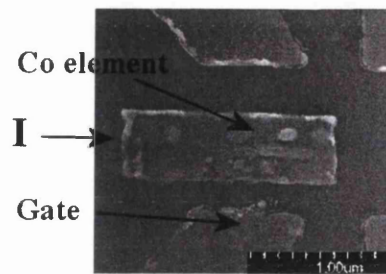


Figure 5.18: SEM image of specimen

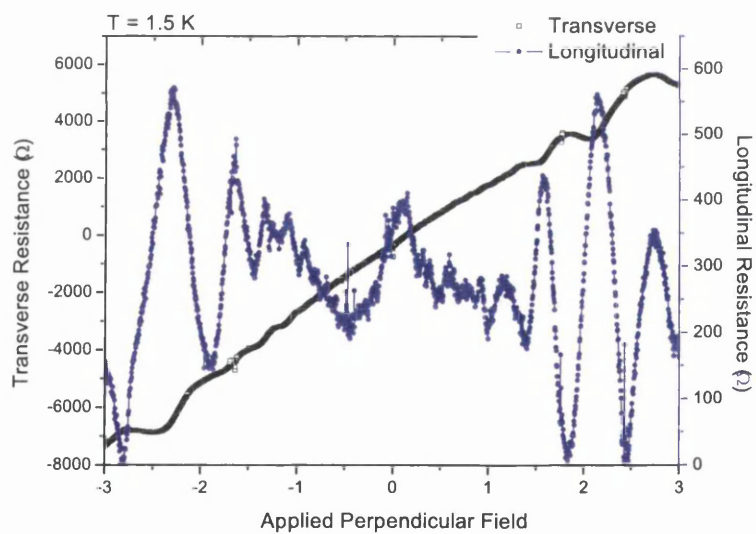


Figure 5.19: Cross coupling of signals in small Hall bar. $I = 1/4$, $V = 3/5$ (transverse) and $5/6$ (longitudinal). $1500 \times 500 \times 50 \text{ nm}$ cobalt element with one end of the element over a Hall cross.

and 3/5 (5/6) being used as voltage probes with I being contacts 1/4, and 3/5 (3/4) being used with I through contacts 1/6. The principal difference between these measurements and measurements with a full set of contacts is that there is some cross coupling of signals. Fig 5.19 shows transverse and longitudinal measurements from the specimen. It can be observed that in the transverse trace, instead of the expected plateaux, the resistance begins to oscillate in a similar manner to the longitudinal resistance measurement. These oscillations are evidence of some cross coupling between the longitudinal and transverse measurements. It should be noted that this effect is only appreciable at fields greater than 1T and is therefore not of significance in the measurements obtained here where the region of interest is less than 0.4 T. It is still possible to obtain the bulk characteristics of the material and for this specimen, $n_{2D} = 3.3 \times 10^{15} \text{ m}^{-2}$ and $\mu = 51 \text{ m}^2 \text{ V}^{-1} \text{ s}^{-1}$. This is a high mobility for the specimen range investigated and as expected, the specimen came from near the centre of the wafer.

Element			Mesoscopic Effect
Material	Size (nm)	Position	Field Range (T)
None			$\simeq \pm 0.2$
NiFe	$1000 \times 500 \times 20$	one end over Hall cross	$\simeq \pm 0.2$
	$1500 \times 500 \times 20$	one end over Hall cross	$\simeq \pm 0.25$
Co	$1500 \times 500 \times 50$	one end over Hall cross	$\simeq \pm 0.4$
	$1500 \times 500 \times 50$	centre of Hall bar	$\simeq \pm 0.25$
	$1000 \times 500 \times 50$	centre of Hall bar	$\simeq \pm 0.35$

Table 5.1: Applied field range over which mesoscopic effects occur for different element size, location and materials.

Fig 5.20 shows the longitudinal trace in perpendicular field of the small electrostatically defined Hall bar. Mesoscopic shape effects were observed. As

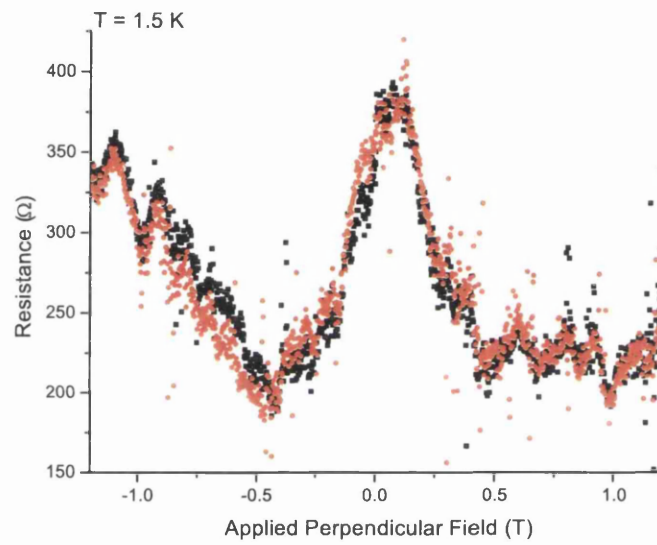


Figure 5.20: Longitudinal measurement of electrostatically defined Hall bar. $I = 1/4$, $V = 5/6$. $1500 \times 500 \times 50$ nm cobalt element with one end of the element over a Hall cross.

discussed in the section 5.4.1, the shape effects were not of magnetic origin and arose from comparable magnitudes of the Hall bar dimensions and the electron mean free path. One interesting difference between this measurement and those taken from the basic Hall bars is that the field range over which the mesoscopic effect occurred is not the same. Table 5.1 shows the change in field range of the mesoscopic effects due to different element sizes, locations with respect to the Hall bar and material. The NiFe elements have little effect on the range over which the effects occur. However, the Co elements can have a much more significant effect on the field range. A number of mechanisms could account for the effect. The NiFe is thinner than the Co and has a smaller M_S . If the expansion of the field range depends on the stay field of the element as well as the standing field, this explains the effect only being significant for Co elements. Also, the stray field from the element could act to further constrict the Hall bar, increasing the applied field range over which diffusive boundary scattering occurs. Currently, there is not sufficient evidence to conclusively determine which, if any of these theories are correct or whether a combination of effects are occurring.

Little magnetic information can be obtained while the applied field is perpendicular to the specimen plane. In order to progress further, the specimen was rotated until the applied field direction is near parallel to the specimen plane. Fig 5.21 shows the longitudinal and transverse measurements taken at a small angle ($0.1^\circ \pm 0.03^\circ$) from the in-plane field. Each set of results was repeated on two consecutive days with the sample warming to 50 K overnight. The results showed that the magnetic effects were similar over the two days, although the absolute resistance changed. This indicated that the results were reproducible with a stable hysteresis loop and magnetic reversal cycle. The change in resistance was dependent on the cooling and warming cycles and can vary from day to day. Measurements were obtained at a temperature of 5 K as there was a reduction in noise within the measurements and the temperature

control mechanism was more stable at this rather than lower temperatures.

The residual gradient in Fig 5.21 was due to a slight misalignment of the sample field to the applied field direction. The calculated field angle is $\sim 0.1^\circ$ from the in-plane field. The Hall gradient can be subtracted from the results using the transformation equation shown in Fig 5.22. This transformation gives a hysteresis loop with a step of $3 \pm 0.2 \Omega$, Fig 5.22. Using the equation

$$\Delta R_H = \frac{B}{ne} \quad (5.8)$$

where ΔR_H is the step in the resistance and n the carrier concentration, this gives a mean flux density change through the Hall cross of $\simeq \pm 0.8$ mT for the reversal of the magnetisation of the sample.

The flux through the Hall cross can also be simulated. Two different methods of simulating the flux are shown below.

The first uses three assumptions to calculate the flux per unit area at the end of the magnetic element going into the Hall cross. Firstly, it is assumed that the element is magnetised uniformly and that all external flux originates at the end of the element. Secondly, that the flux splits up and down equally so that half of the flux goes through the Hall cross. Finally that $B \simeq \mu_0 M$ and is much greater than H inside the element. From these, the flux is

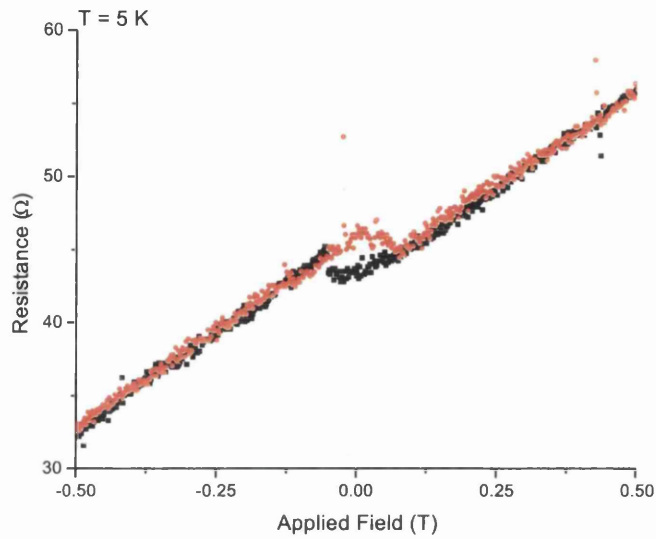
$$\phi \simeq \frac{\mu_0 M}{2} \times hW, \quad (5.9)$$

where $M = M_S$, the saturation magnetisation of the element, h is the element thickness and W the width of the element. From this, the flux density through the Hall cross can be calculated using

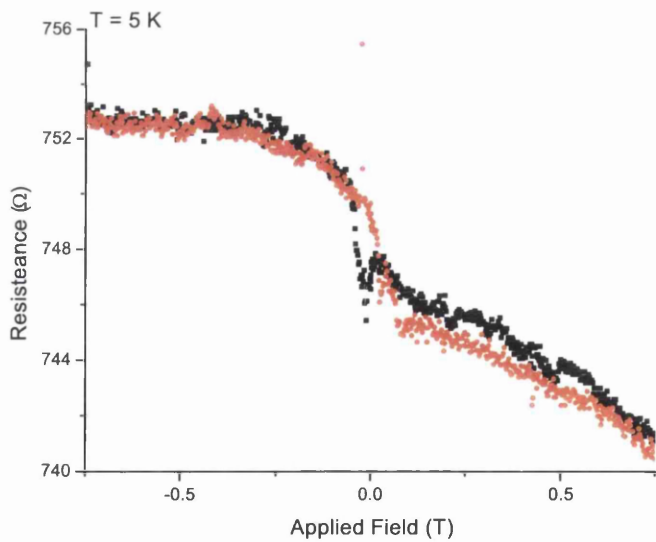
$$B = \frac{\phi}{A}, \quad (5.10)$$

where A is the area of the Hall cross. Using $\mu_0 M = 1.82$ T for cobalt² and the element dimensions defined previously, this gives a flux through the Hall cross

²For Co, $M = 1.42 \times 10^6$ A m⁻¹ [1]



(a) transverse measurements



(b) longitudinal measurements

Figure 5.21: Transverse and longitudinal measurement close to an in-plane applied field. $I = 1/6$, $V = 3/4$ (longitudinal) and $3/5$ (transverse). $1500 \times 500 \times 50$ nm cobalt element with one end of the element over a Hall cross.

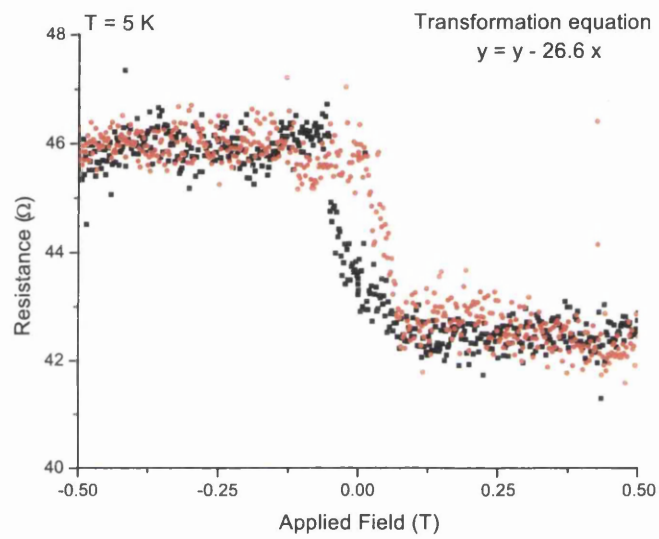


Figure 5.22: Transverse measurement from Fig 5.21a with the Hall gradient subtracted. $1500 \times 500 \times 50$ nm cobalt element with one end of the element over a Hall cross.

of 0.07 T. This estimated value of the flux through the Hall cross is greater by an order of magnitude than the measured value. This calculation is a useful tool for understanding the basic mechanisms involved but needs to be refined to confirm that the poor agreement is not an artefact.

The second method of calculating the flux through the Hall cross also assumes that the element is magnetised uniformly with a magnetisation $\mathbf{M}(\mathbf{r})$. This element can be represented as the sum of the volume charge and surface charges

$$\text{divM}dV + \mathbf{M} \cdot d\mathbf{S}. \quad (5.11)$$

The flux at a plane below the specimen can therefore be calculated by taking into account the surface and volume charge distributions and integrating over the thickness of the specimen.

This method is non-trivial and is complex to carry out analytically. However, a method using Fourier Transforms has been developed which simplifies the calculations somewhat. Full details of the calculations can be found in Beardsley [102] and a more accessible treatment in McVitie et al. [48, 103]. To undertake the transformations, an assumption that the magnetisation does not vary through the specimen thickness is made. The transform is calculated in a plane parallel to the plane of the film and is a 2D transform with the magnetisation split into $M_{x,y}$ and M_z (in plane and out of plane components). Calculations of the fields are made using Fourier transforms in the xy plane with Fourier space coordinates $\mathbf{K} = k_x\hat{x} + k_y\hat{y}$. The expression for the out of plane component of field in Fourier space is

$$H_z(K, z) = \left(\frac{-i[K \cdot M_{xy}(K)]}{K} + M_z(K) \right) \sin \left(\frac{Kt}{2} \right) \quad (5.12)$$

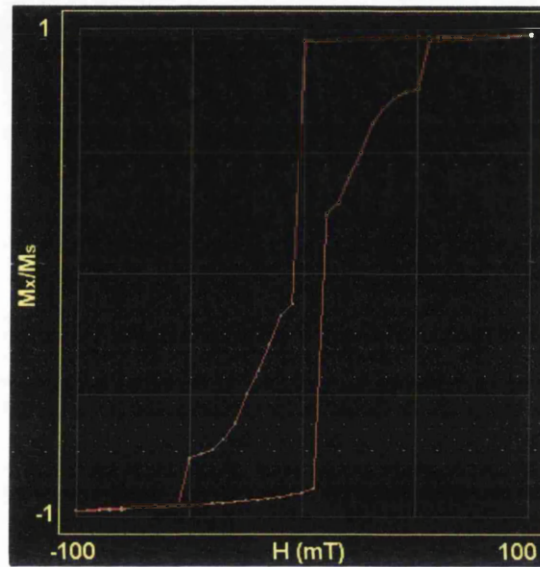
where $i = \sqrt{-1}$, t is the specimen thickness and z the distance of the xy plane from the centre of the specimen. This can be inverse transformed to calculate the real space field for any plane with $z > 0.5t$.

This simulated out of plane component is equivalent to the out of plane field

contributing to the Hall offset measured experimentally. The Fourier transform technique was applied to simulations of the magnetic element using the LLG [70] magnetics package. The calculations on the element were undertaken using the Fast Fourier Transform package available as part of the Digital Micrograph [104] package. The K space functions and magnetic data were controlled by scripts written by Mr Gordon White under the supervision of Dr Stephen McVitie.

The reversal process of a $1500 \times 500 \times 50$ nm Co element was simulated using the LLG package to investigate the flux density through the Hall cross from the element. Fig 5.23a shows the hysteresis loop from the reversal of such an element. This loop indicates that the element reverses over ± 60 mT which is comparable to the experimental loop, Fig 5.22 where reversal occurs over ± 80 mT. The shape of the simulated hysteresis loop indicates that domain processes were involved in the reversal. Figs 5.23b and 5.23c show the magnetic state of the element at 0 and -5 mT respectively. These show that the element relaxed into a flower state as the applied field approached zero and that a small reverse field induced a jump into a flux closure domain state. The favourably aligned domain grows as the applied field increased in the negative direction until the magnetisation approaches a uniform value. For an element of this size, this is not unexpected.

Fig 5.24 shows the out of plane field component at the 2DEG for a simulated Co element in a single domain state and a line scan taken across the centre of the element. In general, some of the flux can be seen to arise from along the side edge of the element. Using the out of plane field components from the element, the flux through the Hall cross can be calculated by summing the field value at every point over the area of the Hall cross with respect to the magnetic element. From this, the simulated mean flux density through the Hall cross was found to be ± 29 mT. This is considerably better than the first estimate but is still much larger than the measured flux through the Hall



(a) Hysteresis loop

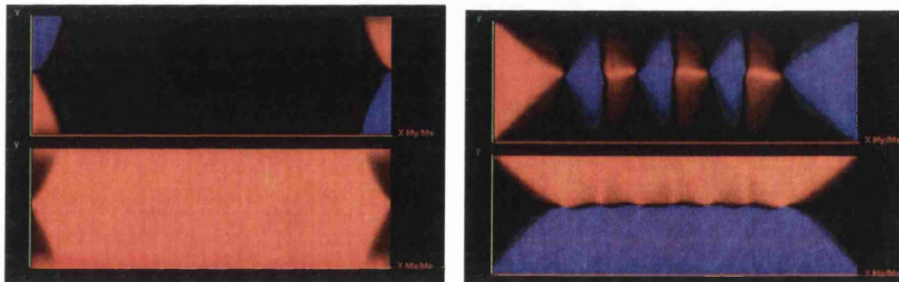


Figure 5.23: LLG simulation of $1500 \times 500 \times 50$ nm Co element.

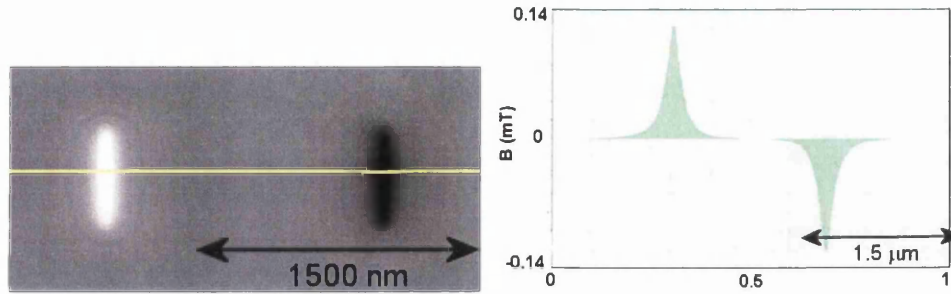


Figure 5.24: Image of stray field from single domain magnetised Co element and accompanying line scan. Element dimensions $1500 \times 500 \times 50$ nm.



Figure 5.25: Schematic of stray field arising from element with raised ends. It can be seen that less flux enters the area underneath the end of the element and therefore less flux passes through the Hall cross.

cross.

Two possible explanations for the discrepancy are that the Hall cross defined in the 2DEG was larger than expected and that the ends of the element were not completely parallel to the substrate surface. During lift-off, it is common for materials evaporated onto the surface in the holes in the resist to partially lift-off due to adhesion problems between the material and GaAs substrate. The Co layer does not have a seed layer to ensure good adhesion and could therefore have partly lifted off. Fig 5.25 shows a sketch of the stray field which would arise from an element with raised ends. To confirm this picture, a SEM image could be taken at an angle to the specimen plane and the simulation system could be modified to consider this. Due to time constraints, it was not possible to attempt this.

Also of interest was the longitudinal measurement cycle where structure due to the magnetic element was observed, Fig 5.21(b). Due to the cross coupling of signals, the longitudinal signal also contained a fraction of the Hall component from the element, see section 5.4.3 below. This gave the observed hysteresis loop in the longitudinal measurement.

Fig 5.26 shows results from reversing the current and voltage contacts. Here the current is through 3/5 with the voltages being measured over 1/6 (1/4). The transverse measurement here, is taken over the length of the element. However, one end of the element is outwith the narrow constriction of the gated Hall bar. The measurements have been transformed to remove the gradient due to the slight misalignment. It can be observed that this measurement is similar to the transverse measurement in Fig 5.22 with the orientation of the hysteresis loop reversed. The step in the hysteresis loop measured here is 3Ω as found previously with the conventional current/voltage contact arrangement. This helps confirm the step is due to the magnetic element and that the measured mean flux density through the Hall cross is $\sim \pm 0.8$ mT.

5.4.3 $1500 \times 500 \times 50$ nm Co element in the centre of the Hall bar

A $1500 \times 500 \times 50$ nm Co element was evaporated such that the centre of the element was aligned at the centre of the Hall bar, Fig 5.27. The bulk carrier concentration and mobility were; $n = 2.7 \times 10^{15} \text{ m}^{-2}$ and $\mu = 26 \text{ m}^2 \text{ V}^{-1} \text{ s}^{-1}$. In this specimen, a contact problem was observed with pin 4. This led to the set of measurements, both longitudinal and transverse, which used this contact having considerably more noise than the measurements from the second set of contacts. The level of noise was such no magnetic information could be obtained from measurements using contact 4.

As discussed previously, the transverse measurement changed with applied

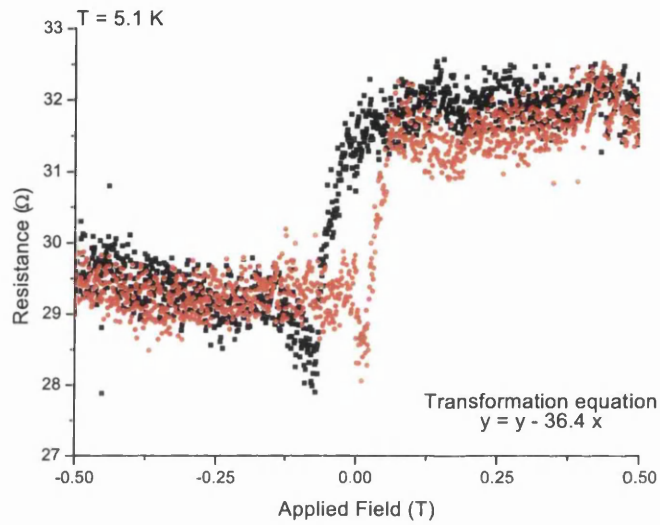


Figure 5.26: Measurements with I and V reversed. $1500 \times 500 \times 50$ nm cobalt element with one end of the element over a Hall cross.

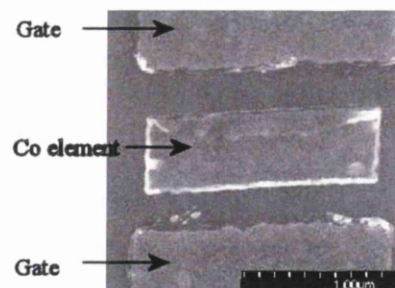


Figure 5.27: SEM image of specimen

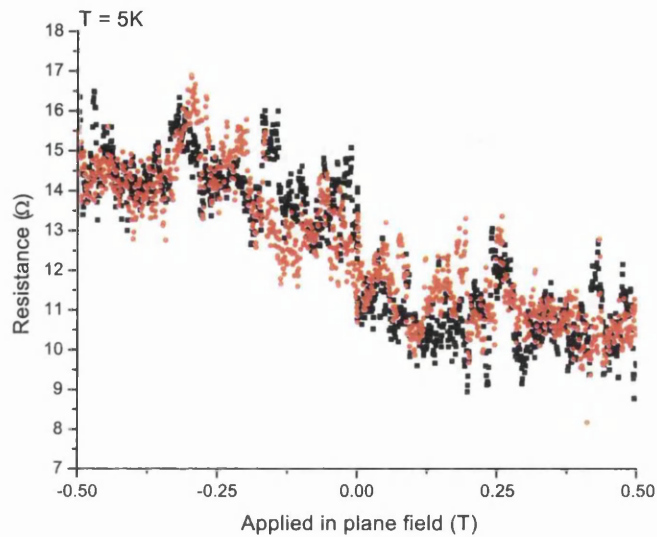
gate voltage. In this specimen, the Hall measurement varied between positive and negative as the applied gate voltage was increased. Two separate measurements at $V_g = -0.15$ V and $V_g = -0.25$ V were obtained. Both had a positive transverse resistance. Fig 5.28 shows the transverse measurement for an in plane field using contacts 3/5 for the two different applied gate voltages. As with the previous specimen, a change in resistance of $\simeq 3 \Omega$ was measured in the hysteresis loop for a gate voltage of -0.15 V. This was the applied gate voltage chosen for good gate definition. Increasing the gate voltage to -0.25 V increased the constriction in the Hall bar and therefore the mean flux density through the Hall cross increased. This is observed in the measurement as a significantly larger step in the transverse measurement.

For the standard applied gate voltage of -0.15 V, the simulations carried out in the previous section would also be roughly applicable as the end of the magnetic element is very close to the Hall cross. Again, the calculated flux density through the Hall cross is greater than the measured flux density as discussed previously.

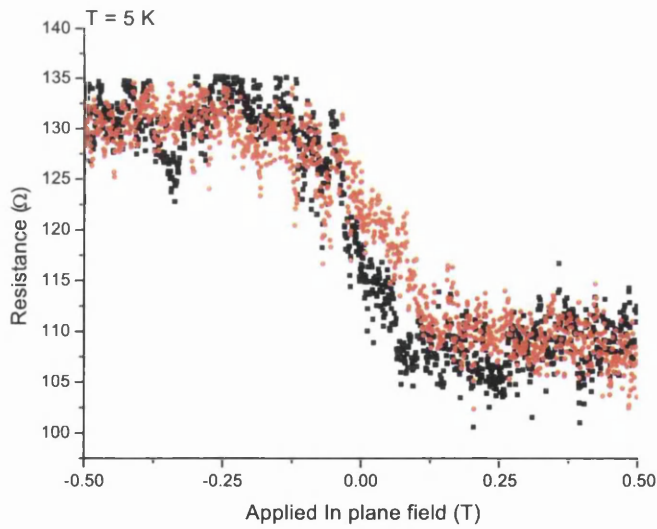
A rough estimate of the area of the Hall cross with the applied gate voltage of -0.25 V can be obtained by considering the size of the step in the measurement. The step gives a flux density through the Hall cross of $B = 0.01$ T using equation 5.8. Combining this with equation 5.9, the area can be calculated by dividing one by the other. This gave a Hall cross area of $A = 2 \times 10^{-13} \text{ m}^2$. One possible set of dimensions for the Hall cross could therefore be $250 \text{ nm} \times 0.9 \mu\text{m}$.

5.4.4 $1000 \times 500 \times 50$ nm Co element in the centre of the Hall bar

A $1000 \times 500 \times 50$ nm Co element was evaporated such that the centre of the element was aligned with the centre of the Hall bar. SEM images



(a) Transverse measurement at $V_g = -0.15\text{ V}$



(b) Transverse measurement at $V_g = -0.25\text{ V}$

Figure 5.28: Hall measurements at differing applied gate voltages. $I = 1/2$, $V = 3/5$. $1500 \times 500 \times 50\text{ nm}$ cobalt element in the centre of the Hall bar.

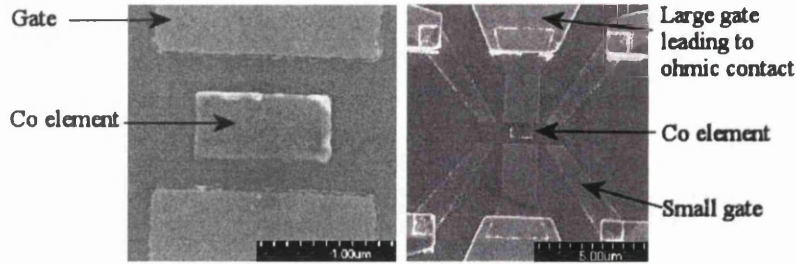


Figure 5.29: SEM image of specimen

of the element and the small gated Hall bar are shown in Fig 5.29. Bulk substrate measurements gave a carrier concentration of $n = 3.1 \times 10^{15} \text{ m}^{-2}$ and a mobility of $\mu = 48 \text{ m}^2 \text{ V}^{-1} \text{ s}^{-1}$. With an applied field perpendicular to the plane of the specimen and the small Hall bar defined in the 2DEG, mesoscopic effects were observed in the longitudinal measurement as expected.

Longitudinal and transverse measurements from both sides of the Hall bar, in an in-plane field, are shown in Fig 5.30. A clear step in resistance and a hysteresis loop can be observed in all cases. The difference in the resistance of the two measurements is due to gate b, between current contact 1 and voltage probe 5 being badly defined leading to a high resistance state. Although the resistance is different, the loop observed in all four measurements occurs at the same fields. The two Hall resistance measurements ($(V_3 - V_5)$ and $(V_4 - V_6)$) independently showed hysteresis loops of opposite sign. The sense of the loop is reversed in the two graphs as the measurements are taken at different ends of the magnetic element. One Hall measurements will be affected by flux out of the element whereas the other will be affected by flux into the element.

Similar investigations using a 2D array of elements have been carried out by McMullen et al [105]. McMullen calculated the longitudinal and transverse, sum and difference signals and showed that for a perfectly symmetric system, the summed signals should show no variation in resistance with applied field. Also, the longitudinal difference voltage, $(V_3 - V_4) - (V_5 - V_6)$, can

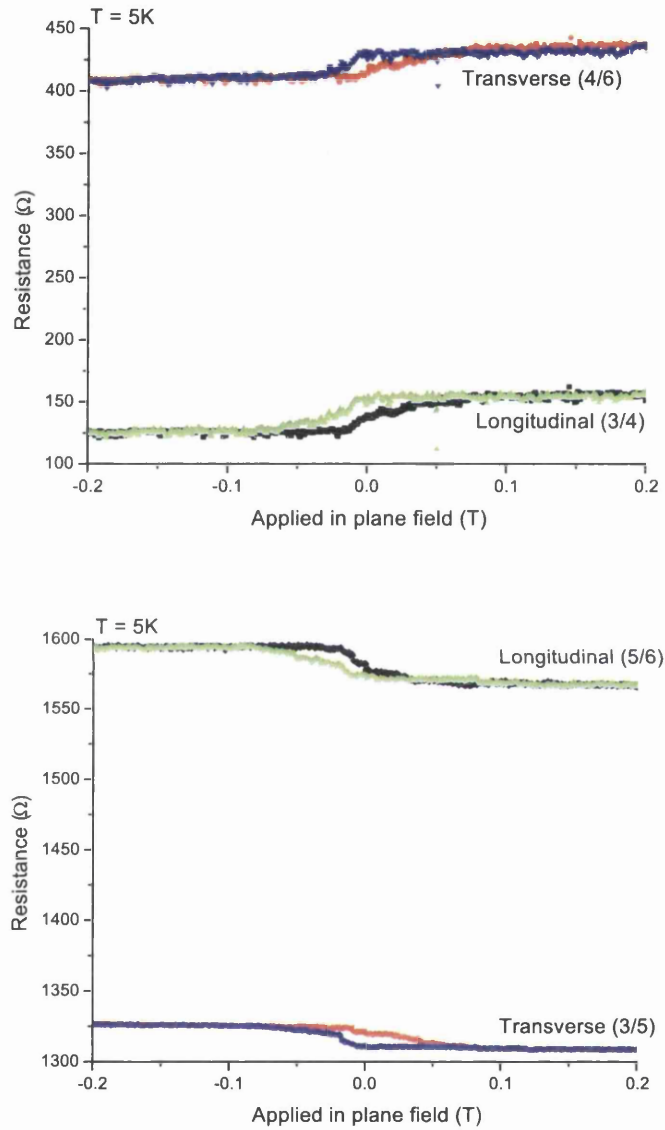


Figure 5.30: Traces of longitudinal and transverse at parallel applied field. $1000 \times 500 \times 50$ nm cobalt element in the centre of the Hall bar.

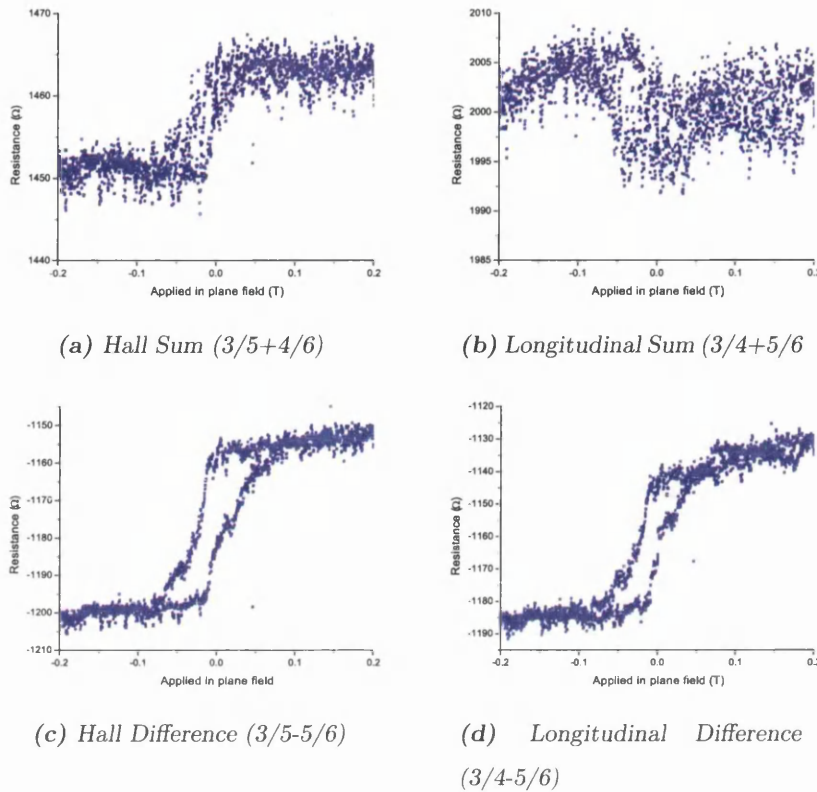


Figure 5.31: Sum and Difference traces of longitudinal and transverse at parallel applied field. $1000 \times 500 \times 50$ nm cobalt element in the centre of the Hall bar.

be re-written as $(V_3 - V_5) - (V_4 - V_6)$. This is equal to the difference in Hall voltages, $(V_3 - V_5)$ and $(V_4 - V_6)$, over the two Hall crosses. Therefore, the Hall and longitudinal difference signals would be identical.

The analysis applied to the 2D array of elements is also applicable here as the element lies in the centre of the Hall cross. Figs 5.31a and 5.31b show the transverse and longitudinal summed signals. The change in measured resistance observed in both graphs indicate that the system is not fully balanced. This could arise from differences in gate definition voltages giving two Hall crosses with a slightly different size or a small misalignment of the element with respect to the two Hall crosses.

The difference voltages are shown in Figs 5.31c and 5.31d. Only two of the possible four difference signals are shown; the other two are identical but with opposite sense, similar to taking measurement on opposite sides of the Hall bar as discussed previously. Some small differences are observed, the reasons for which were discussed above. The shapes however, are the same within experimental error.

The shape of the hysteresis loop, has been observed previously [106, 107] and represents the formation of domains, with favourably aligned domains growing before an irreversible change. Further domain processes occur as the magnetisation aligns fully with the applied field. The shape of the hysteresis loop is similar to that obtained from simulating the reversal of a $1000 \times 500 \times 50$ nm Co element using LLG, Fig 5.32. When compared with the experimentally observed loops, it can be seen that the fields at which the element reverses do not match perfectly. The likely cause of this discrepancy is that the anisotropy used in the the simulation did not match that of the real element due to grains in the elements giving fluctuations in the anisotropy and therefore affecting the reversal fields.

Fig 5.33 shows the stray field arising from a $1000 \times 500 \times 50$ nm Co element and a line scan across the centre of the element. Using the same technique discussed in section 5.4.2, the flux through the Hall cross was calculated to be 27 mT. The measured flux through the Hall cross was $\simeq 20$ mT. These two values are in much better agreement with one another than found previously. One explanation for this is that the element was in the centre of the Hall bar, with all contacts working, which enabled a full characterisation and measurement of the effects at both sides of the Hall bar.

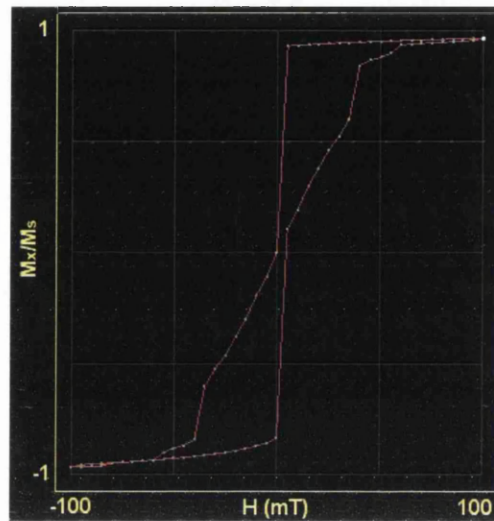


Figure 5.32: Simulated hysteresis loop for $1000 \times 500 \times 50$ nm Co element

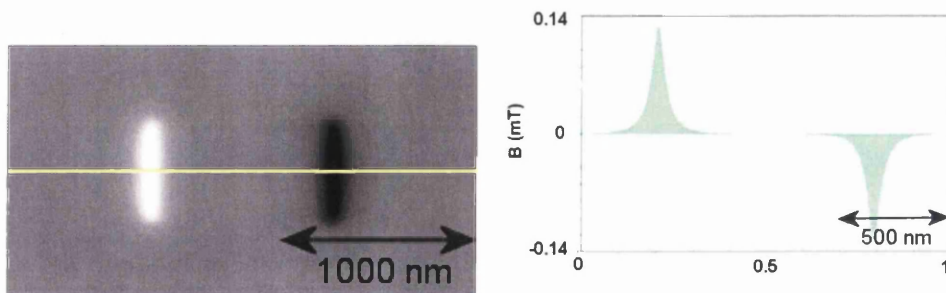


Figure 5.33: Simulated hysteresis loop, image of stray field from single domain magnetised Co element and accompanying line scan. Element dimensions $1000 \times 500 \times 50$ nm.

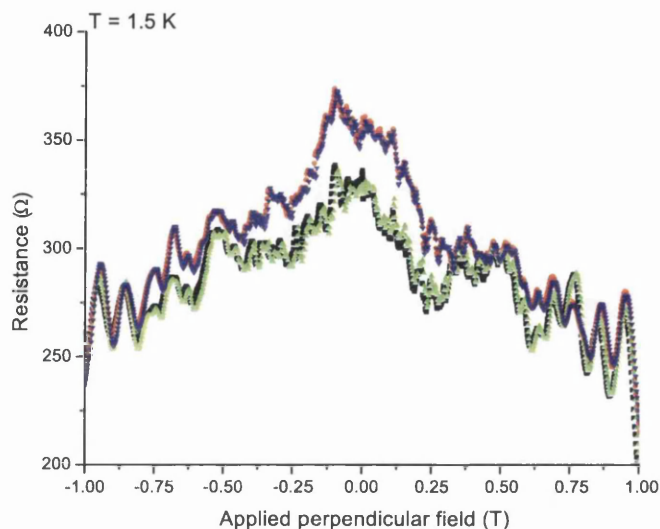


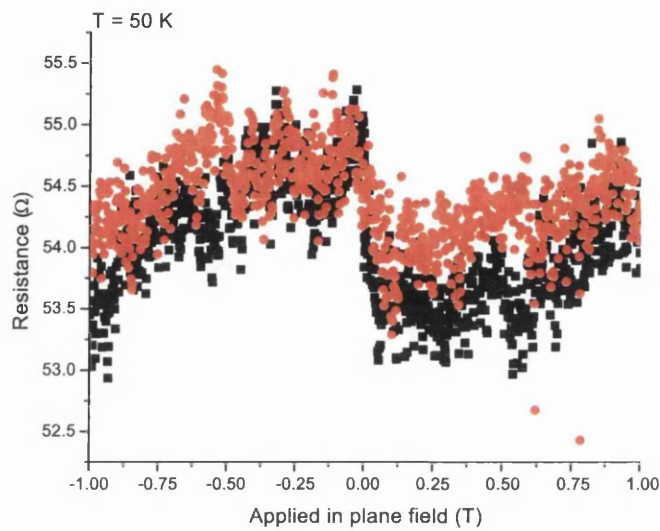
Figure 5.34: Longitudinal measurement with applied field perpendicular to specimen plane

5.4.5 $1500 \times 500 \times 20$ nm Py element with one end over a Hall cross

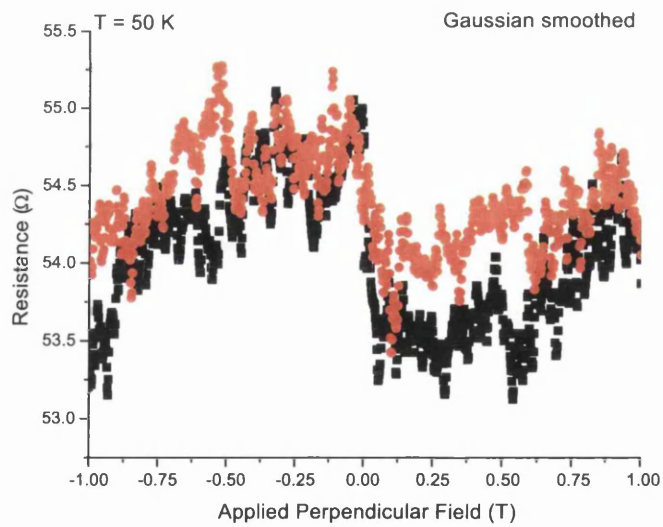
A $1500 \times 500 \times 20$ nm permalloy element was evaporated such that one end of the element lay over a Hall cross. As with previous experiments, the bulk transport properties of the substrate were investigated. For this specimen, the carrier concentration was $n = 3.4 \times 10^{15} \text{ m}^{-2}$ and the mobility $\mu = 22 \text{ m}^2 \text{ V}^{-1} \text{ s}^{-1}$.

The longitudinal measurement, for both sides of the Hall bar is shown in Fig 5.34. The field in this case was applied perpendicular to the plane of the specimen. From this, it can be seen that the mesoscopic effects observed in the basic Hall bars and those with cobalt elements are also observed when a permalloy element is evaporated onto the surface of the substrate as expected.

The transverse measurement with the field applied in the plane of the specimen is shown in Fig 5.35a. Due to the magnetic element being permalloy



(a) original data



(b) smoothed 3 times

Figure 5.35: Transverse measurement showing unclear small step in transverse measurement. Second fig shows same data but smoothed three times.

rather than cobalt and the reduction in element thickness, it was expected that any effects due to the magnetic element would be smaller. This meant that at low temperatures, it was considerably more difficult to observe a step in the hysteresis loop as the expected step was comparable to the noise level. To reduce the mesoscopic resistance fluctuations, the specimen was warmed to 50 K and the measurements were obtained at this temperature. From Fig 5.35, the step in the transverse measurement is $\sim 1 \Omega$. Using the method described in section 5.4.2, this gives a flux density through the Hall cross of 0.5 mT.

Although the data taken shows a step in the hysteresis loop, it is not as clear as the steps observed for the cobalt elements. To help reduce some of the noise, the data was gaussian smoothed. That is, every data point is transformed using

$$\delta n' = \frac{\delta n}{2} + \frac{\delta n + 1}{4} + \frac{\delta n - 1}{4} \quad (5.13)$$

where δn is the signal point n in a particular generation and $\delta n'$ the smoothed values which replaces it. Fig 5.35b shows the smoothed measurements after 3 cycles of Gaussian smoothing. This helps make it easier to observe that the step in the transverse measurement is $\sim 1 \Omega$ and also, that the field at which the magnetic element reverses is $\sim \pm 0.07$ T.

LLG simulations were carried out on a magnetic element of the same dimensions as the one investigated experimentally. The hysteresis loop and stray fields were calculated using the techniques described in section 5.4.2. Fig 5.36 shows the simulated hysteresis loop. The fields at which the simulation reversed are similar but do not match those of the element investigated experimentally. This could be due to a difference in the anisotropy between simulated and experimental results as discussed previously. Also, as for the Co elements, the stray field through the Hall cross was calculated and as previously, was considerably larger than the experimental value.

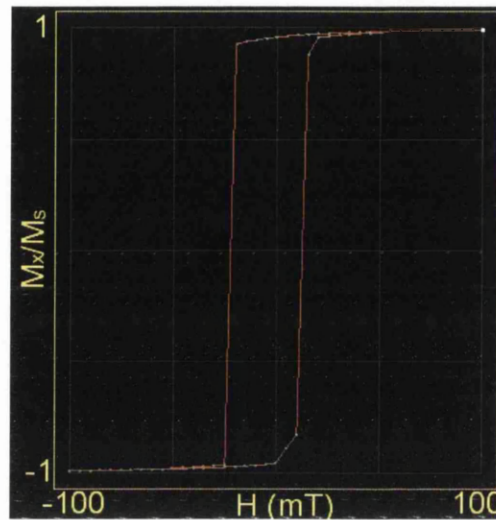


Figure 5.36: Simulated hysteresis loop for $1 \times 0.5 \mu\text{m} \times 20 \text{ nm}$ permalloy element

5.5 Conclusions

It has been shown that small gated Hall bars could be fabricated onto the surface of a semiconductor specimen on top of a larger etched Hall bar. This enables the characterisation of the bulk transport properties alongside measurements related to the small Hall bar. In particular, it confirmed that the high field transport properties of the systems investigated did not change markedly with Hall bar size, and that the carrier concentration and mobility remained constant. At low fields, the small gated Hall bar showed additional effects to those observed in the large Hall bar. These mesoscopic effects were attributed to diffuse boundary scattering.

Further to this, magnetic elements were evaporated near the centre of the gated Hall bar to investigate the interactions between the stray field from the element and electrons in the 2DEG. The mesoscopic effects observed in the basic system were also observed in perpendicular applied field with a magnetic element present. With an in-plane external field, an additional effect was observed due to the stray field from the magnetic element. This effect gave a

measurable change in the Hall resistance. The magnitude of the Hall signal due to stray field from the magnetic element was measured experimentally and also calculated. Discrepancies between the two values were measured in many samples. This is currently attributed to partial lift-off of the element leading to a reduction of flux through the Hall cross.

For an element placed symmetrically between the two Hall contacts, in the centre of the Hall bar, both longitudinal and transverse resistance measurements exhibited structure due to the magnetic element when an in-plane field was applied. The relationship between the two measurements was described by a simple model which was used to discuss the data. Again, the magnitude of the Hall signal due to the stray field was measured experimentally and also calculated. In this case, good agreement between the two values was obtained. The shape of the hysteresis loop was in good agreement between the simulation and experimental results and was explained by domain processes effecting the reversal.

Chapter 6

Conclusions and Future Work

6.1 Introduction

The work presented in this thesis has investigated properties of selected single and multilayer magnetic materials. Lorentz microscopy was carried out on AAF biased SVs, both as thin films and elements, to study their micromagnetic properties. Alongside this, quantum transport measurements of hybrid semiconductor/magnetic structures gave an insight into the interactions between the stray field from magnetic elements and conduction in the 2DEG. For some of the AAF biased SV elements, simulations were carried out to aid interpretation of the results.

This chapter discusses the principal findings from the different investigations and conclusions drawn from the studies. Following this, is a discussion of some of the possible future investigations which could extend the work carried out here.

6.2 Conclusions

6.2.1 Artificial antiferromagnetically biased spin valves

The free layer reversal mechanisms of a range of thin film AAF biased SVs were investigated in Chapter 3. Fresnel imaging showed that the reversal mechanisms varied markedly with the thickness of the second Co layer in the AAF.

It had been expected that this would occur and that three different regimes would be observed. For the AAF biased SVs where the second Co layer of the AAF was thinner than the first, it was expected that the system would behave in a manner similar to that of a conventional SV and possess moderate GMR. As the thickness of the second Co layer approached that of the first, both layers would compete to lie parallel with the growth field direction creating a complex domain structure in the AAF. This would become pinned, leading to the observation of complex domain structures and a low GMR. For a system where the second Co layer of the AAF was thicker than the first, the orientation of the AAF would reverse so that the second layer would lie parallel to the applied field direction. Again, due to the imbalance in thickness of the two layers, the system would behave like a conventional SV and have a corresponding GMR.

For the series of spin valves investigated, changes in magnetic reversal mechanisms and the magnitude of the GMR with the thickness of the second Co layer in the AAF were observed. The spin valve studied with the second Co layer significantly thinner than the first acted in a manner consistent with conventional SVs, with easily understood behaviour. Also, the system with the second Co layer notably thicker than the first behaved as anticipated. However, the specimens studied where the two Co layers were thought to be comparable or with the second slightly thicker than the first did not exhibit the anticipated reversal properties. Further investigation indicated that an

anomaly during growth had led to the second Co layer of the AAF being approximately 70% of the expected thickness. This explained the unexpected results. Specimens where the two Co layers were thought to be approximately equal were in fact unbalanced and the specimen where the second Co layer was thought to be slightly thicker than the first had both Co layers approximately equal. In light of the new information, the predicted behaviour of the system and the experimental results were in good agreement.

For use in applications, elements rather than continuous films are of interest and two of the AAF structures were chosen for further investigation in Chapter 4. Edge field coupling from the elements interacted with the interlayer coupling affecting the offset in the hysteresis loop. In one case, the thickness of the second Co layer was $\sim 70\%$ that of the first whilst for the other specimen it was $\sim 12\%$ and possibly a discontinuous film.

DPC images of the magnetisation reversal showed that they were dependent on the orientation of the long axis with respect to the growth and applied field directions. However, for the elements investigated, one particular magnetic configuration was observed in a number of the elements. This consisted of a number of large, central domains effecting the reversal, leaving edge domains which were eliminated as the applied field increased in magnitude.

The offset in the hysteresis loop was similar for elements of the same shape and size but different orientation. This had been expected for elements with the same layer structure and growth conditions. The offset did however differ between the two specimens with different layer structures. Also, in the elliptical elements, the lack of domain nucleation and wall location points due to corners, led to lower reversal fields and offsets in the hysteresis loop.

As introduced above, in the specimen where the second Co layer is significantly thinner than that of the first, it is not known whether the second Co layer was a continuous film. An incomplete layer could explain some of the results observed in this specimen.

6.2.2 Hybrid ferromagnet/semiconductor heterostructures

A hybrid ferromagnetic/semiconductor system was investigated in Chapter 5. It was shown that small gated Hall bars can be successfully used in conjunction with a larger etched Hall bar to enable bulk characterisation of the material alongside measurements on a smaller scale. Both large and small Hall bars showed similar high field magnetotransport properties but at low field, the smaller Hall bar shows additional mesoscopic effects attributed to diffuse boundary scattering.

With the magnetic element present, the above effects persisted in perpendicular applied field. With an in-plane field, an additional effect was observed where the stray field from the magnetic elements gave a measurable changes in the Hall resistance. The magnitude of the Hall signal due to stray field from the element was measured experimentally and also calculated. It was shown that discrepancies between the two values existed in many samples. Currently, this is attributed to partial lift-off of the element leading to a curled state and reduced flux through the Hall cross.

For an element placed in the centre of a Hall bar, symmetrically between the two Hall contacts, both longitudinal and transverse resistance measurements showed structure due to the magnetic element in an in plane applied field. The relationship between the two measurements has been described by a simple model which was used to discuss the data. For this sample, both the shape of the hysteresis loop and the magnitudes of the resistance structures were in good agreement with theoretical estimates.

6.3 Future Work

6.3.1 Artificial antiferromagnetically biased spin valves

The work presented on the free layer reversal of AAF biased thin film SVs concentrated on the applied field aligned parallel to the growth field direction. Only a small section related to the field applied at an angle (θ) with respect to the growth field. The results obtained from measurements with the applied field at an angle to the growth field showed that the reversal mechanism significantly altered as θ increased. Reversals became asymmetric and were dependent on whether the field was rotated clockwise or anticlockwise from the preferred direction of magnetisation.

Previous work had been undertaken simulating the change in the reversal mechanism as the applied field rotated from the preferred direction of magnetisation using a modified Stoner-Wohlfarth model. Developing the current research by investigating the dependence of the reversal mechanism on θ alongside the simulations to gain a better understanding of the coupling between the layers and anisotropy within the system. This could lead to possible modifications of the AAF system to render it more suitable for applications such as MRAM where two distinct magnetisation states with a fast reversal between them are desirable or a sensor where a smooth rotation of the magnetisation is more favourable.

The AAF biased SV specimens incorporated an IrMn antiferromagnetic biasing layer. The IrMn was chosen as it has a high blocking temperature which is necessary for applications. A number of applications in which SV's are used experience operating temperatures significantly higher than room temperature. It would therefore be interesting to investigate the temperature dependence of the SV systems. Both the GMR, using a four probe CIP arrangement, and the reversal properties, using a heating rod in the TEM, could be studied to gain a comprehensive insight into the suitability of these materials for high

temperature operation.

Due to limitations of time and difficulties in observing magnetic contrast, it was not possible to fully characterise the range of SV elements. As smaller elements are of greater interest, it is desirable that a method of enhancing magnetic contrast from the elements is found. Improvements in the fabrication process to minimise edge flags should be considered. Also, other methods of observing the reversal, such as MOKE could be used in conjunction with the TEM to aid characterisation of larger elements.

Finally, the specimens investigated in this thesis did not possess the expected layer structures. It would be interesting to investigate specimens where the layer structure was closer to that expected and enable a study of a fully balanced AAF and also to adjust the layer structure so that the hysteresis loop centered around zero field.

6.3.2 Hybrid ferromagnet/semiconductor heterostructures

The work presented on the hybrid ferromagnetic/semiconductor systems highlighted some of the technical difficulties in fabricating complex multi-layer systems. Lift-off and adhesion problems reduced the quality and yield of a specimen batch. It would therefore be beneficial to study the fabrication process to determine where improvements could be made. Alongside this, it would be desirable to develop a process to enable the patterning of a Hall bar using dry etch. This would offer a more uniform Hall bar with known Hall bar dimensions and should help reduce noise within the system. As part of the development, a study into the feasibility of reducing the dimensions of the Hall cross could be undertaken.

Following improvement to the Hall bar structure, it would be interesting to study a wider range of ferromagnetic elements. Co is a relatively easy material

to study; further investigations on thinner layers of Co and continuation of the study into NiFe would help determine possible measurement limits. This would act as a base from which more complex ferromagnetic systems such as the AAF biased SVs could be investigated.

As part of the investigations into the limits of measurement, it could also be useful to consider the shape, position and size of the elements with respect to the Hall bar to maximise the stray field from the element through the Hall cross.

Appendix A

Appendix A

A.1 Introduction

This appendix describes the fabrication of hybrid ferromagnetic/semiconductor heterostructures. Each step in the fabrication of the Hall bars is described. Following this, the deposition of the magnetic elements is reported.

A.2 Fabrication process

A.2.1 Wafer Cleaning

<i>process</i>	<i>action</i>	<i>timing</i>
cleaning	acetone and ultrasonic bath	5 minutes
	IPA and ultrasonic bath	5 minutes
	dry in nitrogen	

Wafer cleaning, as discussed in section 2.6, was vital to the fabrication process as contamination damaged specimens, often to the extent where the specimen was unusable. Wafer cleaning removed contamination and was carried out before commencing fabrication of a new sample, and as required during the fabrication process.

A.2.2 Alignment Marks

<i>process</i>	<i>action</i>	<i>timing</i>
depositing resist	spin 15 % 2010 resist at 5000rpm	60 s
	bake at 180 °C	30 minutes
	spin 4 % 2041 resist at 5000rpm	60 s
	bake at 180 °C	60 minutes
transfer of pattern	pattern transferred from WAM to CATS	
	Job file submitted	
	submit job to beamwriter	
	dose 280 μ C, spot size 160 nm	1 night
develop	1 : 1, MIBK : IPA warmed to 21 °C	60 s
	rinse in IPA	30 s
	dry in nitrogen	
de-oxidisation etch	20 : 1 H ₂ O : HCl	20 s
	rinse H ₂ O	20 s
	dry in nitrogen	
metallise	evaporate 33 nm Ti, 160 nm Au	30 minutes
lift-off	acetone and heatbath	~ 20 minutes
	rinse in IPA	30 s
	dry in nitrogen	

The set of four alignment marks had dimensions of $30\ \mu\text{m} \times 30\ \mu\text{m}$ with a spacing of $150\ \mu\text{m}$ between bottom left corners. The alignment process during subsequent layers exposed the alignment mark used for that layer. This led to the mark in use being damaged, for example, during the evaporation of ohmic contacts, the alignment mark used will also have the ohmic materials evaporated onto the exposed area making the reference corner less well defined. It is not possible to prevent this so a set of four alignment markers were used, when the first was damaged, the reference distances were altered to use the

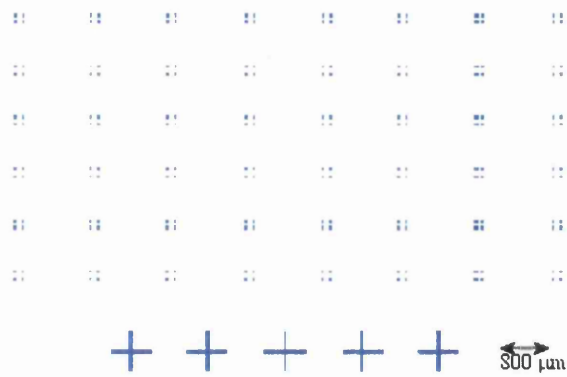


Figure A.1: CATS image of alignment file to enable the fabrication of 35 specimens

second alignment mark and so on.

Multiple specimens were fabricated on a large section of substrate and the specimen spacing was $1.5 \text{ mm} \times 1 \text{ mm}$. This enabled each specimen to have four sets of alignment marks, one at each corner. This gave an advantage in aligning the specimen accurately as all four sets could be used to determine the position and any rotation of the specimen. Fig A.1 shows the CATS image of the complete alignment mark file.

A.2.3 Ohmics

<i>process</i>	<i>action</i>	<i>timing</i>
depositing resist	spin 15 % 2010 resist at 5000rpm	60 s
	bake at 180 °C	30 minutes
	spin 4 % 2041 resist at 5000rpm	60 s
	bake at 180 °C	60 minutes
transfer of pattern	pattern transferred from WAM to CATS Job file submitted submit job to beamwriter dose 280 μ C, spot size 160 nm	1 night
develop	1 : 1, MIBK : IPA warmed to 21 °C	60 s
	rinse in IPA	30 s
	dry in nitrogen	
de-oxidisation etch	20 : 1, H ₂ O : HCl	20 s
	rinse H ₂ O	20 s
	dry in nitrogen	
metallise	8 nm Ni, 120 nm Ge, 130nm Au, 80 nm Ni, 250 nm Au	45 minutes
lift-off	acetone and heatbath	~ 25 minutes
	rinse in IPA	30 s
	dry in nitrogen	
annealing	heat from ambient temperature to 360 °C	10 s
	raise from 360 °C to 380 °C	10 s
	anneal at 380 °C	40 s
	cool to ambient temperature	2 minutes

Fig A.2 shows the CATS pattern used for the ohmic contacts. The ohmic contacts had dimensions of $150 \mu\text{m} \times 150 \mu\text{m}$ with a spacing of $100 \mu\text{m}$ between contacts. Ohmic contacts have been labelled to indicate which contacts

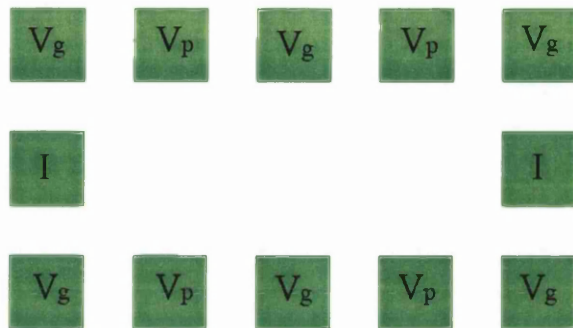


Figure A.2: CATS images of ohmics. I represents current contacts, V_p voltage probes and V_g gate contacts

traditionally current contacts, voltage probes or gate contacts.

As shown in the table, after lift-off, the wafer section is annealed. This involves heating of the specimen to allow the diffusion of germanium atoms through the metallised stack into the GaAs/AlGaAs semiconductor. These atoms form a current path between the ohmic contact and the 2DEG. Different semiconductors and 2DEG depths require different annealing conditions. The conditions shown above chosen after a series of tests which varied the annealing temperature and time.

After cooling, the room temperature resistance of the wafer is checked using a probe system. For a good specimen, the resistance between ohmic contacts should be less than $1\text{ k}\Omega$. If the resistance is significantly higher, this can mean that when cooled, the specimen may fail. Frequently, a single Hall bar will be cleaved and tested in the low temperature system to confirm the quality of the annealing process and the viability of the wafer segment. It is possible to re-anneal at this point, although this process has limited success.

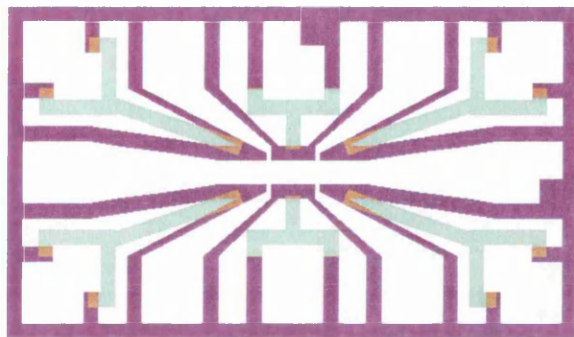


Figure A.3: CATS image of the isolation

A.2.4 Isolation

<i>process</i>	<i>action</i>	<i>timing</i>
depositing resist	spin 15 % 2010 resist at 5000rpm	60 s
	bake at 180 °C	60 minutes
transfer of pattern	pattern transferred from WAM to CATS	
	Job file submitted	
	submit job to beamwriter	
	dose 280 μC , spot size 160 nm	1 night
develop	1 : 1, MIBK : IPA warmed to 21 °C	60 s
	rinse in IPA	30 s
	dry in nitrogen	
isolation etch	100 : 2 : 1, H_2O : H_2O_2 : H_2SO_4	30 s
	rinse H_2O	20 s
	dry in nitrogen	

Fig A.3 shows the pattern file for the isolation. After completion of the etch, the resistance between ohmic contacts is again checked. This gives an indication of whether the etch has reached depth of the 2DEG. In a successful etch, the resistance between ohmic contacts should be less than 1 k Ω for contacts with a current path between them and considerably greater than 1 M Ω

when there is no current path available.

If the isolation etch did not reach the 2DEG, the etch can be repeated for a further 5 s and then re-checked. Once completed, the resist layer is removed by a 5 minute soak in acetone, 30 s rinse in IPA then dried using a fast flow of nitrogen.

The isolation etch defines the large Hall bar into the 2DEG. It also isolates the specimen from other specimens on the same piece of wafer. Each ohmic also has isolation round either three or four sides of the contact depending on whether it is to be used for current/voltage or for a gate. For a current or voltage contact, the side without isolation leads to the Hall bar. The other three sides are isolated to prevent unwanted current flow. For a gate, the ohmic needs to be electrically isolated from the Hall bar, hence isolation on all sides of the contact. Also, for the gate ohmics, there is a small area between the isolation and the contact on one side. This is to prevent cracks in the gates by having a stepped drop from the ohmic to the isolated gate track.

A.2.5 Small Gates

<i>process</i>	<i>action</i>	<i>timing</i>
depositing resist	spin 4 % 2010 resist at 5000rpm	60 s
	bake at 180 °C	30 minutes
	spin 2.5 % 2041 resist at 5000rpm	60 s
	bake at 180°C	60 minutes
transfer of pattern	pattern transferred from WAM to CATS	
	Job file submitted	
	submit job to beamwriter	
	dose 312 μC , spot size 15 nm	1 night
develop	2.5 : 1, MIBK : IPA warmed to 21 °C	60 s
	rinse in IPA	30 s
	dry in nitrogen	
de-oxidisation etch	20 : 1, H ₂ O : HCl	20 s
	rinse H ₂ O	20 s
	dry in nitrogen	
metallise	evaporate 12 nm Ti, 15 nm Au	15 minutes
lift-off	acetone and heatbath	~ 30 minutes
	rinse in IPA	30 s
	dry in nitrogen	

To establish the correct dose to expose the pattern, a series of exposure tests are carried out. The pattern file used is shown in Fig A.4 and results of one such test is shown below in Fig A.5.

From this, it can be seen that a dose of approximately 312 μC was suitable for the pattern required. Further investigation of the exposure test around this dose gave the exact dose required. Fig A.6a shows that a dose of 250 μC defined the gates well but did not give the desired voltage probe dimension of 300 nm. A dose of 312 μC (Fig A.6b) showed that the gates were well defined

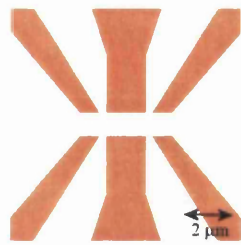


Figure A.4: CATS image of the small gates

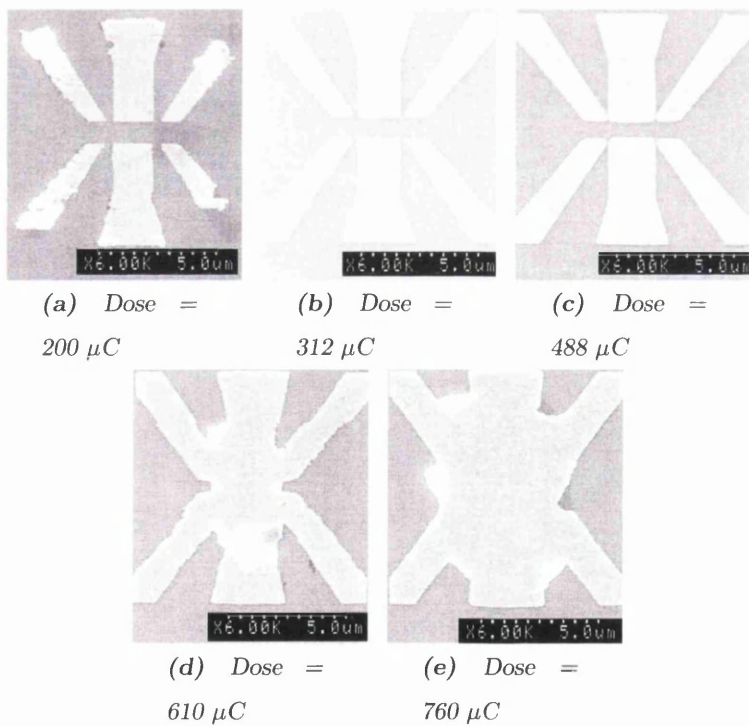


Figure A.5: SEM images of small Hall bar exposure dose test

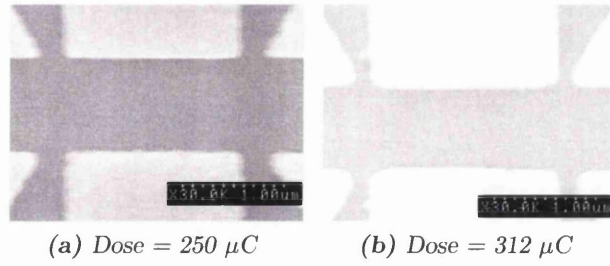


Figure A.6: Higher magnification SEM images of small Hall bar exposure dose test

and that the desired voltage probe dimension of 300 nm was transferred from pattern to substrate accurately. It was this dose which was used to fabricate the small Hall bars.

A.2.6 Thick gate leads

<i>process</i>	<i>action</i>	<i>timing</i>
depositing resist	spin 15 % 2010 resist at 5000rpm	60 s
	bake at 180 °C	30 minutes
	spin 4 % 2041 resist at 5000rpm	60 s
	bake at 180 °C	60 minutes
transfer of pattern	pattern transferred from WAM to CATS Job file submitted submit job to beamwriter dose 280 μ C, spot size 160 nm	1 night
develop	1 : 1, MIBK : IPA warmed to 21 °C	60 s
	rinse in IPA	30 s
	dry in nitrogen	
de-oxidisation etch	20 : 1, H ₂ O : HCl	20 s
	rinse H ₂ O	20 s
	dry in nitrogen	
metallise	evaporate 33 nm Ti, 160 nm Au	30 minutes
lift-off	acetone and heatbath	~ 20 minutes
	rinse in IPA	30 s
	dry in nitrogen	

The large gates, Fig A.7, linked the gate ohmics to the small Hall bar at the centre of the design by an overlap of 2 μ m to provide current continuity between the ohmic contacts and the centre of the Hall bar. The thick gates were used in conjunction with the small gates and the thicker gates are less likely to be discontinuous over a larger distance. The small gates are required at the centre of the Hall bar to achieve the desired definition.

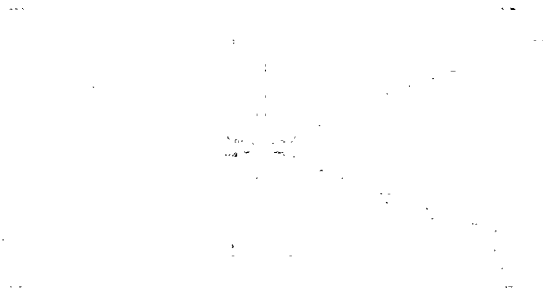


Figure A.7: CATS image of the thick leads to the gates

A.2.7 Magnetic structures

<i>process</i>	<i>action</i>	<i>timing</i>
depositing resist	spin 4 % 2010 resist at 5000rpm	60 s
	bake at 180 °C	30 minutes
	spin 2.5 % 2041 resist at 5000rpm	60 s
	bake at 180 °C	60 minutes
pattern transfer	pattern transferred from WAM to CATS Job file submitted submit job to beamwriter dose 312 μC , spot size 15 nm	1 night
develop	1: 1, MIBK : IPA warmed to 21 °C	60 s
	rinse in IPA	30 s
	dry in nitrogen	
de-oxidisation etch	20:1, H ₂ O : HCl	20 s
	rinse H ₂ O	20 s
	dry in nitrogen	
metallise	evaporate 60 nm Co	3 hours
lift-off	acetone and heatbath	~ 30 minutes
	rinse in IPA	30 s
	dry in nitrogen	

Magnetic structures were evaporated onto the surface of the GaAs substrate using the thermal evaporator in the Department of Physics and Astronomy. Metallisation times for the magnetic structures are considerably longer than those for other layers. This is due to the use of different evaporator for the magnetic layer.

Dose tests similar to those for the small Hall bar were also carried out for the magnetic layer. The test gave a dose of $312 \mu\text{C}$ defining the magnetic structure most accurately.

Bibliography

- [1] D. Jiles. *Introduction to Magnetism and Magnetic Materials*. Chapman and Hall, 2 edition, 1998.
- [2] D. Craik. *Magnetism, Principles and Applications*. Wiley, 1995.
- [3] A. Hubert and R. Schafer. *Magnetic Domains*. Springer, 1998.
- [4] R. Becker. Zur theorie der magnetisierungskurve (on the theory of the magnetisation curve). *Z. Phys*, 67:253–269, 1930.
- [5] F. Bitter. On inhomogeneties in the magnetization of ferrmagnetic materials. *Phys. Rev*, 38:1903–1905, 1931.
- [6] M. Prutton. *Thin Ferromagnetic Films*. Butterworth, 1964.
- [7] M.N. Baibich, J.M. Broto, A. Fert, F. Nguyen Van Dau, F. Petroff, P. Eitenne, G. Creuzet, A. Friederich, and J. Chazelas. Giant magnetoresistance of (001)fe/ (001)cr magnetic superlattices. *Phys. Rev. Lett*, 61(21):2472–2475, 1988.
- [8] S.S.P. Parkin, N. More, and K.P. Roche. Oscillations in exchange coupling and magnetoresistance in metallic superlattice structures. *Phys. Rev. Lett*, 64(19):2304–2308, 1990.
- [9] S.S.P. Parkin, R. Bhadra, and K.P. Roche. Oscillatory magnetic exchange coupling through thin copper layers. *Phys. Rev. Lett*, 66(16):2152–2155, 1991.

-
- [10] Eric E. Fullerton, M.J. Conover, J.E. Mattson, C.H.Sowers, and S.D. Bader. 150 % magnetoresistance in sputtered fe/cr(100) superlattices. *Appl. Phys. Lett.*, 63(12):1699–1701, 1993.
- [11] A. Fert and P. Bruno. *Ultrathin Magnetic Structures*. Springer-Verlang, Berlin, 1992.
- [12] A. Fert, P. Grunberg, A. Barthelemy, F. Petroff, and W. Zinn. Layered magnetic structures : interlayer exchange coupling and giant magnetoresistance. *J. Magn. Magn. Mat*, 140-144:1–8, 1995.
- [13] B.A. Jones. Theory of exchange coupling in magnetic multilayers. *IBM J. Res. Develop.*, 42(1):25–31, 1998.
- [14] M. D. Stiles. Interlayer exchange coupling. *J. Magn. Magn. Mat*, 200:322–337, 1999.
- [15] B. Dieny. Giant magnetoresistance in spin-valve multilayers. *J. Magn. Magn. Mat*, 136:335–339, 1994.
- [16] J.C.S. Kools. Exchange-biased spin-valves for magnetic storage. *IEEE Trans. Mag.*, 32(4):3165–3183, 1996.
- [17] J. Nogués and Ivan K. Schuller. Exchange bias. *J. Magn. Magn. Mat*, 192:203–232, 1999.
- [18] A.E. Berkowitz and K. Takano. Exchange anisotropy - a review. *J. Magn. Magn. Mat*, 200:552–570, 1999.
- [19] R.L. Stamps. Mechanisms for exchange bias. *J. Phys. D: Appl. Phys.*, 33:R247–R268, 2000.
- [20] D. Wei and H. Neal Bertram. Interlayer coupling and surface roughness in gmr spin valves. *IEEE Trans. Mag.*, 32(5):3434–3436, 1996.

-
- [21] J.C.S. Kools, Th.G.S.M. Rijks, A.E.M. De Beirman, and R. Coehoorn. On the ferromagnetic interlayer coupling in exchange-biased spin-valve multilayers. *IEEE Trans. Mag.*, 31(6):3918–3920, 1995.
- [22] J.H. Davies. *The Physics of Low-Dimensional Semiconductors*. Cambridge University Press, 1998.
- [23] S.M. Sze. *Semiconductor Devices*. Wiley, 1985.
- [24] Leica Ltd. *51 Coldhams Lane, Cambridge, CB1 3XJ*.
- [25] Barnard Microsystems Ltd. *134 Crouch Hill, London N8 9DX*.
- [26] Transcription Enterprises. *now Synopsis Inc. 700 East Middlefield Road, Mountain View, CA 94043*.
- [27] Dr S. Thoms. *Department of Electrical and Electronic Engineering, University of Glasgow, private communication*.
- [28] *SPIE Handbook of Microlithography, Micromachining and Microfabrication*. <http://www.cnf.cornell.edu/spiebook/TOC.htm>.
- [29] Dr C. Marrows. *Dept of Physics and Astronomy, E.C.Stoner Laboratory, University of Leeds, Leeds. LS2 9JT UK, private communication*.
- [30] D.E. Heim, R.E. Fonatana Jr., C. Tsang, V.S. Sperisou, B.A. Gurney, and M.L. Williams. Design and operation of spin valve sensors. *IEEE Trans. Magn.*, 30(2):316–321, 1994.
- [31] H.A.M. van den Berg, W. Clemens, G. Gieres, G. Rupp, M. Vieth, J. Wecker, and S. Zoll. Gmr angle detector with an artificial antiferromagnet subsystem (aaf). *J. Magn. Magn. Mate.*, 165:524–528, 1997.

- [32] H.A.M. van der Berg, J. Altmann, L. Br, Gieres G, R. Kinder, M. Veith, and J. Wecker. Magnetic tunnel sensors with co-cu artificial antiferromagnetic (aaf) hard subsystem. *IEEE Trans. Magn.*, 35(5):2892–2894, 1999.
- [33] K.J. Kirk. Nanomagnets for sensors and data storage. *Contemporary Physics*, 41(2):61–78, 2000.
- [34] B. Dieny, V.S. Speriosu, S.S.P. Parkin, B.A. Gurney, D.R. Wilhoit, and D. Mauri. Giant magnetoresistance in soft ferromagnetic multilayers. *Phys. Rev. B*, 43(1):1297–1300, 1991.
- [35] R.W. Cross, Y.K. Lim, J.O. Oti, and S.E. Russek. Magnetostatic effects in giant magnetoresistive spin-valve devices. *Appl. Phys. Lett*, 69(25):3935–3937, 1996.
- [36] K.R. Coffey et al. Spin valve magnetoresistive sensor with self-pinned laminated layer and magnetic recording system using the sensor. *US Patent*, page 5583725, 1996.
- [37] H.A.M. van den Berg, W. Clemens, G. Gieres, G. Rupp, W. Schelter, and M. Veith. Gmr sensor scheme with artificial antiferromagnetic subsystem. *IEEE Trans. Magn.*, 32(5):4624–4626, 1996.
- [38] J.L. Leal and M.H. Kryder. Spin valves exchange biased by co/ru/co synthetic antiferromagnets. *J. Appl. Phys.*, 83(7):3720–3723, 1998.
- [39] Y. Huai, J. Zhang, G.W. Anderson, P. Rana, S. Funada, C.Y. Hung, and M. Zhao. Spin valve heads with synthetic antiferromagnet cofe/ru/cofe/irnmn. *J. Appl. Phys.*, 85(8):5528–5530, 1999.
- [40] A. de Morais and A.K. Petford Long. Spin valve structures with artificial antiferromagnets. *J. Appl. Phys.*, 87(9):6977–6979, 2000.

-
- [41] C.H. Marrows, F.E. Stanley, and B.J. Hickey. Canted exchange bias in antiparallel biased spin valves. *J. Appl. Phys.*, 87(9):5058–5060, 2000.
- [42] H. Seok Cho, J. Chen, S. Cool, R. Michel, and N. Tabat. Effect of pinning field on the magnetization in patterned synthetic antiferromagnetic spin valves. *J. Appl. Phys.*, 87(9):4939–4941, 2000.
- [43] C.H. Marrows, G.L. Creeth, F.E. Stanley, B.J. Hickey, P.R. Aitchison, M. Crawford, and J.N. Chapman. Micromagnetic disorder in antiparallel biased spin valves. *Appl. Phys. Lett.*, 79(26):4384–4386, 2001.
- [44] J.N. Chapman. The investigation of magnetic domain structures in thin foild by electron microscopy. *J. Phys. D: Appl. Phys.*, 17:623–647, 1984.
- [45] J.N. Chapman and M.R. Scheinfein. Transmission electron microscopies of magnetic microstructures. *J. Magn. Magn. Mater.*, 200:729–740, 1999.
- [46] X. Portier and A.K. Petford-Long. Electron microscopy studies of spin-valve materials. *J. Phys. D: Appl. Phys.*, 32:R89–R108, 1999.
- [47] A.K. Petford-Long, X. Portier, E.Y. Tsymbal, T.C. Anthony, and J.A. Brug. In-situ lorentz microscopy of spin-valve structures. *IEEE Trans. Magn.*, 35(2):788–793, 1999.
- [48] S. McVitie, G.S. White, J. Scott, P. Warin, and J.N. Chapman. Quantitative imaging of magnetic domain walls in thin films using lorentz and magnetic force microscopies. *J. Appl. Phys.*, 90(10):5220–5227, 2001.
- [49] D.B. Williams and C.B. Carter. *Transmission electron microscopy*. Plenum Press, 1996.
- [50] J.N. Chapman, I.R. McFadyen, and S. McVitie. Modified differential phase contrast lorentz microscopy foe improved imaging of magnetic structures. *IEEE Trans. Mag.*, 26(5):1506–1511, 1990.

-
- [51] I.R. McFadyen and J.N. Chapman. Electron microscopy of magnetic materials. *EMSA Bulletin*, 22(2):64–75, 1992.
- [52] S. McVitie and J.N. Chapman. Reversal mechanism in lithographically defined magnetic thin film elements imaged by scanning transmission electron microscopy. *Microsc. Microanal.*, 3:146–153, 1997.
- [53] J.P. King. *An investigation of spin valves and related films by TEM*. PhD thesis, Solid State Group, University of Glasgow, 1999.
- [54] B. Dieny et al. Magnetoresistive sensor based on the spin valve effect. *US Patent*, page 5206590, 1993.
- [55] M.F. Gillies, J.N. Chapmans, and J.C.S. Kools. Magnetization reversal mechanisms in nife/cu/nife/femn spin valve structures. *J. Apply. Phys.*, 78(9):5554–5562, 1995.
- [56] J.P. King, J.N. Chapman, and J.C.S. Kools. Magnetisation reversal mechanisms of femn-biased spin-valves as a function of interlayer coupling strength and field orientation. *J. Magn. Magn. Mate*, 177-181:896–897, 1998.
- [57] J.P. King, J.N. Chapman, J.C.S. Kools, and M.F. Gillies. On the free layer reversal mechanism of femn-biased spin-valves with parallel anisotropy. *J. Phys. D: Appl. Phys.*, 32:1087–1096, 1999.
- [58] J.P. King, J.N. Chapman, M.F. Gillies, and J.C.S. Kools. Magnetisation reversal of nife films exchange biased by irmn and femn. *J. Phys. D: Appl. Phys.*, 34:528–538, 2001.
- [59] FEI. *Achtseweg Noord 5, PO Box 80066, 5600 KA Eindhoven*.
- [60] M. Schneider, H. Hoffmann, and J. Zweck. Magnetic switching of single vortex permalloy elements. *Appl. Phys. Lett.*, 79(19):3113–3115, 2001.

-
- [61] B. Khamsehpour, C.D.W. Wilkinson, J.N. Chapman, and A.B. Johnston. High resolution patterning of thin magnetic films to produce ultrasmall magnetic elements. *J. Vac. Sci. Technol. B*, 14(5):3351–3366, 1996.
- [62] R.H. Koch, J.G. Deak, D.W. Abraham, P.L. Trouiloud, R.A. Altman, Yu Lu, W.J. Gallacher, R.E. Scheuerlein, K.P. Roche, and S.S.P. Parkin. Magnetisation reversal in micron-sized magnetic thin films. *Phys. Rev. Lett.*, 81(20):4512–4515, 1998.
- [63] JQ. Wang, L.M. Malkinski, Y. Hao, C.A. Ross, J.A. Wiemann, and C.J. O’Connor. Fabrication of pseudo-spin-valves and 100 nm sized periodic elements for magnetic memory application. *Mat. Sci and Eng. B*, 76:1–5, 2000.
- [64] H. Arduin, J.N. Chapman, P.R. Aitchison, M.R. Gillies, K.J. Kirk, and C.D.W Wilkinson. Magnetisation reversal of patterned spin-tunnel junction material: A transmission electron microscopy study. *J. Appl. Phys.*, 88(5):2760–2765, 2000.
- [65] J.N. Chapman, P.R. Aitchison, K.J. Kirk, S. McVitie, J.C.S. Kools, and M.F. Gillies. Direct observation of magnetization reversal processes in micron-sized elements of spin-valve material. *J. Appl. Phys.*, 83(10):5321–5325, 1998.
- [66] K.J. Kirk, J.N. Chapman, and C.D.W. Wilkinson. Switching fields and magnetostatic interactions of thin film magnetic nanoelements. *Appl. Phys. Lett.*, 71(4):539–541, 1997.
- [67] G. Yi, P.R. Aitchison, W.D. Doyle, J.N. Chapman, and C.D.W. Wilkinson. Influence of end shape, temperature, and time on the switching of small magnetic elements. *J. Appl. Phys*, 92(10):6087–6093, 2002.

-
- [68] S. Chikazumi. *Physics of Magnetism*. John Wiley and Sons Inc., 1964.
- [69] X. Liu, J.N. Chapman, S. McVitie, and C.D.W. Wilkinson. Reversal mechanisms and metastable states in magnetic nanoelements. *accepted for publication in J. Appl. Phys.*
- [70] M.R. Scheinfiel and E.A. Price. Llg micromagnetics simulator. 4034 NW North Road, Portland, OR 97229.
- [71] M.R. Scheinfiel, J. Unguris, J.L. Blue, K.J. Coakley, D.T. Pierce, R.J. Celotta, and P.J. Ryan. Micromagnetics of 180 degree domain walls at surfaces. *Phys. Rev. B*, 43(3):3395–3422, 1991.
- [72] G.A. Prinz. Magnetolectronics applications. *J. Magn. Magn. Mate.*, 200:57–68, 1999.
- [73] M. Johnson, B.R. Bennett, M.J. Yang, M.M. Miller, and B.B. Shanabrook. Hybrid hall effect device. *Appl. Phys. Lett.*, 71(7):974–976, 1997.
- [74] A.K. Geim, S.V. Dubonos, J.G.S. Lok, I.V. Grigorieva, J.C. Maan, L. Theil Hansen, and P.E. Lindelof. Ballistic hall micromagnetometry. *Appl. Phys. Lett.*, 71(4):2379–2381, 1997.
- [75] V. Kubrak, F. Rahman, B.L. Gallagher, P.C. Main, M. Henini, C.H. Marrows, and M.A. Howson. Magnetoresistance of a two-dimensional electron gas due to a single magnetic barrier and its use for nanomagnetometry. *Appl. Phys. Lett.*, 74(17):2507–2509, 1999.
- [76] F.G. Monzon, M. Johnson, and M.L. Roukes. Strong hall voltage modulation in hybrid ferromagnet/semiconductor microstructures. *Appl. Phys. Lett.*, 71(21), 1999.

-
- [77] M. Johnson. Hybrid ferromagnet-semiconductor devices. *J. Vac. Sci. Technol.*, 16(3):1806–1811, 1998.
- [78] M. Johnson. Hybrid ferromagnet-semiconductor device for memory and logic. *IEEE Trans. Magn.*, 36(5):2758–2763, 2000.
- [79] A.K. Geim, I.V. Grigorieva, J.G.S. Lok, J.C. Maan, S.V. Dubonos X.Q. Li, F.M. Peeters, and Yu. V. Nazarov. Precision magnetometry on a submicron scale: magnetisation of superconducting quantum dots. *Appl. Phys. Lett.*, 23(1):151–160, 1998.
- [80] S.V. Dubonos, A.K. Geim, K.S. Novoselov, J.G.S. Lok, J.C. Maan, and M. Henini. Scattering of electrons at a magnetic protuberance of submicron size. *Physica E*, 6:746–750, 2000.
- [81] K.S. Novoselov, A.K. Geim, S.V. Dubonos, Y.G. Cornelissens, F.M. Peeters, and J.C. Maan. Scattering of ballistic electrons at a mesoscopic spot of strong magnetic field. *Phys. Rev. B*, 65:233312, 2002.
- [82] A. Nogaret, S.J. Bending, and M. Henini. Resistance resonance effects through magnetic edge states. *Phys. Rev. Lett.*, 84(10):2231–2234, 2000.
- [83] J. Reijnders and F.M. Peeters. Resistance effects due to magnetic guiding orbits. *Phys. Rev. B*, 763:165317, 2001.
- [84] V. Kubrak, A.W. Rushforth, A.C. Neumann, F. Rahman, B.L. Gallagher, P.C. Main, M. Henini, C.H. Marrows, and B.J. Hickey. The transport of 2d electrons through magnetic barriers. *Proceedings of MSS-9*, 1999.
- [85] V. Kubrak, A. Neumann, B.L. Gallagher, P.C. Main, M. Henini, C.H. Marrows, and B.J. Hickey. Magnetoresistance and hall magnetometry of single submicron ferromagnetic structures. *J. Appl. Phys.*, 87(9):5986–5988, 2000.

- [86] I.S. Ibrahim, V.A. Schweigert, and F.M. Peeters. Classical transport of electrons through magnetic barriers. *Phys. Rev. B*, 56(12):7508–7516, 1997.
- [87] J. Reijniers and F.M. Peeters. Hybrid ferromagnetic/semiconductor hall effect device. *Appl. Phys. Lett.*, 73(3):357–359, 1998.
- [88] J. Reijniers and F.M. Peeters. Diffusive transport and optimization of the hybrid hall effect device. *J. Appl. Phys.*, 87(11):8088–8092, 2000.
- [89] F.M. Peeters and X. Q. Li. Hall magnetometer in the ballistic regime. *Appl. Phys. Lett.*, 72(5), 1998.
- [90] I.S. Ibrahim, V.A. Schwigert, and F.M. Peeters. Diffusive transport in a hall junction with a microinhomogeneous magnetic field. *Phys. Rev. B*, 57(24):15 416–15 427, 1998.
- [91] J. Reijniers, F.M. Peeters, and A. Matulis. Electron scattering on circular symmetric magnetic profiles in a two-dimensional electron gas. *Phys. Rev. B.*, 64(245314), 2001.
- [92] J. Reijniers and F.M. Peeters. Resistance effects due to magnetic guiding orbits. *Phys. Rev. B.*, 63(165317), 2001.
- [93] S.M. Badalyan and F.M. Peeters. Transport of magnetic edge states in a quantum wire exposed to a non-homogeneous magnetic field. *Nanotechnology*, 12:570–576, 2001.
- [94] Oxford Instruments. *Tubney Woods, Abingdon, Oxon, OX14 5QX*.
- [95] T. McMullen. *to be published*. PhD thesis, University of Glasgow, 2004.
- [96] B. Milton. *Lateral Surface Superlattices in strained InGaAs layers*. PhD thesis, University of Glasgow, 2000.

-
- [97] H. Van Houten, C.W.J. Beenaker, P.M.H van Loosdrecht, T.J. Thornton, H. Ahmed, M. Pepper, C.T. Foxon, and J.J. Harris. Four-terminal magnetoresistance of a two-dimensional electron-gas constriction in the ballistic regime. *Phys. Rev. B*, 37(14):8534–8536, 1988.
- [98] T.J. Thornton, M.L. Roukes, A. Scherer, and B.P. Van der Gaag. Boundary scattering in quantum wires. *Phys. Rev. Lett.*, 63(19):2128–2131, 1989.
- [99] D.A. Wharam, T.J. Thornton, R. Newbury, M. Pepper, H. Ahmed, J.E.F. Frost, D.G. Hasko, D.C. Peacock, D.A. Ritchie, and G.A.C. Jones. One-dimensional transport and the quantisation of the ballistic resistance. *J. Phys. C: Solid State Phys.*, 21:L209–L214, 1988.
- [100] D.A. Wharam, M. Pepper, H. Ahmed, J.E.F. Frost, D.G. Hasko, D.C. Peacock, D.A. Ritchie, and G.A.C. Jones. Addition of the one-dimensional quantisation ballistic resistance. *J. Phys. C: Solid State Phys.*, 21:L887–L891, 1988.
- [101] C.W.J. Beenaker and H. van Houten. Quantum transport in semiconductor nanostructures. *Solid State Physics, Vol 44*, 1991.
- [102] I.A. Beardsley. Reconstruction of the magnetization in a thin film by a combination of lorentz microscopy and external field measurements. *IEEE Trans. Magn.*, 25(1):671–677, 1989.
- [103] S. McVitie, R.P. Ferrier, J. Scott, G.S. White, and A. Gallagher. Quantitative field measurements from magnetic force microscope tips comparison with point and extended charge models. *J. Appl. Phys.*, 89(7):3656–3661, 2001.
- [104] Gatan.

- [105] T. McMullen, E. Skuras, K.J. Kirk, J.H. Davies, and A.R. Long. The 2deg as a non-invasive tool for determining the switching behaviour in cobalt needle arrays. *Submitted to Physica E*.
- [106] J.N. Chapman, S. McVitie, and S.J. Hefferman. Mapping induction distributions by transmission electron microscopy. *J. Appl. Phys.*, 69(8):6078–6083, 1991.
- [107] S.J. Hefferman, J.N. Chapman, and S. McVitie. In-situ magnetising experiments on small regularly shaped permalloy particles. *J. Magn. Magn. Mate.*, 95:76–84, 1991.